University of Naples Federico II

Department of Physics

PhD Thesis in

Innovative Technologies for Materials, Sensors and Imaging

25st cycle

Sol-Gel Synthesis and Characterisation of pure and doped Transparent and Conductive ZnO Thin Films

Tutors: **Prof. Santolo Daliento**

Dr. Esther Fanelli

Coordinator: **Prof. Luciano Lanotte**

PhD Student: **Orlando Tari**

March 2013

CONTENTS

CHAPTER 2

CHAPTER 3

Acknowledgments

Ho fissato a lungo questa pagina prima di iniziare a scrivere. Ho rivisto mentalmente tutto il mio percorso formativo iniziando dalla scuola dell'infanzia e mi sono commosso. Mi rivedo bambino in fila per la mensa dell'asilo cantando "Ciao Teresina" e adesso sto per raggiungere il titolo di dottore di ricerca, il più alto nella formazione italiana. Mi riempio di un profondo sentimento di gratitudine che provo in modo sincero nei confronti di molte persone che mi hanno aiutato, sostenuto e consigliato durante la mia crescita formativa.

E' strano ricordarsi come a sei anni ti vedevi da grande, ma è bello costatare che ho fatto esattamente quello che avrei voluto: studiare e ricercare. Purtroppo non ho una mia fortezza delle scienze (☺) ma ho modo di lavorare nel mondo della ricerca scientifica. Se però ho raggiunto i miei obiettivi, il merito non è solo mio.

Rivendico con orgoglio le mie modeste origini. Sono figlio di contadini e sono fiero di poterlo dire. Ai miei genitori, Aristide e Nunzia, voglio rivolgere il primo posto in questo elenco di ringraziamenti. Li voglio, in qualche modo, ripagare dei tanti sacrifici fatti con amore. Grazie! Grazie per avermi dato tanto e per avermi sempre sostenuto in questo lungo percorso.

Voglio ringraziare i miei nonni, che ormai non ci sono più ma vivono nel mio cuore, per aver contribuito alla mia educazione e formazione.

Il percorso intrapreso mi ha cambiato profondamente rendendomi adulto e maturo. Con la fanciullezza dei sedici anni attendevo questo momento della mia vita, adesso "leopardianamente" desidero un po' di fanciullezza. Per questo ringrazio la mia fidanzata Sabrina che facendomi sentire "fanciullo" mi ha aiutato in modo indescrivibile in questi anni di studio. Voglio ringraziare anche i genitori della mia fidanzata, Cesare e Anna, perché anche da loro ho ricevuto sostegno e aiuto.

Tuttavia il mio percorso formativo non si sarebbe potuto concludere in questo modo senza l'aiuto che ho ricevuto dal prof. Santolo Daliento. Lui è stato il mio relatore durante la tesi di laurea specialistica e il mio tutor durante questi tre anni di dottorato. Ho lavorato con lui per circa quattro anni e posso dire che è stata un'esperienza che mi ha arricchito professionalmente e umanamente. Non è stato solo un insegnante, è stato un saggio consigliere che mi ha guidato in questo percorso. Grazie professore, per avermi dato quest'opportunità e per aver creduto in me, spero che il mio lavoro in qualche modo abbia ripagato le sue aspettative.

Il mio percorso formativo ha, però, avuto un altro forte punto di riferimento il prof. Aronne. Prima di iniziare il dottorato di ricerca non conoscevo il prof. Antonio Aronne, e le prime volte il suo nome "biblico" mi metteva agitazione. Conoscendolo ho capito che avevo a che fare con una persona competente, senza la quale gran parte di questo lavoro non si sarebbe svolto nella maniera in cui è stato presentato. Il professor Aronne mi ha guidato "per mano" nel complesso mondo della chimica. Grazie Professore.

Mentre scrivo, mi rendo conto che l'elenco delle persone a cui dire grazie è lungo e voglio cercare di ringraziare in modo adeguato tutti. Sicuramente una di queste è il professor Pasquale Pernice, che con la sua esperienza scientifica e pratica ha arricchito il mio lavoro. Un ringraziamento particolare lo rivolgo alla dott.ssa Esther Fanelli. Esther è stata per me un'insegnante e un'amica, mi ha aiutato molto nel laboratorio di chimica soprattutto all'inizio, dove quasi tutto mi era estraneo. È sempre stata presente in questi anni

stimolandomi ad andare avanti anche quando incontravo difficoltà apparentemente insormontabili. Mi mancheranno le passeggiate post-pranzo per il caffè.

Un ringraziamento sentito lo rivolgo al sempre ottimo Guido Celentano (segretario amministrativo del dottorato TIMSI), persona estremamente disponibile, competente, precisa e gentile. Grazie a lui, molte pratiche amministrative legate al dottorato sono state svolte con celerità e maestria.

In ogni esperienza ci sono dei compagni di viaggio, che forse anche a loro insaputa riescono a darti una mano, un aiuto. Voglio ringraziare pertanto, i miei colleghi Gianpaolo, Pierluigi, Gianlorenzo e Stefania, per essere stati miei compagni di viaggio in questo percorso.

In quest'attività ho avuto modo di collaborare con validi ricercatori del c.r. ENEA di Portici che mi hanno fatto sentire a casa ogni volta che andavo al centro. L'elenco delle persone da ringraziare è lunghissimo: Laura, Tiziana, Filiberto, Peppe, Emilia, Antonio, Angelica, Luigi, Annarita, Sonia, Tommaso, Iurie e spero di non aver dimenticato nessuno ☺.

Ma un ringraziamento particolare lo rivolgo alla dott.ssa Maria Luisa Addonizio, che per me è stato un riferimento fortissimo in questi anni. La considero a tutti gli effetti un mio tutor. Grazie dott.ssa per la sua disponibilità, grazie per aver messo a disposizione del mio progetto di ricerca la sua competenza scientifica, la sua serietà professionale e il suo tempo.

Voglio ringraziare anche le dott.sse Paola Delli Veneri e Lucia Mercaldo, perché si sono mostrate sempre disponibili a discussioni di approfondimento scientifico e hanno consentito la realizzazione di dispositivi fotovoltaici sui miei materiali.

Ci sono ancora molte altre persone da ringraziare e voglio farlo qui. Ognuno di voi mi ha dato qualcosa; di ognuno di voi conserverò un ricordo positivo qualunque sia la strada che intraprenderò. Grazie: Nicola, Davide, Alessio, Luca, Vito, Grazia, Maurizio, Flavio, Cinzia, Ivana e Dario.

Concludo con una citazione di Giovanni Paolo II, che mi emoziona ogni volta che la leggo:

"Prendete in mano la vostra vita e fatene un capolavoro"

SCIENTIFIC PUBLICATIONS

- **Publications in scientific journals**

1) S. Daliento, O. Tari and L. Lancellotti, *Closed-Form Analytical Expression for the Conductive and Dissipative Parameters of the MOS-C Equivalent Circuit,* **IEEE transaction on electronic devices**, Vol. 58 No. 10, (2011), pp. 3643-3646.

2) O.Tari, M. L. Addonizio, S. Daliento, E. Fanelli, P.Pernice, A. Aronne, *Sol-Gel synthesis of ZnO transparent and conductive films: a critical approach,* **Solar Energy Materials and Solar Cells**, Vol. 105, (2012), pp. 179-185.

3) L.Lancellotti, T. Polichetti, F. Ricciardella, O.Tari, S. Gnanapragasam, S. Daliento, G. Di Francia, *Graphene Applications in Schottky Barrier Solar Cells,* **Thin Solid Films**, Vol. 522, (2012), pp. 390-394.

4) O. Tari, S. Daliento, E. Fanelli, A. Aronne, P. Pernice, L.V. Mercaldo, P. Delli Veneri and I. Usatii, *Measurement of single junction shunt resistances in micromorph tandem solar cells*, under review to **EPJ Photovoltaics** (2012).

5) S. Daliento, V. D'Alessandro, O. Tari and L.V Mercaldo, *An approach to the measurement of shunt resistance and open-circuit voltage of individual subcells in tandem thin-film devices*, under review to **Progress in Photovoltaics: Research and Applications** (2012).

- **Publications in the proceedings of International Conferences and WorkShops**

1) S. Daliento, O. Tari, L. Lancellotti, S. Gnanapragasam, E. Bobeico, *Modelling and Characterisation of Passivating Layers for c-Si Concentrator Cells,*in the proceedings of 25th **EUPVSEC**, (2010) – Valencia (Spain), pp. 2268-2271. ISBN: 3-936338-26-4.

2) O. Tari, S. Daliento, E. Fanelli, L. Lancellotti, P. Delli Veneri, L. V. Mercaldo, I. Usatii *An Analysis On The Recombination Mechanisms In The Intrinsic Layer Of P-i-N a-Si:H Solar Cell*, in the proceedings of 26th **EUPVSEC**, (2011) – Hamburg (Germany), pp. 2589-2592, ISBN: 3-936338-27-2.

3) S. Daliento, O. Tari, L. Lancellotti, F. Roca, K.C. Heasman, L.M. Brown, *Design Strategies for Solar Cells Devised to the Low Wavelengths Portion of the Solar Spectrum*, in the proceedings of 26th **EUPVSEC**, (2011) – Hamburg (Germany), pp. 1459-1462 , ISBN: 3-936338-27-2.

4) L. Lancellotti, T. Polichetti, F Ricciardella, O. Tari, P. Guerriero, S. Gnanapragasam, I. Nasti, G. Di Francia, *Graphene Based Schottky Barrier Solar Cells*, in the proceedings of 26th **EUPVSEC**, (2011) – Hamburg (Germany), pp. 533-537, ISBN: 3-936338-27-2.

5) O. Tari, M. L. Addonizio, E. Fanelli, S. Daliento, P. Pernice, A. Aronne *Preparation and Characterisation of ZnO Sol-Gel Thin Films Deposited on Glass Substrates*, in the proceedings of 1th **SuNEC**, (2011) – Palermo (Italy), pp. OP-1, ISBN: 978-3-9502992-2-9.

6) T. Polichetti, L. Lancellotti, E. Massera, M. L. Miglietta, F. Ricciardella, S. Romano, O. Tari, S. Gnanapragasam, G.Di Francia, *Graphene: different fabrication technologies for Solid State devices*, in the proceedings of **Graphene** (2012) – Brussels (Belgium), pp. 253-254.

7) O. Tari, A. Aronne, P. Pernice, E. Fanelli, M.L. Addonizio and S. Daliento, *Sol-Gel Synthesis of Transparent and conductive oxides (TCOs) for thin film solar cells applications*, in the proceedings of **VIII Work-Shop Sol-Gel** (2012) – Trento (Italy), pp. 61-62, ISBN: 978-88-8443-4173.

8) O. Tari, S. Daliento, E. Fanelli, L. Lancellotti, *Measurement of Single Junction Shunt Resistance in Micromorph Tandem Solar Cells*, in the proceedings of **PVTC** (2012) – Aix-en-Provence (France), pp. 10-11.

9) A. Aronne, O. Tari, M. L. Addonizio, S. Daliento, E. Fanelli, P. Pernice, *Transparent and Conductive Thin Films by Sol-Gel*, in the proceedings of **AICIng** 2012 – Catania (Italy), pp.152-153. ISBN:978-88-7051-226-7.

- **Oral Presentation in International Conferences**

1) **TITLE**: "Preparation and Characterisation of ZnO Sol-Gel Thin Films Deposited on Glass Substrates" – **CONFERENCE**: SUNEC 2011 – **LOCATION**: Palermo (Italy) – Date: 5-7 July 2011.

2) **TITLE**: "Measurement of Single Junction Shunt Resistance in Micromorph Tandem Solar Cells" – **CONFERENCE**: PVTC 2012 – **LOCATION**: Aix-en-Provence (France) – Date: 6-8 June 2012.

3) **TITLE**: "Sol-Gel Synthesis of Transparent and conductive oxides (TCOs) for thin film solar cells applications" – **CONFERENCE**: VIII WorkShop Sol-Gel – **LOCATION**: Trento (Italy) – Date: 21-22 June 2012.

- **Poster Presentation in International Conferences and Schools**

1) **TITLE**: "Improved G-f analysis of RTO passivating films for concentrator silicon solar cells" – **CONFERENCE**: Spring Meeting E-MRS – **LOCATION**: Strasbourg (France) – Date: 7-11 June 2010.

2) **TITLE**: "Modelling and Characterisation of Passivating Layers for c-Si Concentrator Cells" – **CONFERENCE**: XXV EUPVSEC – **LOCATION**: Valencia (Spain) – Date: 6-10 September 2010.

3) **TITLE**: "Sol-Gel Preparation of Nanostructured Aluminium Doped ZnO (AZO) Thin Films for Photovoltaic Applications" – **School**: Training School "Synthesis of Hybrid Organic-Inorganic Nanoparticles for Innovative Nanostructered Composites" – **LOCATION**: Naples (Italy) – Date: 28 February – 2 March 2011.

4) **TITLE**: "Morphological, Optical and Electrical properties of ZnO Sol-Gel Transparent and Conductive films" – **CONFERENCE**: Spring Meeting E-MRS – **LOCATION**: Nice(France) – Date: 9-13 May 2011.

INTRODUCTION

Transparent Conductive Oxides (TCOs) such as Indium tin oxide (ITO), Al-doped zinc oxide (AZO) and Zinc-Doped Indium Oxide (IZO) are doped metal oxides. Their interest has grown for what it concerns the application of optoelectronic devices such as solar cells and liquid crystal displays due to their high conductivity and transmittance in the visible region of the spectrum. It is well known that optical, electrical, structural and morphological properties of the TCO films are important in order to determine the performances of the device.

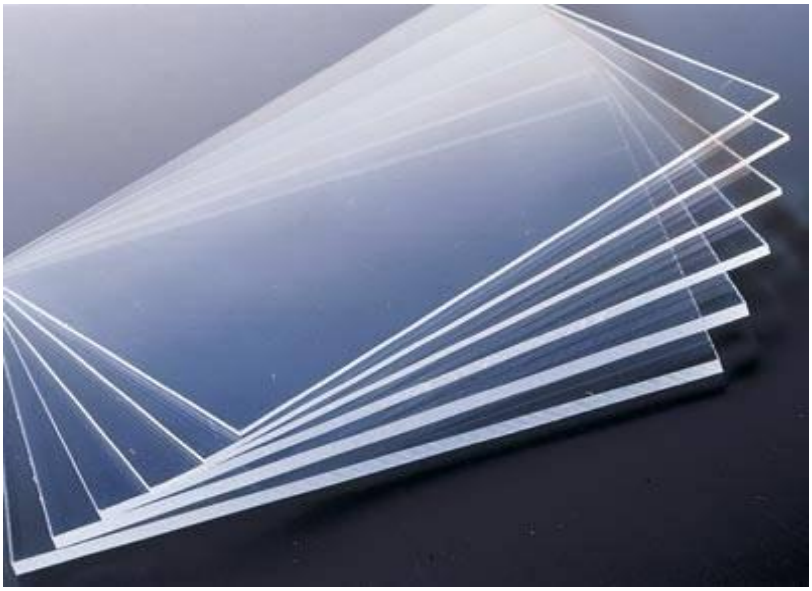

Figure 1: TCO on Glass substrates.

In the case of thin film solar cells [1] TCO layers play a unique role. The performances of solar devices are affected for the 40% by TCO electrical and optical properties; moreover the deposition costs of TCO layers represent about the 30-35% of the total device cost [1].

In particular, in photovoltaic (PV) applications the incident light has to pass through the TCO layer without any optical losses. Furthermore, photogenerated carriers into the active layers of the solar cell (e.g. hydrogenated amorphous silicon: a-Si:H) have to be collected from the TCO layer. Finally, due to the low dimensions of the Thin Film Solar Cells (TSFC) the TCO layer has to scatter the incident light [2] in order to increase the optical pathway of the light into the active layers and to enable the so-called “light trapping” [2].

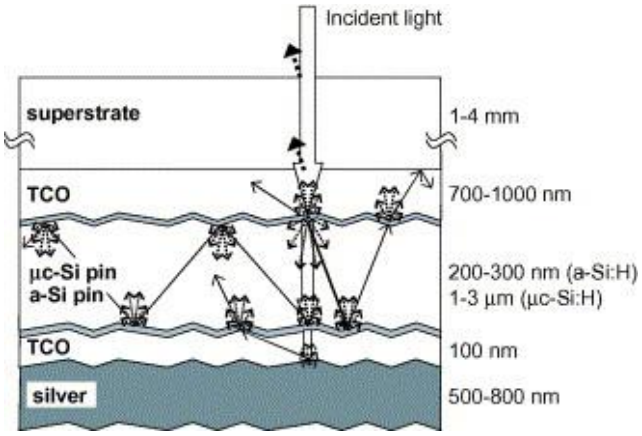

Figure 2: Schematic (not in scale) of a single junction thin film solar cell.

A complete list of all TCO requirements for PV applications is available in [3]:

- High total transmittance in the visible (VIS) region of solar spectrum (> 80-85%);
- High diffuse transmittance in the VIS region (> 30 -35%);
- High surface roughness (root main square (*RMS*) > 35 *nm*) in order to scatter the incident light and to make possible the light-trapping;
- High adhesion force to glass substrate (> 100 kg/cm^2);
- Good film uniformity and low porosity;
- High crystal grain size (> 20 *nm*);
- Low electrical resistivity (< 10^{-3} $\Omega \cdot cm$)

The most common used TCO materials are:

- Tin-doped Indium Oxide (ITO);
- Fluorine-doped Tin Oxide (SnO_2:F);
- Aluminium or Boron doped zinc oxide (AZO or BZO).

ITO was the first TCO to be introduced by Rupperecht in 1954 [4]. Thanks to its high transmittance and low resistivity ITO was often chosen as front electrode in solar cells and flat panel displays. However, it is important to underline that indium is rare and quite expensive. Great care must be taken when exposing SnO_2 to

hydrogen plasma atmosphere (required for solar cell deposition) in order to avoid degradation of optical and electrical characteristics. Therefore, ITO was often replaced by Doped Zinc Oxide (ZnO) due to its lower cost, its wider availability, its non-toxicity and its higher stability.

Typical doping elements used to prepare doped ZnO thin films include Aluminium (Al), Boron (B), Gallium (Ga), Indium (In) and Tin (Sn).

In general, ZnO thin films are deposited on glass substrates through vacuum deposition techniques such as sputtering [5] and Chemical vapour deposition (CVD) [6] methods. Both processes are energy-intensive because of the high vacuum level of these deposition systems, their high maintenance costs and their high dissipated energy amount during layers deposition.

In this research activity solution-gelation (Sol-Gel) route was chosen as a low cost alternative technique. In particular dip-coating method has been selected to deposit ZnO films on glass supports.

The Sol–Gel method is a low temperature wet chemical process characterised by a very high versatility. It allows controlling chemical composition, shape, structure, textural as well as morphological properties of final materials by adjusting processing parameters. Sol–Gel allows coating large areas of arbitrary shaped substrates. Its equipment is cheaper than the one of CVD. Finally, the energy dissipated during the deposition process is lower than the one of CVD or sputtering.

The main goal of this PhD research activity is the study Sol-Gel synthesis of doped transparent and conductive ZnO thin films on glass substrates. In particular, the most important synthesis parameters (such as Zn molar concentration, annealing temperature and time, post annealing environment and solution pH value) were examined in-depth. The gel derived ZnO layers were characterised from a structural, morphological, optical and electrical point of view. A new characterisation technique based on impedance spectroscopy of a Metal-Oxide-Semiconductor (MOS) structures was developed in order to qualify the electrical interface between the fabricated ZnO layers and the others layers in the final device (e.g. active layer, hydrogenated amorphous silicon (a-Si:H) in thin film solar cells). Finally, amorphous silicon thin film solar cells (single-junction) were deposited on gel derived doped ZnO and characterised.

This PhD thesis is divided into four chapters. In the first chapter, an overview on thin film solar cell technology, concerning the TCO role is presented. Moreover, the TCO electrical and optical properties are deeply discussed.

In the second chapter, the Sol-Gel technology is introduced. The ZnO synthesis is investigated and the adopted procedure is discussed. Finally, the key synthesis parameters monitored throughout this research are explained.

The third chapter deals with the so-called characterisation techniques. Both standard and innovative techniques are presented. A list of ZnO films for each analysed method is made. The last part of this chapter presents the most recently developed innovative characterisation technique.

In the fourth section of this PhD thesis, a hard look is taken to the experimental results carried out on gel derived pure and doped ZnO films. Finally, the electrical characterisation of thin film solar cells deposited on the best ZnO films is presented.

[1] A. Luque and S. Hegedus, Handbook of Photovoltaic Science and Engineering, Wiley: West Sussex, England (2003).

[2] J. I. Cisneros, Applied Optics, 37, pp. 5262-5270 (1998).

[3] M. W. Rowell and M. D. McGehee, *Energy Environ. Sci.*, 4, pp. 131-134 (2011).

[4] G. Rupperecht, Z. Phys., 139, pp. 504-511 (1954).

[5] K. Ellmer, A. Klein and B. Rech, Transparent conductive zinc oxide; Springer series in materials science, vol. 104, Springer-Verlag, Berlin, (2008).

[6] C. Jagadish and S.J. Pearton, Zinc Oxide: Bulk, Thin Films and Nanostructures, Elsevier, Oxford, U.K., (2006).

CHAPTER 1

Thin Film Technology

As discussed in the preface, the goal of this PhD activity is the fabrication and the characterisation of Transparent and Conductive Oxides (TCO) layers for thin film solar cells (TFSC). In particular, the Sol-Gel method has been chosen as a cost-effective alternative to the vacuum deposition system for TCO. This layer is one of the most important, because its deposition cost is about the 35% of TFSC [1] and because it strongly affects the performances of such cells.

In recent years, the photovoltaics (PV) market has been booming, with sales almost completely dominated by product based on the use of silicon wafers, similar to those used in microelectronics. Wafer costs account for over 50% of the total module cost. A way to eliminate this cost is to replace wafers by thin-films of semiconductors deposited on the substrate. The sustained boom has been causing demands for silicon wafers to outstrip the capacity to supply, creating a market entry opportunity for a number of competing thin-film technologies. These fall into two main classes: one based on silicon in amorphous, nanocrystalline and polycrystalline phases and on polycrystalline chalcogenide (group six) semiconducting compounds. A third class of emerging technologies is based on organometallic dyes and polymers. In this chapter, the main thin film technologies will be presented, focusing on the TCO role. Furthermore, the TCO electrical and optical properties will be discussed.

1. Thin Film Technology Development

In the 1980's, research activities on thin film PV technology was minimal. After this period, there has been a constant progress, in terms of research on manufacturing technology and used materials. The trade-off between cost-effective electricity generating technology has led corporations and investors towards the thin film PV industry which finally saw more than 100 companies entering in the market between 2001 and 2011.

Therefore, a development in the thin film PV technology has been registered: from a mere 14 *MW* production in 2001 the market has grown to 3600 *MW* in 2011 (*Source: Thin Film 2012–2016: Technologies, Markets and Strategies for Survival -GTM Research)*. The market outlook for the coming decade appears promising, as shown in Figure 1.1. In retrospect, the thin film module production is expected to grow at the rate of 30% from 2012 to reach 10 *GW* production by 2016. The forecast for the total PV production by 2016 is about 56 *GW* (*IMS Research's latest forecast for global PV installations*). Hence, the thin film technology is expected to take approximately 18% of total PV demand in 2016.

Current thin film modules are based on amorphous silicon (a-Si), either in a single or multiple junction configurations, as well as on the chalcogenide compounds CdTe, CIS (copper indium diselenide or disulphide) or GIGS (copper indium gallium selenide). Over the past 5 *years*, rapidly-growing production volumes are dominated by the amorphous silicon, cadmium telluride and CIGS approaches. However, since the volumes associated with the wafer-based approaches have also been increasing rapidly, the thin film technologies have to grow quickly just to maintain their present market share (the total combined share nowadays is less than 10%). There are high barriers for thin film technologies to enter the market due to higher capital costs per unit output for thin film manufacturing facilities. The manufacturing of the conventional wafer-based modules is commonly broken down into four separately-financed operations: silicon purification, crystal growth and wafering, cell processing and cell encapsulation. However, in a thin film technology all these operations are effectively bundled into the one facility.

The rapidly escalating demand for silicon wafers has been creating a supply shortage that will moderate the growth of the wafer-based output over at least the next 2 *years*. This gives to the thin film product an opportunity to increase its market share and to establish its credentials on a market previously disinterested.

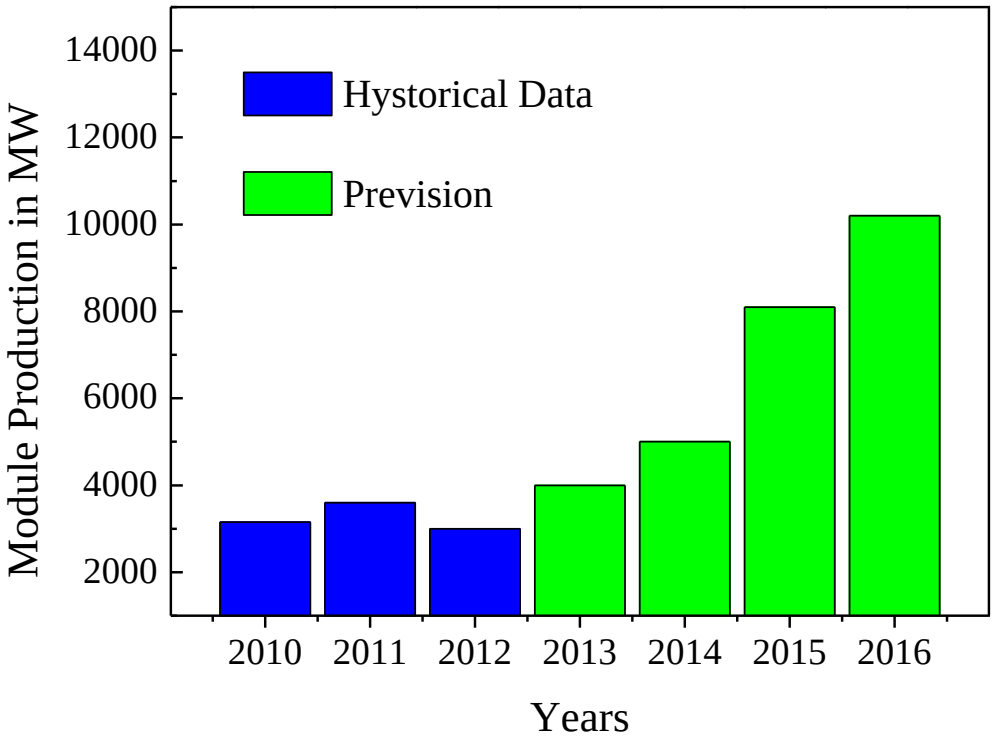

Figure 1.1: Global Thin Film Production in MW (Source: *Thin Film 2012–2016: Technologies, Markets and Strategies for Survival* - *GTM Research*).

1.1. Silicon Based

In this paragraph the most common silicon based thin film solar cells are introduced in order to present both their advantages and disadvantages.

1.1.1. Single Junction Amorphous Silicon

Since the early 1980s amorphous silicon (a-Si) solar cells have been used in consumer products such as calculators and digital watches. Later, some attempts were made to launch outdoor power modules on the market. However, only over the last years several companies, notably Kaneka and Mitsubishi in Japan, have

supplied single junction a-Si power modules in appreciable quantities. The amorphous silicon is deposited at low temperature in a way that allows about 10% (in atoms) hydrogen to be incorporated: the secret of this technology's success [2, 3]. In fact it has been proved that the hydrogen greatly improves the quality of the material.

A *p-i-n* junction structure, see Figure 1.2, is used with the n and p-type regions creating a field in the intrinsic-layer due to their work-function difference [3]. Since the amorphous silicon is not very conductive, a key feature of the technology is the use of a transparent conductive oxide (TCO) layer between the silicon and the glass.

The front TCO is one of the most important layer in the cell structure. In fact it has to collect the photogenerated carriers in the active layers (it must have a low sheet resistance of about 10 $\Omega/\square$) and it should not absorb the incident light. This means that it must have a very high optical transmittance (> 90%) in the visible region of the solar spectrum. Moreover, the TCO surface morphology has to be able to scatter the incident light in order to increase the optical pathway of photons inside the active layers of the cell and to generate more carriers. A comprehensive overview on the TCO requirements for thin film solar cell may be found in [4].

The strength of a-Si technology is its simplicity combined with the use of benign and abundant form of silicon. The technology is also able to capitalise on equipment development in the active matrix display area, where similar deposition equipment is used. The relatively slow spreading of a-Si technology, given its early potential, is due to the light-induced degradation of its material quality. Manufacturers now report cells parameters in terms of ''stabilized'' performance which are obtained after a month or two of light exposure. However, stabilized module efficiency is quite low, generally in the 7–11% range [5].

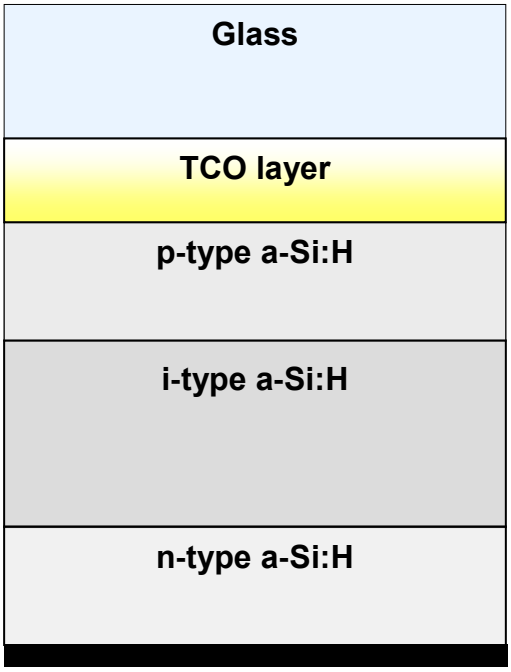

Figure 1.2: Single-junction amorphous silicon solar cell (qualitative structure).

1.1.2. Multiple Junction Silicon Cells

A way to reduce the decreased material quality under light exposure is to use thinner layers of amorphous silicon. This is possible if two or more cells are stacked in series. If the bandgaps of the lower cells are smaller than that of the upper cells, this also produces a performance boost [6].

The earliest approach to reduce the bandgap from the quite high values typical of hydrogenated amorphous silicon (1.75 *eV*) was by alloying it with germanium. At present, this approach is successfully proposed by a US Company, United Solar. It produces a module based on a 3-cell stack with the two underlying cells made from a-Si alloyed with germanium. This gives nominal module performance within the 7–9% range, comparable to the best of the single junction a-Si technologies. A more recent approach is to combine an amorphous silicon top cell with a bottom cell consisting of microcrystalline silicon, as shown in Figure 1.3. The bandgap of the lower cell is determined by the crystalline regions in this mixed phase and it is similar to the one of wafer-based cells (1.1 *eV*). The use of two junctions improves the module performance to the 9–12% range

[5]. The strengths and weaknesses of this technology are the same of a-Si:H technology. Quantities of such modules have recently been supplied on the market by two Japanese manufacturers, Kaneka and Sharp.

It has to be noticed that also for this kind of device TCO layer plays a key role. The reasons are the same as in the case of a-Si:H solar cells. Standard materials used as TCO layer in this kind of devices are Indium tin oxide (ITO), doped ZnO and SnO_2:F.

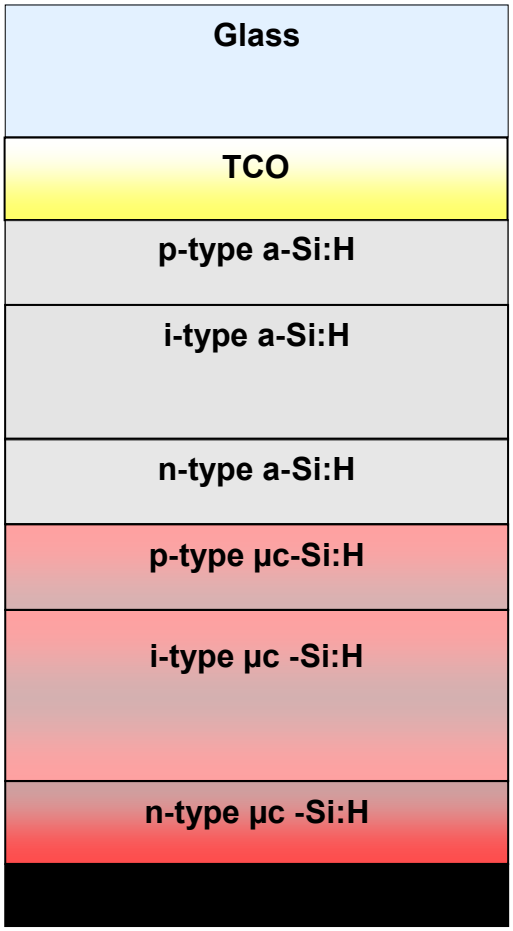

Figure 1.3: Structure of tandem Solar Cell.

1.2. Chalcogenide-Based Cells

1.2.1. Cadmium Sulphide

The first thin film solar cell candidates for large-scale manufacture were based on cadmium sulphide. Attempts to commercialise this technology in the mid-1970s and early 1980s were unsuccessful, due to stability issues with cells and with the introduction of amorphous silicon as an apparently superior contender at that time. However, greater difficulties than originally anticipated in commercializing amorphous silicon provided opportunities for two related chalcogenide-based polycrystalline thin film technologies discussed below.

1.2.2 Cadmium Telluride

A schematic of a cadmium telluride cell is drawn in Figure 1.4. CdTe PV cells are created in the superstrate configuration and the charge carrier separation occurs via a heterojunction. The process starts with the deposition of a TCO layer onto the planar soda lime glass substrate (ITO and doped ZnO are typically used). Subsequently, the depositions of the cadmium sulphide (CdS) window layer (thickness ~ 100 *nm*) and the CdTe absorber layer (thickness ~ 5 μm) follow. These two polycrystalline semiconductor materials are chemically very stable and they can relatively easy deposit stoichiometrically at 400–600°*C*. Efficiencies of up to 18*%* have been reported with small-area cells, while the best commercial modules are presently 11-13*%* efficient [5]. Over the last years the commercialisation of PV technologies increased and one of the companies that mostly benefitted of it was the US First Solar, Inc..

The main technical issue of the CdTe technology is related to the back contact. Specifically, the relatively light p-type doping of the CdTe layer complicates the realisation of a low-resistance, long-term-stable back contact. One possible solution is the formation of a thin heavily doped p^+ layer at the back surface of the

CdTe layer. Another approach is the deposition of a thin p^+ doped buffer layer having a smaller bandgap than CdTe (i.e., forming a heterostructure). The main issue of the CdTe PV technology, however, is related to the toxicity of Cd. Even if a proper modules recycling is offered by manufacturers, it is questionable whether the production and the deployment of Cd-based modules are sufficiently environmentally-friendly to justify their use instead of less problematic PV technologies. Furthermore, Te is a scarce element and hence, even if most of the annual global Te production is used for PV, CdTe PV module production seems limited to levels of a few GW_p per year.

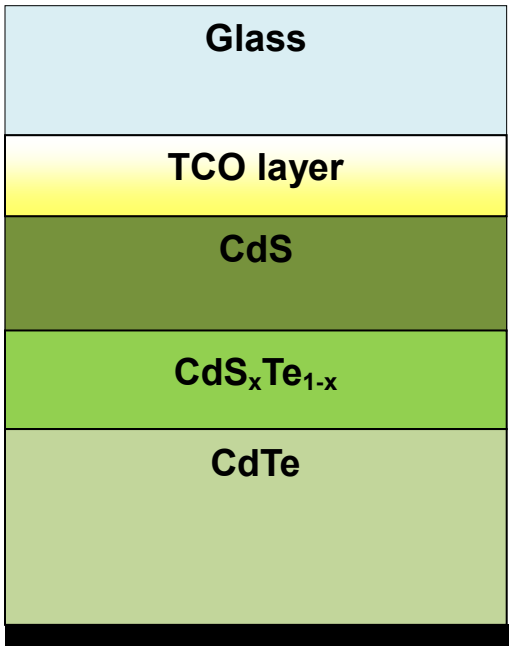

Figure 1.4: Schematic of a Cadmium Telluride cell.

1.2.3 Copper-Indium Diselenide (CIS)

CIS modules are fabricated in the *substrate* configuration, i.e. from back to front. In this case there is no need for a transparent supporting material (TCO), giving flexibility with respect to the choice of the substrate. While flexible substrates are being investigated, the standard substrate is soda-lime glass due to its availability, cost effectiveness, and the enhancement of the doping concentration in the CIS absorber layer by sodium atoms that diffuse from the substrate into the CIS layer during the module fabrication process. The process starts with a glass substrate clean, followed by the deposition of a thin molybdenum (Mo) film and scribing of the Mo film. Then the deposition of the polycrystalline CIS absorber film follows. It deals with a complex system involving the five elements Cu, In, Ga, Se and S. The bandgap is 1.0 *eV* for copper indium diselenide and it increases when gallium is added to replace indium, CIGS technology [1]. Once more, as in the case of CdTe, the absorber layer is automatically p-type doped. The CIS materials system is more complex than CdTe and it has higher demands on the process control systems. As in CdTe solar cells, the separation of the photo-generated carriers occurs via a heterojunction formed by n-type CdS. A thin intrinsic ZnO layer is then sputtered onto the CdS, followed by sputter deposition of a thick (~ 1 μm) front TCO (Al-doped ZnO).

The CIS technology is a star performer in the laboratory, with confirmed efficiencies of up to 20% for small area cells [7]. However, the technology has encountered difficulties in its commercialisation. The best commercial modules at the moment are 13–15% efficient [5].

The main technical issue of the CIS technology is associated with the complexity of the CIS absorber layer (a 5-element system) which imposes significant challenges for the realization of uniform film properties across large-area substrates using high-throughput equipment. Further issues are the use of cadmium (as previously noticed) and the use of indium, an element poorly retrieved.

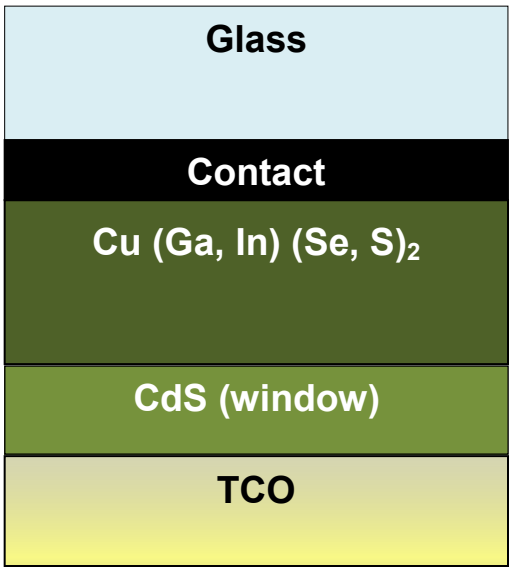

Figure 1.5: Schematic of a CIS solar cell.

2. Transparent and Conductive oxides

In this paragraph an overview on the TCO electrical and optical properties is reported.

2.1. TCO Overview

Most optically transparent and conductive oxides (TCOs) are binary or ternary compounds, containing one or two metallic elements. Their resistivity could be lower than $10^{-4}\ \Omega \cdot cm$, and their extinction coefficient (k) in the optical visible range (Vis) is lower than 0.0001, owing a wide optical bandgap (E_g) greater than 3 eV. This remarkable combination of conductivity and transparency is usually impossible in intrinsic stoichiometric oxides. However, it is stored by producing them with a non-stoichiometric composition or by introducing appropriate dopants. Badeker discovered that thin CdO films possess such characteristics [8]. Later, it was recognized that thin films of ZnO, SnO_2, In_2O_3 and their alloys were also TCOs. Doping these oxides resulted in improving electrical conductivity without degrading their optical transmission. Al/B doped ZnO (AZO/BZO), tin doped In_2O_3, (ITO) and antimony or fluorine doped SnO_2 (ATO and FTO) are among the most used TCO thin films in modern technology. In particular, ITO is extensively used.

The actual and potential applications of TCO thin films include:

- transparent electrodes for flat panel displays;
- transparent electrodes for photovoltaic cells;
- low emissivity windows;
- transparent thin films transistors;
- light emitting diodes;
- semiconductor lasers.

As the usefulness of TCO thin films depends on both their optical and electrical properties, both parameters should be considered together with environmental stability, abrasion resistance, electron work function and compatibility with substrate and other components of a given device, as appropriate for the application. The availability of raw materials and the costs of the deposition method are also key factors in choosing the most appropriate TCO material. The selection decision is generally made by maximising the functioning of the TCO thin film by considering all relevant parameters and minimizing the expenses. TCO material selection is based only on maximising the conductivity and on its transparency.

Recently, the research activity has being addressed to find a substitute for ITO, the most popular TCO, due to the shortage and to the high price of Indium needed for ITO. A 100 *nm* thick ITO film have optical transmission (T) of about 90% and a sheet resistance (R_s) of about 10 $\Omega/\square$. Up to now, AZO and ZnO:Ga (GZO) semiconductors are considered to be the possible alternative to ITO for thin film transparent electrode applications. The best candidate is AZO which can have a low resistivity (about $10^{-4}\ \Omega \cdot cm$) and its source materials are inexpensive and non-toxic. However, the development of large area and high rate deposition techniques are needed.

Published reviews on TCOs deposition and diagnostic techniques on film characteristics and expected applications are shown [9-15]. This chapter has three objectives: (1) to review the theoretical and experimental efforts in order to explore brand-new TCO materials intended to improve the TCO performance, (2) to explain the intrinsic physical limitations that affect the development of an alternative TCO with properties equivalent to those of ITO, and (3) to review the practical and industrial applications of existing TCO thin films.

2.2. *TCO Electrical Conduction*

TCOs are wide band gap (E_g) semiconducting oxides, with electrical resistivity ρ in the range 10^{-4} – $10^{11} \Omega \cdot cm$. The conductivity is due to doping either by oxygen vacancies or by extrinsic dopants. In the absence of doping, these oxides become proper insulators with an electrical resistivity (ρ) > $10^{8}\ \Omega \cdot cm$. Most of the TCOs are n-type semiconductors. The electrical conductivity of n-type TCO thin films depends on the electron density in the conduction band and on their mobility. It is equal to: $\sigma = \mu n q$, where μ is the electron mobility, n is the electrons density, and q is the electron charge. The mobility is given by:

$$\mu = \frac{q\tau}{m*} \qquad (1.1)$$

where τ is the mean time between collisions, and m^* is the effective electron mass. However, as n and τ are negatively correlated, the magnitude of μ is limited. Due to the large energy gap (E_g > 3 eV) separating the valence band from the conducting band, the conduction band cannot be thermally populated at room temperature. Hence, stoichiometric crystalline TCOs are good insulators [14]. To explain the TCO characteristics, various population mechanisms and several models describing the electron mobility were proposed. Some characteristics of the mobility and the processes by which the conduction band is populated with electrons were shown to be interconnected by electronic structure studies [16], e.g., that the mobility is proportional to the magnitude of the band gap.

In the case of intrinsic materials, the density of conducting electrons was often attributed to the presence of unintentionally introduced donor centres, usually identified as metallic interstitials or oxygen vacancies that produced shallow donor or impurity states located close to the conduction band. The excess or donor electrons are thermally ionized at room temperature and they move into the host conduction band. However, experiments have been inconclusive as to which of the possible dopants was the predominant donor. Extrinsic dopants have an important role in populating the conduction band and some of them were unintentionally introduced. Thus, it was conjectured in the case of ZnO that interstitial hydrogen, in the H^+ donor state could be responsible for the presence of carrier electrons [17]. In the case of SnO_2, the important role of interstitial Sn in populating the

conducting band, in addition to that of oxygen vacancies, was conclusively supported by first-principle calculations of Kiliç and Zunger [18]. They both showed that Sn interstitials and O vacancies dominating the defect structure of SnO_2 due to the multivalence of Sn explained the natural nonstoichiometry of this material and they produced shallow donor levels, turning the material into an intrinsic n-type semiconductor [17]. Electrons released by these defects were not compensated because acceptor-like intrinsic defects consisting of Sn voids and O interstitials did not form spontaneously. Furthermore, the released electrons did not make direct optical transitions in the visible range due to the large gap between the Fermi level and the energy level of the first unoccupied states. Thus, SnO_2 could have a carrier density with minor effects on its transparency [17].

The conductivity σ is intrinsically limited for two reasons. First, n and μ cannot be independently increased for practical TCOs with relatively high carrier concentrations. At high conducting electron density, carrier transport is limited primarily by ionized impurity scattering, i.e., the Coulomb interactions between electrons and the dopants. A higher doping concentration reduces carrier mobility to a degree that the conductivity does not increase. Furthermore, it decreases the optical transmission at the near-infrared edge. By increasing the dopant concentration, the resistivity reaches a lower limit and it does not decrease beyond it, whereas the optical window becomes narrower. Bellingham *et al.* [19] firstly reported that the mobility and hence the resistivity of transparent conductive oxides (ITO, SnO_2, ZnO) are limited by ionized impurity scattering for carrier concentrations above 10^{20} cm^{-3}. Ellmer [20-21] also showed that in ZnO films deposited by various methods, the resistivity and the mobility were nearly independent of the deposition method and limited to about 2×10^{-4} $\Omega \cdot cm$ and 50 cm^2/Vs, respectively. In ITO films, the maximum carrier concentration was about 1.5×10^{21} cm^{-3}, and the same conductivity and mobility limits were held [22]. This phenomenon is also a universal characteristic of other semiconductors [14]. Scattering by the ionized dopant atoms that are homogeneously distributed in the semiconductor, there is only one possible effect that reduces the mobility. All the recently developed TCO materials, including doped and undoped binary, ternary and quaternary compounds, also suffer from same limitations. Only some exceptional samples had a resistivity of $\leq 1\times10^{-4}$ $\Omega \cdot cm$.

In addition to the above mentioned effects that limit the conductivity, high dopant concentration could lead to clustering of the dopant ions [23], which increase significantly the scattering rate and it could also

produce non-parabolicity of the conduction band. This has to be taken into account for degenerately doped semiconductors with filled conduction bands [24].

2.3. TCO Optical Properties

As mentioned above, besides low resistivity, effective TCO thin films should have a very low absorption coefficient in the near UV-VIS-NIR region. The transmission in the near UV is limited by E_g, as photons with energy larger than E_g are absorbed. A second transmission edge exists at the NIR region, mainly due to reflection at the plasma frequency. Ideally, a wide band gap TCO should not absorb photons in the "window" transmission in the UV-Vis-NIR region. However, there are no "ideal" TCOs thin films and even if such films could be deposited, reflections and interferences would also affect the transmission itself. Hence, 100% transparency over a wide region cannot be obtained.

The optical properties of TCOs transmission *T*, reflection *R*, and absorption *A*, are determined by its refraction index *n*, extinction coefficient *k*, band gap E_g and geometry. Geometry includes film thickness, thickness uniformity and film surface roughness. *T*, *R* and, *A* are intrinsic, depending on the chemical composition and solid structure of the material, whereas the geometry is extrinsic. There is a negative correlation between the carrier density and the position of the IR absorption edge. Instead, positive correlation between the carrier density and the UV absorption edge are noticed as E_g increases at larger carrier density (Moss-Burstein effect). As a result, it can be said that the TCO transmission boundaries and conductivity are interconnected.

The width of the Vis transmission window of a TCO film with thickness deposited on a transparent substrate is affected not only by the optical parameters of the TCO film but also by the optical properties of the substrate. The refractive index n_{sub} of the most common substrates are ~ 1.45 for fused silica and ~ 1.6 for various glasses. The extinction coefficient of the substrate (k_{sub}) is generally < 10^{-7}, hence any light absorption would take place in the film, where generally $k_{film} > k_{sub}$. For films thicker than 100 *nm* several interference bands could be formed producing maximal and minimal values of *T* when either the wavelength or thickness is varied.

When $k_{film} \approx 0$, the peak transmission (T_{max}) is equal to the transmission of the substrate [25]. Hence, assuming that the sample is in air, T_{max} = 90% and 93% for films deposited on glass and fused silica, respectively. The minimum sample transmission (T_{min}) in air is expressed by:

$$T_{\min} = \frac{4n^2 n_{sub}}{(1+n^2)\cdot(n^2+n_{sub}^2)} \qquad (1.2)$$

As most TCO films have values of n in the visible range 1.8 – 2.8, $T_{\min}$ will be in the range 0.8 – 0.52. $T_{\min}$ is closely approximated by the relation: $T_{min} = 0.051n^2 - 0.545n + 1.654$. As n in the VIS decreases with wavelength, $T_{\min}$ increases with wavelength, but will not exceed ~ 0.8. When the film extinction coefficient is not negligible and it affects the transmission, $T_{\max} < T_{\text{sub}}$, and $T_{\min}$ also decreases. By decreasing the TCO film thickness, T is increased but the sheet resistance decreases. Combining together the optical and electrical properties of the film, the fraction of the flux absorbed in a film (A) is given by the expression:

$$A \approx 1 - e^{-\frac{\alpha}{\sigma R}} \qquad (1.3)$$

Figure1.6 presents plots of the fraction of the absorbed power at wavelength of 400 *nm* and $k \sim 0.02$ as a function of the conductivity for three representative values of R_s. For a given σ, low values of R_s necessitate using thick films and lower conductivity requires the use of even thicker films resulting in an increase in the loss of radiative power. The dependence of film thickness on the conductivity for three values of R_s is presented in Figure 1.7.

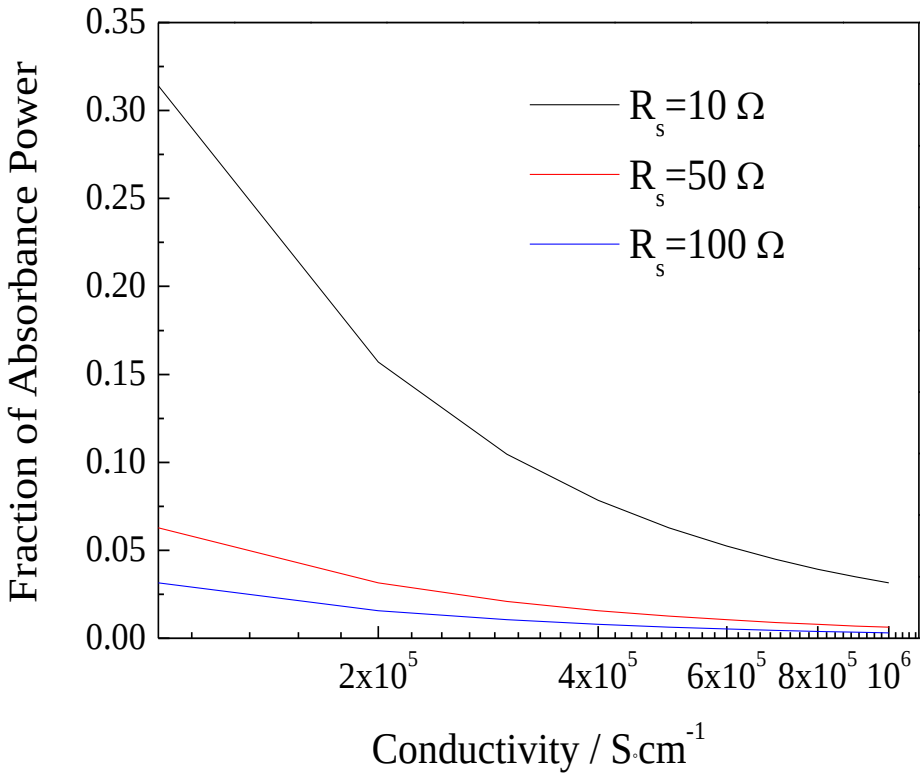

Figure 1.6: Fraction of absorbed power as function of TCO conductivity.

Using the same film conductivity, applications requiring the lowest R_S will be thicker and the absorbed fraction will be higher. At present, only a high quality ITO is compatible with the condition that the absorbed power fraction be lower than 10% and R_S =10 Ω/□. At lower extinction coefficient (k) films with lower conductivities can be used, e.g., when k =0.002 instead of 0.02. The absorbed power A is lower by a factor of ~ 8 and it allows the use of thicker films. The combination of film thickness, conductivity and extinction coefficient determines the absorption of the radiation flux. However, when the total transmission T is considered, reflection and interference must also be considered. This factor depends on the refractive indices of the substrate and the film as well as on the film thickness. A general formula for T and R was provided by Cisneros [25].

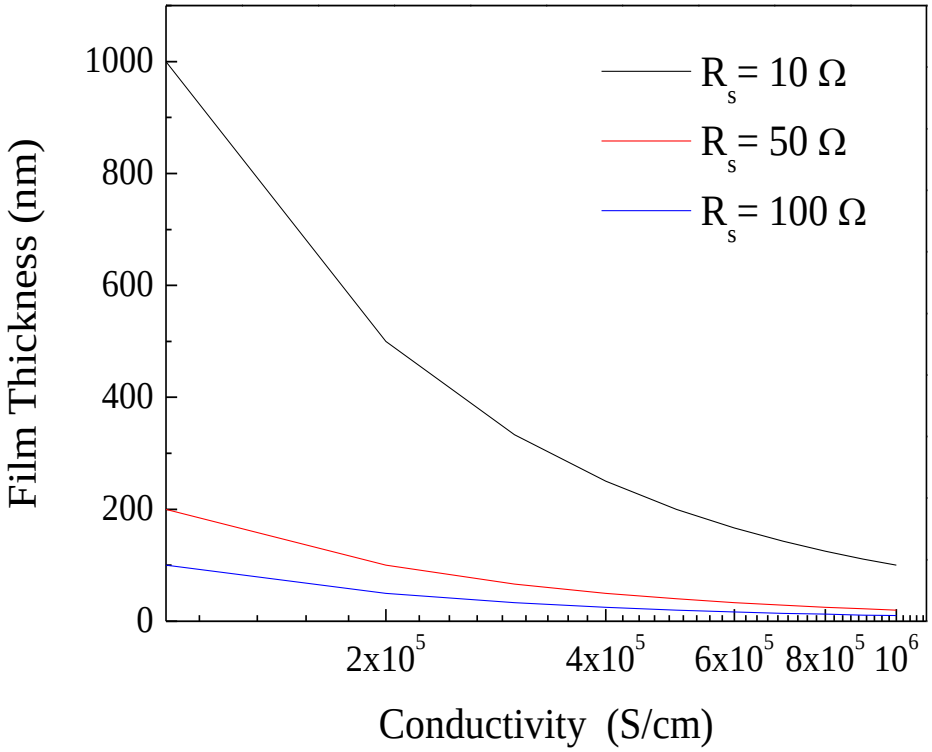

Figure 1.7: TCO film thickness as function of film conductivity.

2.4. Electrical Interface between TCO and Active Layers

The electrical interface between the TCO and the active layer in thin film solar cells strongly affects the solar cell performances [1, 26]. As a matter of fact, due to the small dimensions of the p layer, in the case of silicon based solar cells, the presence of trap states at the TCO/silicon interfaces affects the electrical parameters (lifetime and mobility) of carriers in the intrinsic layer and consequently the current-voltage (*I-V*) curve of the cell. The interface density of states (D_{it}) depends on growth mechanisms of TCO layer [27, 28]. The standard commercial values of D_{it} are in the range: 10^{20}-10^{22} cm^{-2} [29]. The monitoring of interface states is very important and it is based on Capacitance/Conductance-Voltage (*C/G-V*) and/or Capacitance/Conductance-frequency (*C/G-f*) measurements. In the last chapter experimental results will be presented on this topic.

2.5. Development of new TCO

While the development of new TCO materials is mostly dictated by the requirements of specific applications, low resistivity and low optical absorption are always significant pre-requisites. There are basically two strategies in managing the task of developing advanced TCOs that could satisfy the requirements. The main strategy dopes known binary TCOs with other elements, which can increase the density of conducting electrons. As shown in Table 1, more than 20 different doped binary TCOs were produced and characterised [30]. ITO was preferred, while AZO and GZO come close to it in their electrical and optical performance. Doping with low metallic ion concentration generates shallow donor levels, forming a carrier population at room temperature. Doping In_2O_3 with Sn to form ITO substantially increased conductivity. It is believed that substituting Sn^{4+} for In^{3+} provides carrier electrons, as Sn^{4+} is supposed to act as a one-electron donor. Similarly, aluminium is often used for intentional n-type doping of ZnO. Other group III impurities, such as Ga and B, and group IV such as Sn and Ge are also used. Doping by Al produced the relatively high conductivity AZO. Recently, AZO films with resistivity $\rho \sim 8.5.10^{-5}\,\Omega{\cdot}cm$ was reported by Agura *et al* [31] and recently by Addonizio *et al* [32]. An even lower resistivity was reported for GZO, $\sim 8.1.\ 10^{-5}\,\Omega{\cdot}cm$ [33-34].This ρ is very close to the lowest resistivity of ITO [35] of $7.7{\cdot}10^{-5}\,\Omega{\cdot}cm$, with a free carrier density of $2.5.10^{21}\ cm^{-3}$.

Table 1.1: TCO Compounds and Dopants

TCO	**Dopant**
ZnO	Al, Ga, B, H, In, F, Si, Ge, Ti, Zr, Mg, As
In_2O_3	Sn, Mo, Ta, W, Zr, F, Ge, Nb, Hf, Mg
CdO	In, Sn
SnO_2	Sb, F, As, Nb, Ta

The effort to increase the conductivity without degrading the transparency was paralleled by a more elaborate strategy in which phase-segregated, two-binary and ternary TCOs were synthesized and characterised (the strategy will not be discussed in this elaborate).

2.6. TCO Applications

TCO's have several industrial applications: the more important ones are going to be described in this section. TCO coatings are applied to transparent materials used for work surfaces and closet doors, particularly in clean rooms used for electronics assembly, in order to prevent harmful static charge build-up. In this application relatively high surface resistances (e.g. $k\Omega/\square$) can be tolerated.

Transparent heating elements may be constructed from TCO coatings. These are applied as defrosters in aircraft and vehicular windshields. Their advantage over traditional hot air blowers is that they have a much shorter effective defrosting time and they work uniformly over large areas. This application requires either the use of very low surface resistance coatings (e.g. ~ 1 $\Omega/\square$), or a high voltage power source. The application of TCO coatings to passenger vehicles was proven to be technically successful but a commercial failure, due to the high cost of a supplemental alternator to deliver the requisite high voltage. If the automobile industry will adopt a higher bus voltage, as already widely discussed, this application may then prove to be more commercially feasible in the future.

TCO coatings may be used as shielding to decrease electromagnetic radiation interference (EMI) from providing visual access. This may be to either to keep radiation from escaping an enclosure, to avoid interfering with nearby devices or detection, or from entering an enclosure to prevent external radiation sources from interfering with electronic devices. One potential example is the window of domestic microwave ovens which currently uses a perforated metal screen able to obscure clear visual observation and to reduce microwave leakage. Radiation leakage must be minimized to prevent harm to the users, as well as interference to proliferating wireless devices using the unlicensed spectral band at 2.45 *GHz*. While transparent conducting

films were already proposed 50 *years* ago, an attempt to introduce microwave windows with TCO coatings into the market was unsuccessful about 10 *years* ago, due to the high cost. Low cost designs are currently being developed.

The three largest applications of transparent conductive oxide thin films, in terms of the surface area covered and their total value are flat panel displays, solar cells and coatings on architectural glass. In general, transparent electrodes are needed for a large variety of electro-optical devices, of which flat panel displays and solar cells are the most important examples. In liquid crystal displays (LCDs) TCO films are needed for both electrodes in order to allow backlighting to pass through the liquid crystal film while applying voltage to the various pixels. Mostly, these electrodes are in the form of a pattern of lines with the alignment of the lines on the two electrodes perpendicular to each other. This allows addressing individual pixels by applying a voltage to the two lines intersecting at a given pixel. Thus, patterning the films is required.

The best LCDs utilises an active matrix comprising one amorphous silicon transistor occupying the edge of each pixel. As the silicon is opaque, this reduces the light transmission. Recently, transparent field effect transistors (FETs) have been developed based on the zinc oxide, but using a Cr gate.

Small and medium LCDs are a 25 *B$/yr* market which is growing by about 5*%/yr*, while large area LCDs have a similar market size and a much higher growth. The explosive growth of demand of ITO coatings for this specific application has generated widely spread concerns about Indium scarcity in the near future.

Most solar cells use TCO films as a transparent electrode. Major considerations in the choice of the TCO for this application, besides the conductivity and transparency, are electronic compatibility with adjacent layers in the cell, processing requirements and stability under environmental conditions. Often tin oxide based films are chosen for this application, as much as no patterning is required, but environmental stability is.

TCO films are commonly applied to architectural glass, often as part of multi layer tacks. The conductivity *per se* is usually irrelevant in window glass applications. Instead, the concurrent high infra-red reflectivity is exploited in order to obtain a proper light transmission in the visible range, while minimizing heat transmission. This feature is used to minimize air conditioning costs during summer and winter heating costs in buildings equipped with appropriate coated windows. Approximately 25% of flat glass is coated and energy

conserving coatings are now mandated in various regions. The coatings are mostly applied by two techniques. (1) Very enduring and inexpensive but simple, coatings are produced with atmospheric pressure chemical vapour deposition (APCVD), in line with the float glass production process. This assures a fresh surface and it exploits the high temperature of the glass during its production. However, APCVD is not very flexible and there are only limited options available for the coating architecture. (2) A more flexible but also more costly process is magnetron sputtering. Commonly multiple (e.g. 20-60) rotary targets are mounted in long modular vacuum systems (e.g. 40-160 *m* length) and multilayer stacks are deposited as the glass panels pass beneath the various cathodes, travelling at the speed of ~1 *m/s*. Typically these systems operate uninterruptedly for 2 *weeks* after which expended targets are replaced and other maintenances are performed.

In this PhD research activity, TCO layers will be deposited on glass substrates (Corning 1737) for application in thin film solar cells as front transparent and conductive oxide. The requirements, as reported in [4], are:

1) Good transparency in the visible region of solar spectrum (> 80-85%);
2) Good film adhesion to the glass substrate;
3) Low electrical resistivity ($< 10^{-3}\ \Omega \cdot cm$);
4) High surface roughness (RMS ~ 30-40 *nm*);
5) Low density of states at interface (D_{it}) with active layer.

The following chapters will deeply focus on all these aspects.

References

[1] A. Luque and S. Hegedus, Handbook of Photovoltaic Science and Engineering, Wiley: West Sussex, England (2003).

[2] M.A. Green, Thin-film Photovoltaics, in D.Y. Goswami (ed.), Advances in Solar Energy An Annual Review of Research and Development, New York: American Solar Energy Society, Inc., USA, pp. 187–214 (2003).

[3] A. G. Aberle, Thin Solid Films, 517, pp. 4706-4710 (2009).

[4] M. W. Rowell and M. D. McGehee, *Energy Environ. Sci.*, 4, pp. 131-134 (2011).

[5] M. A. Green, K. Emery, Y. Hishikawa, W. Warta and E. D. Dunlop, Prog. Photovolt: Res. Appl., 20, pp. 12-20 (2012).

[6] F. Meillaud, A. Feltrin, M. Despeisse, F –J. Haug, D. Dominé, M. Phthon, T. Soderstrom, P. Cuony, M. Boccard, S. Nicolay and C. Ballif, Sol. Energy Mater. Sol. Cells, 95, pp. 127-130 (2011).

[7] M. A. Green, K. Emery, Y. Hishikawa and W. Warta, Prog. Photovolt: Res. Appl., 16, pp. 61-67 (2008).

[8] K. Baedeker, Ann. Phys. (Leipzig), 22, p. 749 (1907).

[9] M. Schulte, K. Bittkau, K. Jäger, M. Ermes, M. Zeman, and B. E. Pieters, Appl. Phys. Lett., 99, pp. 111107-111107-3 (2011).

[10] C. Battaglia, J. Escarré, K. Söderström, L. Erni, L. Ding, G. Bugnon, A. Billet, M. Boccard, L. Barraud, S. De Wolf, F. J. Haug, M. Despeisse and C. Ballif, Nano Lett., 11, pp. 661-665 (2011).

[11] S. H. Lee, S. H. Han, H. S. Jung, H. Shin, J. Lee, J. H. Noh, S. Lee, I. S. Cho, J. K. Lee, J. Kim

and H. Shin, J. Phys. Chem. C, 114, pp. 7185-7189 (2010).

[12] S. E. Habas, H. A. S. Platt, M. F. A. M. van Hest and D. S. Ginley, Chem. Rev., 110, pp. 6571-6594 (2010).

[13] M. Afzaal and P. O'Brien, J. Mater. Chem., 16, pp. 1597-1602 (2006).

[14] K. Ellmer, A. Klein and B. Rech, Eds. Transparent Conductive Zinc Oxide; Springer Series in Materials Science; Springer-Verlag: Berlin, (2008); Vol. 104.

[15] C. Jagadish and S. J. Pearton, Eds, Zinc Oxide: Bulk, Thin Films and Nanostructures; Elsevier: Oxford, U.K., (2006).

[16] H. Mizoguchi and P.M. Woodward, Chem. Mater., 16, pp. 5233-5248 (2004).

[17] C.G. Van de Walle, Phys. Rev. Lett., 85, pp. 1012-1015 (2000).

[18] C. Kiliç and A. Zunger, Phys. Rev. Lett., 88, pp. 095501/1-095501/4(2002).

[19] J.R. Bellingham, W.A. Phillips and C.J. Adkins, J. Phys. Matter, 2, pp. 6207-6221 (1992).

[20] K. Ellmer, J. Phys., D, Appl. Phys., 33, pp. R17-R32 (2000).

[21] K. Ellmer, J. Phys., D, Appl. Phys., 34, pp. 3097-3108 (2001).

[22] G. Frank and H. Köstlin, Appl. Phys., A 27, pp. 197-206 (1982).

[23] P. Ebert, Z. Zhang, F. Kluge, M. Simon, Z. Zhang and K. Urban, Phys. Rev.Lett., 83, pp. 757-760 (1999).

[24] T. Pisarkiewicz, K. Zakrzewska and E. Leja, Thin Solid Films, 174,pp. 217-221 (1989).

[25] J. I. Cisneros, Applied Optics, 37, pp. 5262-5270 (1998).

[26] C. Casteleiro, H.L. Gomes, P. Stallinga, L. Bents, R. Ayachi, R. Schwarz, J. Non-Cryst. Solids, 354, pp. 2519-2522 (2008).

[27] R. Romero, M.C. López, D. Leinen, F. Mart´ın, J.R. Ramos-Barrado, Mat. Sci. Eng. B, 110, pp. 87-93 (2004).

[28] G. Cannella, F. Principato, M. Foti, C. Garozzo, S. Lombardo, Energy Procedia, 3, pp. 51-57 (2011).

[29] T. Minami, Semicond. Sci. Technol. 20, pp. S35-S44 (2005).

[30] J.R. Bellingham, W.A. Phillips and C.J. Adkins, J. Phys. Matter, 2, pp. 6207-6211 (1992).

[31] H. Agura and H. Suzuki, T. Matsushita, T. Aoki and M. Okuda, Thin Solid Films, 445, pp. 263-267 (2003).

[32] M. L. Addonizio, A. Antonaia, Thin Solid Films, 518, pp. 1026-1031 (2009).

[33] S.-M. Park, T. Ikegami and K. Ebihara, Thin Solid Films, 513, pp. 90-94 (2006).

[34] J. K. Kim, J. M. Lee, J. W. Lim, J. H. Kim and S. J. Yun, Jpn. J. Appl. Phys., 49, pp. 04DP09-04DP09-4 (2010).

[35] H. Ohta, M. Orita, M. Hirano, H. Tanji, H. Kawazoe and H. Hosono, Appl. Phys. Lett., 76, pp. 2740-2742 (2000).

CHAPTER 2

Sol-Gel Technology

As already said in the previous Chapter the main goal of this PhD activity is the investigation of the Sol-Gel (Solution-Gelation) deposition method as a low-cost technique for TCO deposition on glass substrate. This chapter is organized in two main parts. The first part describes the Sol-Gel route, while the second part examines in-depth and critically the ZnO synthesis. Hereafter, the specific approach adopted during the researches is presented.

There are many technologies for the production and the deposition of TCO coatings. The more common used technologies are chemical vapour deposition and sputtering. A wide overview of TCO sputtering equipment and CVD coaters can be found in [1]. Here below some features of these so-called "traditional techniques" are given.

The *Atmospheric Pressure Chemical Vapour Deposition* (APCVD) technique allows producing electrical conductive layers on large areas at a float glass drawing velocity of 9 *m/min*. In this process precursors are dissolved either in organic or in inorganic solvents and they are scattered in a carrier gas like nitrogen. Subsequently, they are supplied to the float glass at a temperature between 500°C and 700°C [2]. The main advantage of this process is that being carried out at an atmospheric pressure it is cheaper than vacuum-based deposition technologies. This kind of method is widely used by companies such as Nippon Sheet Glass, Pilkington, AFG Industries and Saint Gobain. However, it is important to underline that deposition equipments are very expensive and that a high temperature is required during the process. Oerlikon, one of the world's leading high-tech industrial groups, recently introduced another possibility for producing optimized light scattering for so-called "*micromorph cells*" by applying the LPCVD (low pressure CVD) technique). Typically, boron-doped ZnO thin films are deposited at a low pressure with diethyl zinc, water vapour and diborano as a doping gas [3]. The deposition takes place at ~ 50 *Pa* at a substrate temperature of approximately 200°C.

An alternative to CVD based technologies is represented by the sputtering method.

This technique allows obtaining a proper film adhesion as well as a fine control of thickness and morphology of the different layers. Some drawbacks are the need for high process temperatures, the use of volatile molecular precursors, a poor control of the film stoichiometry, the use of complex equipments requiring high maintenance costs and the dissipation of a large amount of energy.

1. Sol-Gel Method

Sol-Gel technology is a remarkably versatile approach in making materials.

In Sol-Gel chemistry nanometre-sized particles are first formed and then connected with one another in order to create a three-dimensional (3D) solid network. Such a technique allows scientists to change both the composition and the structure of materials on the nanometre scale (unit of length equal to one billionth of a metre). In order to produce Sol-Gel materials in different forms such as powders, films, fibres and freestanding pieces of material called monoliths, a variation to this process can be realised.

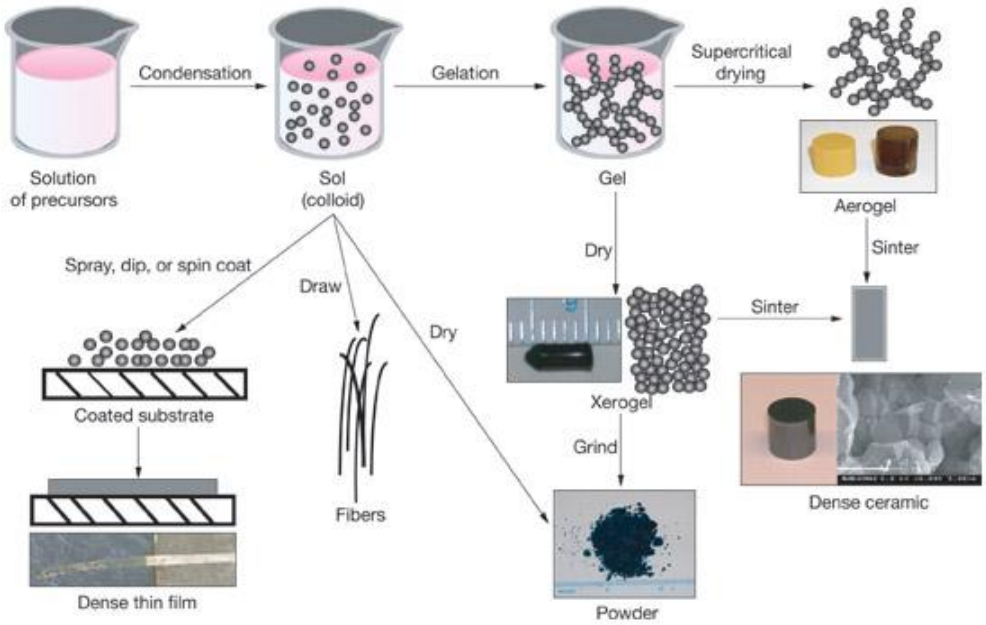

Figure 2.1: Sol-Gel Process.

This technique involves the transition of a system from a colloidal liquid called sol into a solid gel phase [4]. The Sol-Gel method offers many advantages, among them the low process temperature, the homogeneity of the final product up to atomic scale, the ability to control the composition on molecular scale and the low costs of employed materials and technologies. The Sol-Gel process allows obtaining high quality films up to micron thickness, difficult to obtain using the physical deposition system. Moreover, it is possible to synthesise complex composition materials, to form higher purity products through the use of high purity reagents and to provide coatings over complex geometries [4].

The starting materials used during the preparation of the sol are usually inorganic metal salts and metal organic compounds. The sol formation takes place by hydrolysis and polycondensation reactions [4, 5]. A further processing of the sol enables to produce ceramic materials in different forms. In particular thin films can be made by dip-coating or spin-coating. When the sol is cast into a mould, a wet gel is formed. By drying- and heat-treatments, the gel is converted into dense ceramic or glass materials. If the liquid in a wet gel is removed under a supercritical condition a highly porous and extremely low density aerogel material is obtained. As the viscosity of a sol is adjusted into a suitable viscosity range, ceramic fibres can be drown from the sol. Ultra-fine and uniform ceramic powders are formed by precipitation, spray pyrolysis or by emulsion techniques.

2. The chemistry of Sol-Gel

2.1 The Gelation Process

Generally the most preferred starting reagents are alkoxides ($M_x(OR)_y$) - where M is the element with valence y and OR the alkoxide group. As a matter of fact, they exhibit useful properties to control chemical synthesis of oxides. The transition from sol to gel involves two key steps: hydrolysis and polycondensation.

Hydrolysis, a step in the degradation of a substance, takes place by the addition of small quantities of water. Non-aqueous solvent such as alcohol are usually used in order to obtain a homogenous solution. In the hydrolysis reaction the alkoxide groups (OR) are replaced by hydroxyl groups (OH) [6]:

$$M(OR)_n+H_2O = M(OH)(OR)_{n-1}+ROH$$

The hydrolysis rate is determined by many factors. Indeed, an increase in the charge density on the metal, the number of metal ions bridged by a hydroxo- or oxo-ligand and the size of the alkyl groups [7, 8] contribute to cause a reaction. On the contrary, the reverse reaction (esterification) tend to occur during inhibition (as the number of hydroxo-ligand coordinating M increases) or when pH, temperature, water and solvent concentration. For what metal oxides are concerned, thanks to their high electronegativity compared to the metal, the M-O-M bonds are highly polarized and the hydrolysis rates are high. On the contrary, the hydrolysis rates of non-metal alkoxides are slower.

This is very important for multi-component systems where the different hydrolysis rates of the precursors give to different gelation times. In this case a non-homogeneous gel is formed. Many solutions can be adopted in order to solve this problem. These could be:

1) The use of double alkoxides with a precise stoichiometry
2) A modification of the hydrolysis rate of the more reactive precursor using reaction inhibitors
3) A modification of the hydrolysis rate of the slower precursor by a catalysed pre-hydrolysis (acid or basic).

The polycondensation reactions occur at the same time of the hydrolysis leading either to the disappearance of a water molecule [6]:

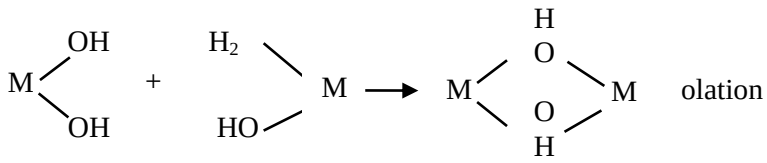

$$M\text{-}OH + M\text{-}OH \rightarrow M\text{-}O\text{-}M + H_2O \quad \text{oxolation}$$

or to the disappearance of an alcohol molecule:

$$M\text{-}OH + M\text{-}OR \rightarrow M\text{-}O\text{-}M + H_2O$$

In any case hydroxyl or oxygen bridges are formed leading to condensed species. At the end of the process all oxygen atoms are bridging oxygen atoms and a hydrated oxide network is obtained.

3. Dip-Coating Technique

One of most interesting feature of the Sol-Gel technique is its possibility to employ the homogeneous solution obtained before the gelation in order to prepare thin films by the deposition of spin and dip-coating. Sol–Gel films can be prepared by using either a dip-coating or a spin-coating deposition procedure. Although the latter easily allows the deposition of more layers, it is only suitable for Newtonian fluids and circular substrates. Furthermore this procedure requires stringent solvent properties such as a proper viscosity and is more exposed to contamination problems. Dip-coating, instead, allows easy coating of samples of any size or shape, it reduces contaminations and it is less sensitive to solvent or solution properties. Based on all the above reasons, it was decided to limit the investigation only to dip-coating deposited films. The used dip-coater is shown in Figure 2.2.

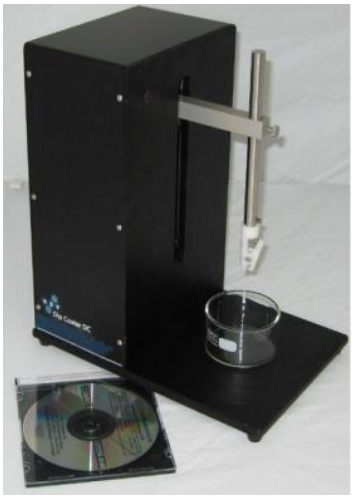

Figure 2.2: Used KSV dip-coater.

The dip-coating techniques can be described as a process where the substrate to be coated is immersed in a liquid and then withdrawn with a well-defined speed under controlled temperature and atmospheric conditions. The coating thickness is mainly defined by the withdrawal speed, the solid content and the viscosity of the liquid. If the withdrawal speed is chosen, such that the sheer rates in the Newtonian regime, the coating thickness can be calculated by the Landau-Levich equation [9]:

$$t = 0.94 \frac{(\eta \cdot v)^2}{\gamma_{LV}^{1/6} \cdot (\rho \cdot g)^{1/2}} \qquad (2.1)$$

Where

- t is the film thickness
- η is the solution viscosity
- v is the withdrawn speed
- γ_{LV} is the liquid-vapour surface tension
- ρ is the solution density
- g is the gravity

As shown by James and Strawbridge [10] for an acid catalysed silicate sol, the thickness obtained through the experiment fits very well the calculated one with the previous equation. Choosing an appropriate viscosity the coating thickness can be varied with high precision from 20 *nm* up to 50 μm while maintaining a high optical quality. The stages of a dip-coating process are shown in Figure 2.3.

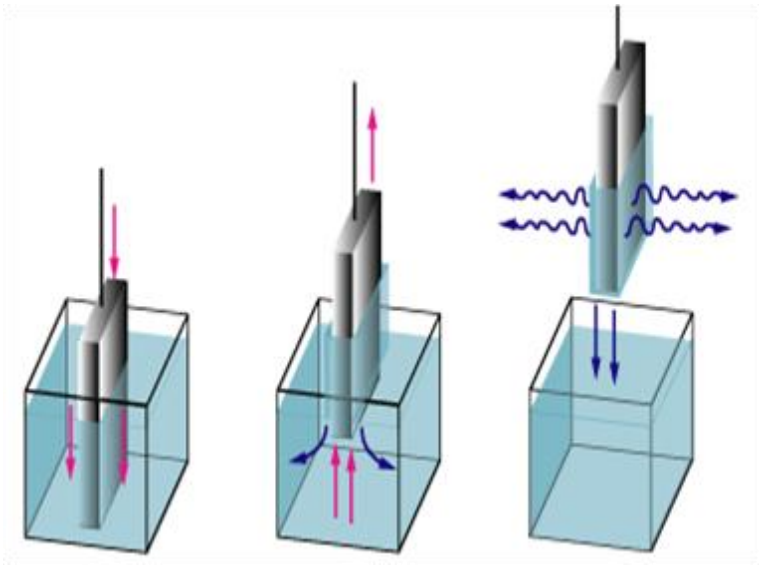

(a) **(b)** **(c)**

Figure 2.3: Stages of the dip-coating process: **(a)** dipping of the substrate into the coating solution; **(b)** wet layer formation by withdrawing the substrate; **(c)** gelation of the layer by solvent evaporation.

In the fourth chapter, some experimental results to optimise the film thickness using the Landau-Levich equation are discussed.

If reactive systems are chosen for coatings as in the case of ZnO Sol-Gel synthesis the control of the atmosphere is indispensable. The atmosphere controls the evaporation of the solvent and the subsequent destabilization of the sols by solvent evaporation. Moreover it leads to a gelation process and to the formation of a transparent film due to the small particle size in the sols (nanometres range) [11].

Largely, sol particles are stabilised by surface charges. The stabilization condition follows the Stern's potential consideration [12]. According to Stern's theory the gelation process can be explained by the approaching of the charged particle to distances below the repulsion potential. Then the repulsion is changed to an attraction leading to a very fast gelation. The resulting gel then has to be densified by a thermal treatment, and the densification temperature is depending on the composition. Unfortunately due to the small size of the gel particles the system presents a large excess of energy. In many cases a remarkably reduced densification temperature compared to bulk-systems is observed.

4. ZnO Sol-Gel Synthesis

As firstly discussed the knowledge of the synthesis of ZnO films through evaporation techniques has reached a solid level of knowledge [13, 14]. Recently, the Sol-Gel route has progressively been proposed as a cost-effective alternative to vacuum-assisted deposition techniques. It is a low temperature wet chemical process characterised by a very high versatility as it allows controlling chemical composition, shape, structure, textural and morphological properties of final materials by adjusting processing parameters. Moreover, Sol-Gel allows coating large area of arbitrary shaped substrates.

The Sol-Gel procedure is constituted essentially by five main steps as shown in Figure 2.4.

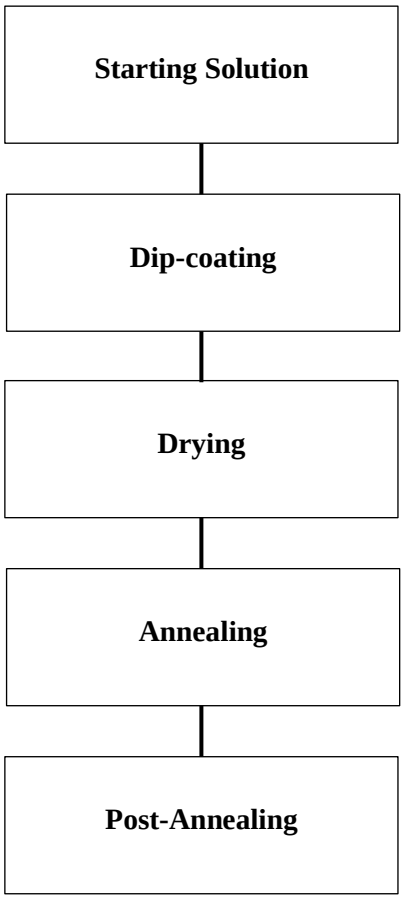

Figure 2.4: Scheme of the Sol-Gel procedure.

The first step is the preparation of the starting solution, also named Precursor Solution as it contains the precursors of the materials. The starting solution strongly affects the film properties. In particular, the film thickness, the grain size as well as the electrical and the optical properties.

This research tackles the issue of the optimization of the starting solution with the attempt to optimize the films properties.

4.1 Starting Solution – Used Approach

4.1.1. General Problem

The key aspect of any wet synthesis of ZnO is the simultaneous control of the hydrolysis equilibrium of Zn^{2+} and the solubility of $Zn(OH)_2$. The formation of zinc oxide in aqueous environment can be described by the following reactions [15].

$$Zn^{2+}_{(aq)} + H_2O \rightleftarrows Zn(OH)^{+}_{(aq)} + H^{+}_{(aq)} \quad (2.2)$$

$$Zn(OH)^{+}_{(aq)} + H_2O \rightleftarrows Zn(OH)_{2(aq)} + H^{+}_{(aq)} \quad \mathbf{(2.3)}$$

$$Zn(OH)_{2(aq)} \rightleftarrows Zn(OH)_{2(s)} \quad (2.4)$$

$$Zn(OH)_{2(s)} \rightleftarrows Zn^{2+}_{(aq)} + 2OH^{-}_{(aq)} \quad (2.5)$$

$$Zn(OH)_{2(aq)} + OH^{-}_{(aq)} \rightleftarrows Zn(OH)_3^{-}{}_{(aq)} \quad (2.6)$$

$$Zn(OH)_3^{-}{}_{(aq)} + OH^{-}_{(aq)} \rightleftarrows Zn(OH)_4^{2-}{}_{(aq)} \quad (2.7)$$

Equilibrium (2.4) is strongly shifted towards right (K~10^6) as a consequence of the very low solubility of $Zn(OH)_2$ into water (K_{sp} = 3.5 10^{-17} at 25°C). Therefore, as shown by the equations, it is not easy to hydrolyse Zn^{2+} without precipitation of zinc hydroxide. On the other hand, it is evident that the above equilibria are strongly influenced by the pH value at 25°C. In acidic conditions (pH < 6), Zn^{2+} is the main ion present in the solution. In neutral or slightly basic conditions the most part of Zn is present in its solid forms $Zn(OH)_2$ or ZnO because both of them have a very low solubility in this range of pH. At pH 12 level or above the main zinc specie is $Zn(OH)_4^{2-}$[15].

Since the Sol-Gel synthesis of ZnO involves the preparation of a colloidal solution of a molecular precursor of Zn that is then hydrolysed and that the production of oxo-hydroxylated species whose polycondensation originate the Zn-oxo colloidal particles the problem of avoiding the precipitation of $Zn(OH)_2$ is crucial. Different approaches proposed to solve this problem were analysed in two recent papers [16, 17].

Spanhel and Anderson [18], have successfully prepared for the first time a stable colloidal solution of ZnO starting from a diluted solution (about 0.1 M) of zinc acetate dehydrate [ZAD: $Zn(CH_3COO)_2 \cdot 2H_2O$] in absolute ethanol [EtOH: CH_3CH_2OH] using drastic conditions (reflux at 80°C for 180 *min*) followed by the addition of a well-defined amount of lithium hydroxide hydrate ($LiOH \cdot H_2O$). Afterwards, many variations of that procedure, concerning either different process parameters or different solvents and complexing agents, have been presented. Ohyama et al. [19, 20], starting from the same precursor, ZAD, and by using an alcohol of high molecular weight as solvent, 2-methoxyethanol [2-ME: $CH_3O(CH_2)_2OH$] in addition to the use of two complexing agents of Zn^{2+}: monoethanolamine [MEA: $(HOCH_2CH_2)NH_2$] and diethanolamine [DEA: $(HOCH_2CH_2)_2NH$] have achieved a more concentrated solution, [Zn^{2+}] = 0.6 M. This allowed preparing the homogeneous solution of the precursor from which the films of ZnO are obtained in milder conditions (30 *min* at 60°C). The mean thickness of the films was about 40 *nm* after a single dip. A wide concentration range of the [Zn^{2+}], ranging from = 0.05 to 1 M, was explored by Znaidi et al. [21, 22], using ZAD as precursor, EtOH and 2-ME as solvents, MEA, triethanolamine [TEA:$(HOCH_2CH_2)_3N$] and lactic acid as complexing agents. The hydrolysis was carried out in both drastic (refluxing at 80°C for 120-180 *min*) and mild (120 *min* at 60 °*C*) conditions. The above solutions allowed ZnO films formation either by spinnig or by dip-coating, whose mean

thickness, after a single coating step, was about 20 *nm*. Kim et al. [23] employed isopropanol [i-PrOH: $(CH_3)_2CHOH$], a solvent with a boiling point lower than 2-ME, and MEA to prepare ZAD solutions with different $[Zn^{2+}]$ ranging from 0.3 to 1.3 M, that were hydrolyzed at 50°C for 60 *min*. O'Brien et al. [24-26] prepared ZnO films by employing a Sol-Gel route similar to the one proposed by Kim et al. [23] but starting from a different Zn molecular precursor, the anhydrous zinc acetate. After a first single coating step films with different thickness were obtained. This depended on the initial $[Zn^{2+}]$ concentration ranging from 84 *nm* ($[Zn^{2+}]$=0.3 M) to 437 *nm* ($[Zn^{2+}]$=1.3 M). The transparency of the films in the UV-Vis range was found to be strongly affected by the thickness [24]. Dutta et al. [27], starting from ZAD, iPrOH and DEA, achieved ZnO films from highly diluted solutions, $[Zn^{2+}]$ ranging from 0.03 to 0.1 M, but using hydrolyzed at a room temperature. Tsay et al. [28] employed EtOH and MEA to prepare ZAD solutions with $[Zn^{2+}]$=0.75 M hydrolyzed at 60°C for 120 *min*.

As the above explanations show, it is evident that the control of the hydrolysis and solubility equilibria (equations 2.2 - 2.7), were obtained by combining the effects of both complexing agents and temperature.

In this PhD activity, I have developed an innovative approach to solve this problem by working at room temperature. Moreover, the effect of the solution pH on film properties has been deeply investigated. The adopted approach is explained in the next paragraph.

4.1.2. The Role of Additives

In my approach, the used Zinc precursor is ZAD (Zinc acetate dehydrate – 99.999% purity, purchased from Sigma-Aldrich) that is the most suitable molecular precursor due to its low cost, its "ease of use" and its commercial availability. As a matter of fact, the acetate group, as contaminant of the gel, is easily removable during the post-treatments of annealing and it acts at the same time as a stabiliser on the colloidal sol. Finally, the hydration water molecules of ZAD allow hydrolysing Zn^{2+} ions without any further addition of water. The

employed solvent is EtOH (anhydrous ethanol provided by Fluka) that was selected as solvent due to its high dielectric constant, low boiling point and non-toxicity.

ZAD has a limited solubility in EtOH at room temperature. A stock solution with [ZAD]=0.12 M (S0) and pH=6.5 was successfully prepared. According to equilibria (1)–(4), this pH value shows that it is not possible to prepare more concentrated [Zn^{2+}] solutions without stabiliser agents. On the basis of this solution amorphous thin films were achieved. ZnO films (F0) were obtained by annealing in air at 600°C for 2 *h* the dried films. F0 films showed: a very high optical transparency (93% in the visible range), a high electrical resistivity (about $10^4\ \Omega \cdot cm$), a very low average size of ZnO nanocrystals (10 *nm*) and a low film thickness (about 50 *nm*). As it is well known, the film thickness depends on both withdrawal speed, on both density and viscosity of the precursor solution [29]. Consequently, more concentrated solutions of the precursor are required to increase the film thickness. This goal involves a proper control of both hydrolysis and solubility equilibria (equations 2.2 - 2.5), needed to avoid the precipitation of the zinc hydroxide. Such a control can be obtained by exploiting chemical species with one or more functional groups, such as alkanolamines or carboxylic acids which can act either as base or as acid and/or as chelating agents [16, 17].

In order to better understand the role of these additives on the synthesis procedure and their influence on the final properties of ZnO films two stock solutions of ZAD with molar concentration 0.50 M were prepared. One containing HAc (acetic acid by Sigma-Aldrich) (S1), the other containing TEA (triethanolamine – 98% purity and provided by Sigma-Aldrich) (S2). HAc decreases the pH of the solution (pH=4.7) shifting to left equilibria 2.1 and 2.2 and to right equilibrium 2.5. It provides acetate ions that act as complexing agents for zinc ions (see Scheme 2.1).

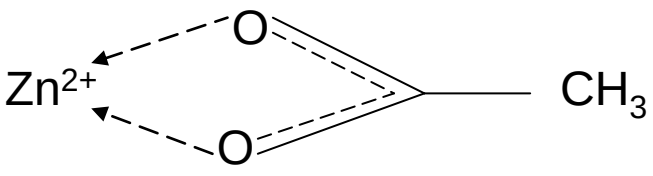

Scheme 2.1: Acetate ion acts as bidentate ligand for the zinc ion.

Therefore, HAc influences both equilibria 2.2 and 2.3 as well as the condensation equilibria between oxo-acetate species belonging to growing oligomers of Zn oxohydroxylated species [30]. On the other hand, TEA increases the pH of the solution (pH=6.8) shifting to right equilibria 2.2 and 2.3 and to left equilibrium 2.5. Moreover it plays a strong complexing action being a tetradentate ligand for zinc ions (see Scheme 2.2).

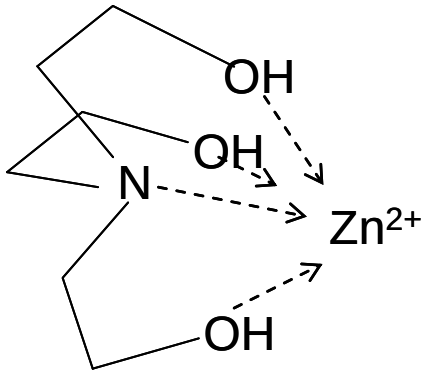

Scheme 2.2: Triethanolamine acts as tetradentate ligand for the zinc ion.

It should be noticed, however, that the preparation of S1 required a heating step at 50°C for 1 *h* to get the complete homogenisation. Instead, the preparation of S2 was wholly performed at room temperature. This confirms the greater chelating efficiency of TEA with respect to HAc. For this question, in this research TEA has been used to control the ZnO synthesis while HAc has been only used for a comparative study.

Stock solutions more concentrated than 0.50 M were prepared by using TEA as additive (see Table 2.1), and ZAD. TEA molar ratio was kept constant at 1. As it can be noticed from Table 2.1, by increasing the TEA amount both the pH and the chemical stability of the solution rise, too. All solutions are stirring at room temperature for 1 *h*, before film deposition.

Table 2.1: Composition, molar concentration and pH of ZAD stock solutions in anhydrous ethanol with the related labels.

Stabilizers		**Stock solutions**				
-	S0					
HAc		S1				
TEA		S2	S3	S4	S5	S6
Concentration ***mol·L*$^{-1}$**	0.12	0.50	0.60	0.75	1.0	1.2
pH	6.5	4.7 6.8	7.1	7.4	7.66	7.8

*4.1.3.*The Role of the pH Level

As equilibria 2.2 – 2.7 show, when the concentration of OH^-, i.e. pH is low, the growth of ZnO particle does not proceed because of the lack of $Zn(OH)_2$ formation in the solution [31]. As a consequence, in Sol–Gel technique there is a strong influence of the pH level on the products nanostructure.

During this PhD research activity, solutions with a pH ranging from 4.5 to 10 were prepared. Since pH controls the rate of ZnO formation, it also affects the size and their way of combination to get stable state [31]. As the freshly formed nuclei in the solution are unstable, a tendency to grow into larger particles is expected. When solutions with pH lower than 7 are prepared, ZnO thin films with a low grain size are expected.

Moreover, a further increase in the concentration of OH^- (pH>9.0) reduces the crystallite size of ZnO, as shown in [31, 32]. This is probably because of the dissolution of ZnO (back reaction of equilibrium 2.6). The decrease in crystallite size above 9.0 pH level is due to the acceleration of ZnO dissolution during competitive

ZnO formation. The pH value of the sols was adjusted to the desired value using ammonia solution (33% in water) provided by Fluka and it has been measured by using the Mettler Toledo pH-metre.

Ammonia solution increases the pH of the solution, shifting to right equilibria 2.2 and 2.3 and to left equilibrium 2.5.

All along this work, the effect of pH on film properties at a fixed molar concentration of Zn precursor was investigated. In particular, solutions at four pH levels were prepared. All prepared solutions are stable from about six months. The obtained sols were stirred for 60 *min* at room temperature. The solutions with the respective pH value are listed in Table 2.2.

Finally, it is to be considered that in the case of S9 solution the TEA/Zn molar ratio is equal to 3 instead of 1, as in the case of all other solutions. This is fundamental criteria for the film formation. In fact, the TEA amount in the solution strongly affects the sol viscosity and therefore films uniformity and homogeneity. In S9 solution the ammonia amount is very high. Experimental results show that in the case of 1.0 TEA/Zn molar ratio film formation does not occur. An increase to 3.0 TEA/Zn molar ratio is required. From this solution films are not be deposited, because the high pH level hinders the multi-deposition process[31] and because of the different TEA/Zn molar ratio. It was prepared only to understand the operating upper limit in the pH level.

Table 2.2: Composition, molar concentration and pH value of the solution prepared with ammonia.

Stabilizers	**Stock solutions**		
TEA	S7	S8	S9
Concentration $mol \cdot L^{-1}$	1.0	1.0	1.0
pH	8.12	8.76	9.71

4.1.4. Boron and Aluminium Doping

Boron doped ZnO thin films were obtained from starting solution containing the Zinc and the Boron precursors. The used precursor for the *Boron* is the Acidic Boron (H_3BO_3 – 99.8% purity), provided by Carlo Erba, thanks to its low cost, wide availability and facility of use. Solutions in nominal atomic ratio of the B/Zn (0.5%, 0.8% and 1%) were prepared by stirring at room temperature for 1 *h*. The molar concentration and the composition of the solutions are reported in Table 2.3. The effect of Boron on ZnO films will be deeply analysed in the last chapter of this work.

Table 2.3: Composition of ZAD solutions doped by Boron.

Stabilizers	**Stock solutions**		
TEA	S10 – S12	S13 – S15	S16 – S18
Concentration ***mol·L*** $^{-1}$	0.5	0.75	1.0
B/Zn (%)	0.5, 0.8 and 1	0.5, 0.8 and 1	0.5, 0.8 and 1

Besides, studies on the effect of Aluminium doping were carried out. The used Al precursor is the anhydrous Aluminium Chloride ($AlCl_3$ – 99.999% purity) provided by ABCR GmbH & Co. Several doped solutions with 0.8% and 3% atomic percentage starting from solutions S8 were prepared. These solutions were named S8b (Al – 0.8%) and S8c (Al – 3%). Lastly, some boron doped solutions with the addition of an atomic percentage equal to 0.8% in S7 and S8 solutions were prepared. These solutions were named S7b and S8d.

4.2. Film Deposition

4.2.1. Glass Substrates

The second step of a Sol-Gel procedure is the deposition of the solution on the glass substrates. During this study, Sol–Gel ZnO thin films were deposited on glass substrates (Corning 1737) with the use of the dip-coating process (see Figure 2.5).

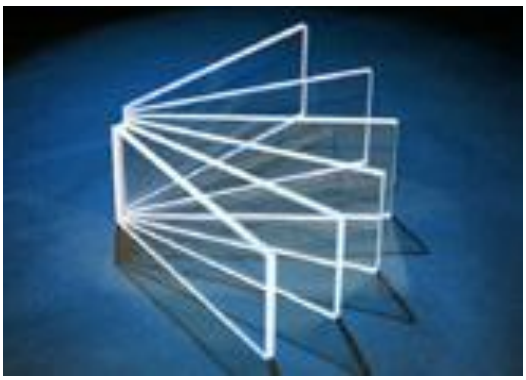

Figure 2.5: Corning 1737.

These substrates are alkaline earth boro-aluminosilicate glasses with softening ($10^{7.6}$ *poise*) and strain ($10^{14.5}$ *poise*) points at 975°C and 666°C, respectively. The optical properties of these substrates are highlighted in the here below Figure 2.6.

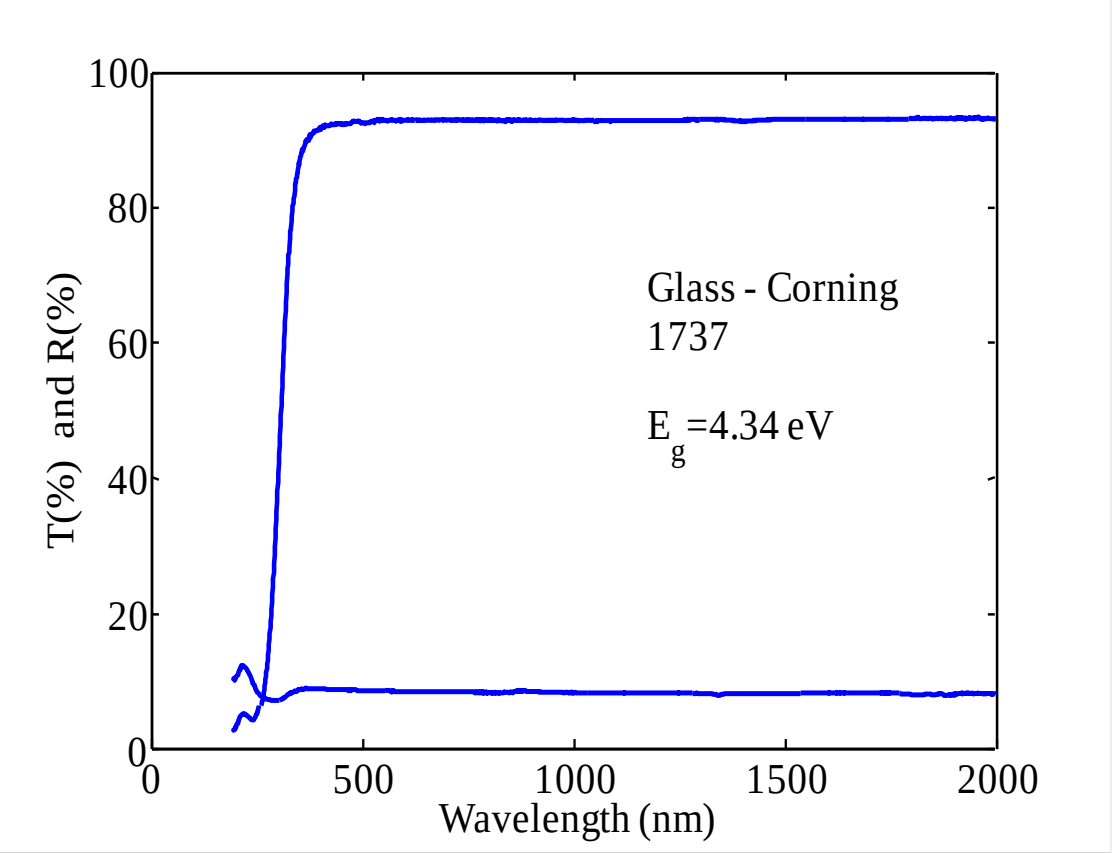

Figure 2.6: Optical properties of Corning 1737 glass substrates.

Films were prepared at room temperature by means of a KSV dip-coater. The glass substrates were dipped into the stock solution and withdrawn at 10 *mm/min*. In order to obtain good-quality films it is mandatory to optimise the wettability of the substrate compared to the sol.

Hence, different chemical etching procedures were applied to the glass substrates in order to select the one corresponding to the lower Water Contact Angle (WCA). The WCA values were measured using a Dataphysics OCA 20. Glass substrates were first cleaned with detergent solution and then subjected to different etching solutions: (a) Piranha solution (H_2SO_4:H_2O_2=3:1 by volume), (b) three NaOH solutions, with concentration 0.25, 0.50 and 0.75 M, for two different times (5 or 15 *min*), at room temperature. After that the substrates were rinsed with ethanol.

WCA values measured after each etching procedure are displayed in Table 2.4. The best surface wettability was obtained by NaOH etching 0.75 M for 15 *min*. Consequently, each glass substrate was treated at the same way before film deposition. The cleaning procedure is reported in Figure 2.7.

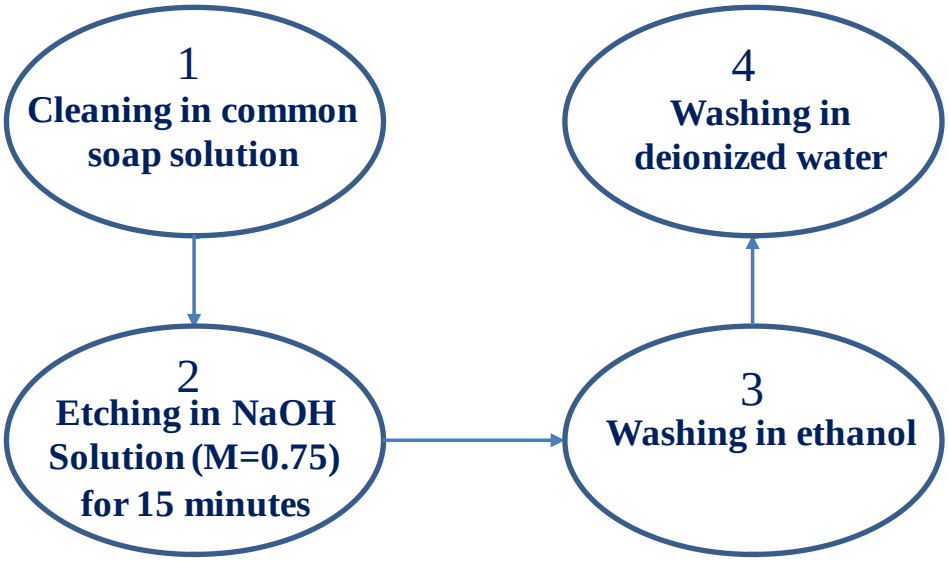

Figure 2.7: Cleaning treatment for glass substrates.

The effectiveness of the treatment was also confirmed by the adhesion tests performed on ZnO films deposited on either untreated or treated glass substrates. The highest adhesion force (140 kg/cm^2) was measured on the glass etched in NaOH 0.75 M for 15 *min*, whereas films deposited on untreated substrates showed an adhesion force of 60 kg/cm^2. This result confirms that better substrate wettability gives a stronger ZnO film adhesion.

Finally, thickness measurements showed that in the case of NaOH etching (0.75 M for 15 *min*) the film thickness was higher, according with Landau-Levich equation (Equation 2.1). This was due to a reduction of liquid-vapour surface tension. The experimental values are reported in Table 2.4. They refer to films deposited from S5 Solution.

The film adhesion was tested through the Z-axis pull stud method thanks to a Sebastian Five-A instrument and film thickness was measured by a KLA Tencor P-10 surface profiler.

Table 2.4: Water Contact Angle (WCA) values of the glass substrates subjected to different etching procedures and film thickness. WCA of common soap cleaned glass was 39 degrees.

Etching solution	**Piranha**[a]		**NaOH 0.25 M**		**NaOH 0.50 M**		**NaOH 0.75 M**	
Time of etching Min	5	15	5	15	5	15	5	15
WCA Degrees	27	22	25	20	19	16.5	17.1	13
Film Thickness (*nm*)	95	99	103	108	110	115	117	120

[a] H_2SO_4:H_2O_2 = 3:1 by volume

4.3. Heating Treatments

Heating treatments are very important in any Sol-Gel procedure as they strongly affect the film properties, such as the crystal structure, the electrical resistivity and the optical transmittance.

First of all, the deposited films were dried in air at 100°C for 2 *h*, in order to remove the solvent and then subjected to different heat-treatments. This second step is named "*annealing*" and it is very important because the film crystallisation depends on the time and on the temperature of this treatment. The effect of annealing time and temperature on film properties was largely investigated all along this PhD research activity and results will be shown in the last chapter. Table 2.5 displays the annealing temperature, time and environment to which the studied films have been subjected.

Table 2.5: Heat treatments performed on the studied films.

Annealing temperature °C	600			550			500		
Annealing time (*h*)	2	1	0.5	2	1	0.5	2	1	0.5
Environment	Air			Air			Air		
Stock Solutions	**Films**			**Films**			**Films**		
S0	F0	-	-	-	-	-	-	-	-
S1	F1	-	-	-	-	-	-	-	-
S2	F2	-	-	-	-	-	-	-	-
S3	F3	-	-	-	-	-	-	-	-
S4	F4	-	-	-	-	-	-	-	-
S5	F5	F7	F8	F9	F10	F11	F12	F13	F14
S6	F6	-	-	-	-	-	-	-	-
S7-S18	-	-	F15/F26	-	-	-	-	-	-
S8b, S8c	-	-	F8b, F8c	-	-	-	-	-	-
S7c, S8d	-	-	F7c, F8d	-	-	-	-	-	-

As discussed in the previous chapter, ZnO is a wide bandgap semiconductor and its electrical resistivity is expected to be very high, in particular in the case of gel derived ZnO films that have a high stoichiometry. In order to reduce the electrical resistivity, heat-treatments in reductive environments were performed. In this case, the oxygen vacancy density was expected to increase with the subsequently reduction of the electrical resistivity

(this point will be deeply analysed in the chapter 3). The above situation suggests to subject gel derived films to a post-annealing treatment in an inert or reductive environment.

Therefore, some selected films were post-annealed in nitrogen or forming-gas (FG) (mixture H_2 – He balance) at different temperatures (250, 400, 450, 500, 550 and 600°C) and for different time (0.5, 1, 1.5 and 2 *h*). Moreover, studies on the effect of the Hydrogen content (2, 3, 5, 10 and 15%) in the mixture on the film conductivity were carried out. The experimental results will be presented in the last chapter.

5. Synthesis of ZnO Multi layer

In any Sol-Gel procedure a simple way to increase the film thickness is the reiteration of the deposition procedure. The adopted procedure is reported in Figure 2.8. As shown, the films deposited on the glass were dried in air for 10 *min* at 100°C and then heated in air for 10 *min* at 400°C throughout two consecutive depositions. This last step is named "*pre-annealing*" and it is required for TEA removal and for film densification in order to enhance the film uniformity, its morphology and to reduce the residual porosity. Finally, n-layered films were annealed at 600°C for 0.5 *h* (for the crystallisation) in air and then post-annealed in FG (H_2 5*%* - He balance) for 0.5 *h* at 450°C.

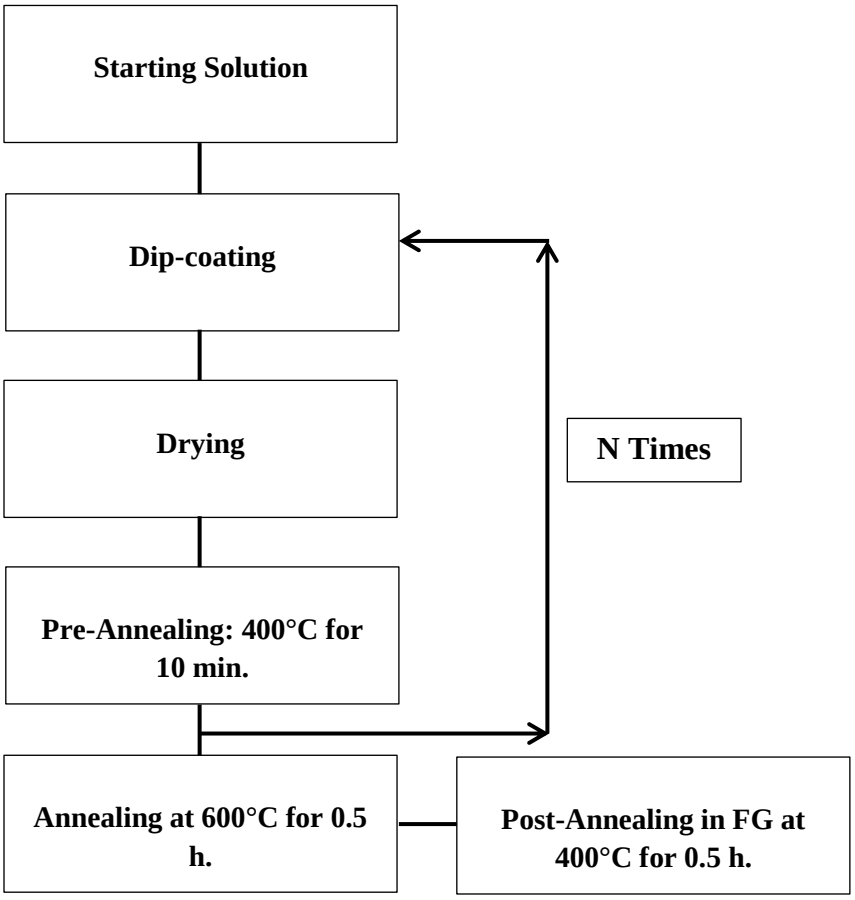

Figure 2.8: Scheme of Sol-Gel procedure for ZnO multi-layer**.**

Table 2.6 presents the number of layers and starting solutions used for the deposition of the multi layered ZnO films.

Table 2.6: Number of layers of studied films.

Number of layers	2	4	6	8	10
Stock Solutions	**Films**				
S5	F27	F28	F29	F30	F31
S7,S7b	F32	F33	F34,F34b	F35,F35b	F36,F36b
S8/S8d	-	-	-	F37/F37d	-
S17	F39	F40	F41	F42	F43

References

[1] D. Richard, Photon International, pp. 142–153 (March 2010).

[2] H. J. Gläser, Large area glass coating, Von Ardenne Anlagentechnik GmbH (Ed.): Dresden, Germany (2005).

[3] S. Faÿ U. Kroll, C. Bucher, E. Vallat-Sauvain, A. Shah, Sol. Energy Mater. Sol. Cells, 86, pp. 385-397 (2005).

[4] C. J. Brinker, S. W. Scherer, Sol-Gel science: the physics and chemistry of Sol-Gel processing, Academic Press: New York, (1990).

[5] C.J. Brinker, B.C. Bunker, D. R. Tallant, K. J. Ward and R. J. Kirkpatrick, Am. Chem. Soc., 26, pp. 314-332 (1988).

[6] H. Dislich and P. Hinz, J. Non-Cryst. Solids, 48, pp. 11-16 (1982).

[7] L.C. Klein and G.J. Garvey, Mater. Res. Soc. Sym. Proc., 32, pp. 33-36 (1984).

[8] K. D. Keefer, Mater. Res. Soc. Symp. Proc., 32, pp. 15-24 (1984).

[9] L.D. Landau and B.G. Levich, Acta Physiochim., U.R.S.S., 17, pp. 42-45 (1942).

[10] I. Strawbridge and P.F. Iames, J. Non-Cryst. Solids, 82, pp. 366-372 (1986).

[11] C.J. Brinker, A.J. Hurd and K.J. Ward, Ultrastructure Processing of Advanced Ceramics, eds. J.D. Mackenzie and D.R. Ulrich, Wiley: New York, (1988).

[12] O. Stern, Z. Elektrochem. Angew. Phys. Chem., 58, pp. 508-516 (1954).

[13] K. Ellmer, A. Klein and B. Rech, Eds. Transparent Conductive Zinc Oxide; Springer Series in Materials Science; Springer-Verlag: Berlin, 2008; Vol. 104.

[14] C. Jagadish and S. J. Pearton, Eds, Zinc Oxide: Bulk, Thin Films and Nanostructures; Elsevier: Oxford, U.K., 2006.

[15] A. Moezzi, M. Cortie and A. McDonagh, Dalton Trans., 40, pp. 4871-4878, (2011).

[16] L. Spanhel, J. Sol-Gel Sci. Technol., 39, pp. 7-24, (2006).

[17] L. Znaidi, Mater. Sci. Eng.B, 174, pp. 18-30, (2010).

[18] L. Spanhel and M. A. Anderson, J. Am. Chem. Soc., 113, pp. 2826-2833, (1991).

[19] M. Ohyama, H. Kozuka, T. Yoko and S. Sakka, J. Ceram. Soc. Jpn, 104, pp. 296-300, (1996).

[20] M. Ohyama, H. Kozuka and T. Yoko, Thin Solid Films, 306, pp.78-85, (1997).

[21] L. Znaidi, G. J. A. A. Soler Illia, R. Le Guennic, C. Sanchez and A. Kanaev, J. Sol-Gel Sci. Technol., 26, pp. 817-821, (2003).

[22] L. Znaidi, G. J. A. A. SolerIllia, S. Benyahia, C. Sanchez and A. Kanaev, Thin Solid Films, 428, 257-262, (2003).

[23] Y.S. Kim, W.P. Tai and S.J. Shu, Thin Solid Films, 491, pp. 153-160, (2005).

[24] S. O'Brien, L.H.K. Koh and G. M. Crean, Thin Solid Films, 516, pp. 1391-1395, (2008).

[25] M. Çopuroğlu, L.H.K. Koh, S. O'Brien and G.M. Crean, J. Sol-Gel Sci. Technol., 52, pp. 432-438, (2009).

[26] S. O'Brien, M. G. Nolan, M. Çopuroğlu, J. A. Hamilton, I.Povey, L. Pereira, R. Martins, E. Fortunato and M. Pemble, Thin Solid Films, 518, pp. 4515-4519, (2010).

[27] M. Dutta, S. Mridha and D. Basak, Appl. Surf. Sci., 254, pp. 2743-2747, (2008).

[28] C.-Y. Tsay, K.-S. Fan, S.-H. Chen and C.-H. Tsai, J. Alloys Compd., 495, pp. 126-130, (2010).

[29] L. D. Landau and B. G. Levich, Acta Physiochim, U.R.S.S., 17, pp. 42-46, (1942).

[30] E. A. Meulenkamp, J. Phys. Chem. B, 102, pp. 7764-7769, (1998).

[31] S. Rani, P. Suri, P.K. Shishodi and R.M. Mehra, Sol. Energ. Mat. Sol. Cells, 92, pp. 1639-1645, (2008).

[32] S. Ilican, F. Yakuphanoglu, M. Caglar and Y. Caglar, J. Alloys Compd., 509, pp. 5290-5294 (2011).

CHAPTER 3

Characterisation Techniques

In this chapter, both standard and innovative characterisation techniques used to study TCO thin films properties are described.

As listed in the first chapter and reported in [1], TCO films have to satisfy some requirements in order to be used in PV applications.

The film uniformity, homogeneity and the surface morphology may be observed by Atomic Force Microscopy (AFM), as well as by Scanning Electron Microscopy (SEM) analysis.

The amorphous nature of the dried films as well as the crystalline nature of the annealed films is ascertained by X-ray diffraction in grazing incidence configuration. The films thickness is measured by profilometric analysis and confirmed by SEM technique. The optical properties were studied by a double-beam Perkin Elmer Lambda 900 spectrometer equipped with a 10 *cm* diameter integrating sphere. Finally the electrical conductivity is measured by four-probe measurement technique.

Moreover, as discussed in the first chapter, one important parameter qualifying the TCO/hydrogenated amorphous Silicon (a-Si:H) interface is the density of states (D_{it}). In particular, it strongly affects the carriers lifetime in the region near the TCO/a-Si:H interface. The knowledge of this lifetime is fundamental in order to understand the effectiveness of TCO film use in PV applications. While D_{it} can be easily extracted from static capacitance-voltage (C–V) curves [2], no straightforward methods exist for extracting carriers lifetime.

Therefore, in the last part of this chapter, an innovative procedure developed during this PhD research to characterise TCO/a-Si:H interface is presented.

1. Standard Characterisation Techniques

1.1. XRD Analysis of Thin Film Materials

X-ray diffraction measurements of "thin" (1-1000 *nm*) films using conventional θ/2θ scanning methods generally produces a weak signal from the film and an intense signal from the substrate. One way to avoid intense signal from the substrate and get stronger signal from the film itself is to perform a diffraction technique that enhances the diffracted signal coming from the thin film. It is used to refer to it as grazing incidence X-ray diffraction (GIXRD) [3, 4].

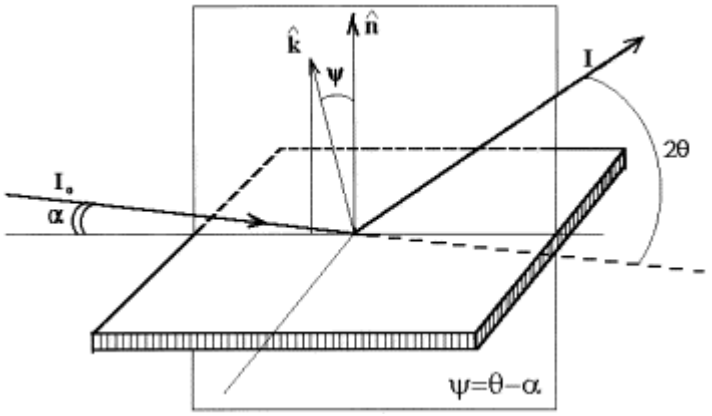

Figure 3.1: Experimental set-up for the GIXRD technique. The angle between the incident beam I_0 and the surface is given by α. I is the diffracted beam, θ is the Bragg angle and ψ is the angle between the surface normal **n** and the diffraction vector **k** normal to the diffracting planes.

In a GIXRD measurement the angle of incidence of the X-rays with respect to the sample surface is fixed at a low value. This value has to be higher than the critical angle of total external reflection to insure penetration of the X-rays into the thin film. GIXRD measurements are performed in a parallel beam geometry, which makes it non-sensitive to sample height displacement.

The advantages of GIXRD are:

- To confine most of (or all of) the incident X-ray beam within the thin film, since the penetration depth is significantly reduced due to the low angle of incidence of the X-rays;
- To reduce the intensity of the diffracted signal from the substrate. In case of single crystal substrate, it can even be completely suppressed;
- To control the depth of information by changing the angle of incidence of the X-rays;

Thin film phase identification is applied to characterise randomly oriented and weakly textured polycrystalline thin films.

In this research, the crystalline nature of all analysed films have been ascertained by X-ray diffraction using a Philips X'Pert PRO MRD diffractometer working with CuKa radiation (λ = 0.154056 *nm*). The glancing incidence configuration was used to obtain higher sensitivity to the film structure. GIXRD measurements were collected at a fixed incidence angle (during the measurements) in the range 0.3°-1.5°. The mean ZnO particle sizes were determined from the line broadening of the (101) diffraction plane using the Scherrer equation [5]. In Table 3.1, all analysed films are listed, for detail see Table 2.5 and Table 2.6.

Table 3.1: Analysed films by GIXRD technique.

Films	**F0-F6**	**F7-F14**	**F30, F42**	**F31, F43**	**F35, F35b**	**F37, F37b, F37c**
N° of layers	1	1	8	10	8	8
Incident Angle (°)	1.5	1.5	0.7	0.7	0.3	0.3

1.2. Atomic Force Microscopy (AFM) Analysis of Thin Film Materials

AFM, also called Scanning Force Microscopy (SFM), is a very high-resolution type of scanning probe microscopy with demonstrated resolution on the order of fractions of a nanometre, more than 1000 times better

than the optical diffraction limit. The precursor of the AFM, the Scanning Tunneling Microscope (STM), was developed by Gerd Binnig and Heinrich Rohrer in the early 1980s at IBM Research – Zurich. They were awarded with the Nobel Prize for Physics in 1986 thanks to the results of their researches. In the same year, Binnig, Quate and Gerber invented the first atomic force microscope which was first placed on the market in 1989. The AFM is one of the foremost tools for imaging, measuring and manipulating matter at the nanoscale. The information is gathered by "feeling" the surface with a mechanical probe. Piezoelectric elements facilitating tiny, accurate and precise movements on (electronic) command enable a very precise scanning. In some variations, electric potentials can also be scanned using conducting cantilevers. In more advanced versions, currents can be passed through the tip to probe the electrical conductivity of the underlying surface. Nevertheless, this is much more challenging with few research groups reporting consistent data.

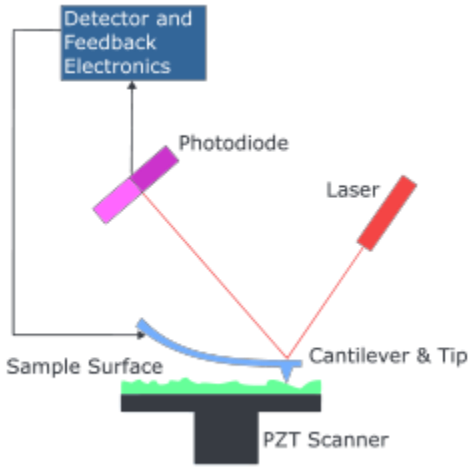

Figure 3.2: Block diagram of atomic force microscope.

The AFM consists of a cantilever with a sharp tip at its end used to scan the specimen surface. The cantilever is usually made by silicon or silicon nitride with a tip radius of curvature on the order of nanometres. When the tip is brought into proximity of a sample surface forces between the tip and the sample lead to a deflection of the cantilever, as per Hooke's law. Depending on the situation, forces that are measured in AFM include mechanical contact force, van der Waals forces, capillary forces, chemical bonding, electrostatic forces, magnetic forces (see Magnetic Force Microscope, MFM), Casimir forces, solvation forces, etc. Along with

force, additional quantities may simultaneously be measured through the use of specialised types of probe (see scanning thermal microscopy, scanning joule expansion microscopy, photothermal microspectroscopy, etc.). Typically, the deflection is measured using a laser spot reflected from the top surface of the cantilever into an array of photodiodes. Other methods used include optical interferometry, capacitive sensing or piezoresistive AFM cantilevers. These cantilevers are fabricated with piezoresistive elements acting as a strain gauge. Strain in the AFM cantilever can be measured by using the Wheatstone bridge. Nevertheless, this method is not as sensitive as laser deflection or interferometry.

The AFM can be operated in a number of modes depending on the application. In general, possible imaging modes are divided into static (also called “contact”) modes and a variety of dynamic (non-contact or "tapping") modes where the cantilever is vibrated.

In static mode, the cantilever is "dragged" across the surface of the sample and the contours of the surface are measured directly using the deflection of the cantilever. In the dynamic mode, the cantilever is oscillated externally at (or close to) its fundamental resonance frequency. The oscillation amplitude, phase and resonance frequency are modified by tip-sample interaction forces. These changes in oscillation with respect to the external reference oscillation provide information about the sample's characteristics.

In this research, the surface morphology of ZnO films was observed by a Veeco NanoScope IV Atomic Force Microscope operating in tapping mode (dynamic configuration).

In tapping mode (also called "AC Mode" or "intermittent contact mode") the cantilever is driven to constantly oscillate vertically closed to its resonance frequency by a small piezoelectric element mounted in the AFM tip holder similar to non-contact mode. However, the amplitude of this oscillation is greater than 10 *nm*, usually between 100 *nm* and 200 *nm*. When the tip comes close to the surface, Van der Waals force, dipole-dipole interaction, electrostatic forces, etc., cause the amplitude of this oscillation to decrease as the tip gets closer to the sample.. An electronic servo uses the piezoelectric actuator to control the height of the cantilever above the sample. The servo adjusts the height to maintain a set cantilever oscillation amplitude as the cantilever is scanned over the sample. A tapping AFM image is therefore produced by imaging the force of the intermittent contacts of the tip with the sample surface [6].

This method of "tapping" lessens the damage done to the surface and the tip compared to the amount done in contact mode. Tapping mode is gentle enough even for the visualisation of supported lipid bilayers or adsorbed single polymer molecules (for instance, 0.4 *nm* thick chains of synthetic polyelectrolytes) under liquid medium. With proper scanning parameters, the conformation of single molecules can remain unchanged for hours [7].

The analysed ZnO films by AFM are reported in Table 3.2.

Table 3.2: Analysed films by AFM technique.

Films	**F1-F6**	**F25**	**F30, F42**	**F31, F43**
N° of layers	1	1	8	10

1.3. SEM Analysis of Thin Film Materials

A Scanning Electron Microscope (SEM) is a type of electron microscope producing images of a sample by scanning it with a focused beam of electrons. The electrons interact with electrons in the sample, producing various signals that can be detected and that contain information about the sample's surface topography and composition. The electron beam is generally scanned in a raster scan pattern and the beam's position is combined with the detected signal to produce an image. SEM can achieve resolution better than 1 nanometre. Specimens can be observed in high vacuum, low vacuum and in wet condition (in environmental SEM).

Accelerated electrons in an SEM carry significant amounts of kinetic energy and this energy is dissipated as a variety of signals produced by electron-sample interactions when the incident electrons are decelerated in the solid sample. These signals include secondary electrons (producing SEM images), backscattered electrons (BSE), diffracted backscattered electrons (EBSD) used to determine crystal structures and orientations of minerals, photons (characteristic X-rays used for elemental analysis and continuum X-rays),

visible light (cathodoluminescence-CL) and heat. Secondary electrons and backscattered electrons are commonly used for imaging samples. Secondary electrons are most valuable for showing morphology and topography on samples and backscattered electrons are most valuable for illustrating contrasts in composition in multiphase samples (i.e. for rapid phase discrimination). X-ray generation is produced by inelastic collisions of the incident electrons with electrons in discrete orbitals (shells) of atoms in the sample. As the excited electrons return to lower energy states they yield X-rays with a fixed wavelength (this is related to the difference in energy levels of electrons in different shells for a given element). Thus, characteristic X-rays are produced for each element in a mineral "excited" by the electron beam. SEM analysis is considered to be "non-destructive". X-rays generated by electron interactions do not lead to volume loss of the sample. It is therefore possible to analyse the same materials repeatedly.

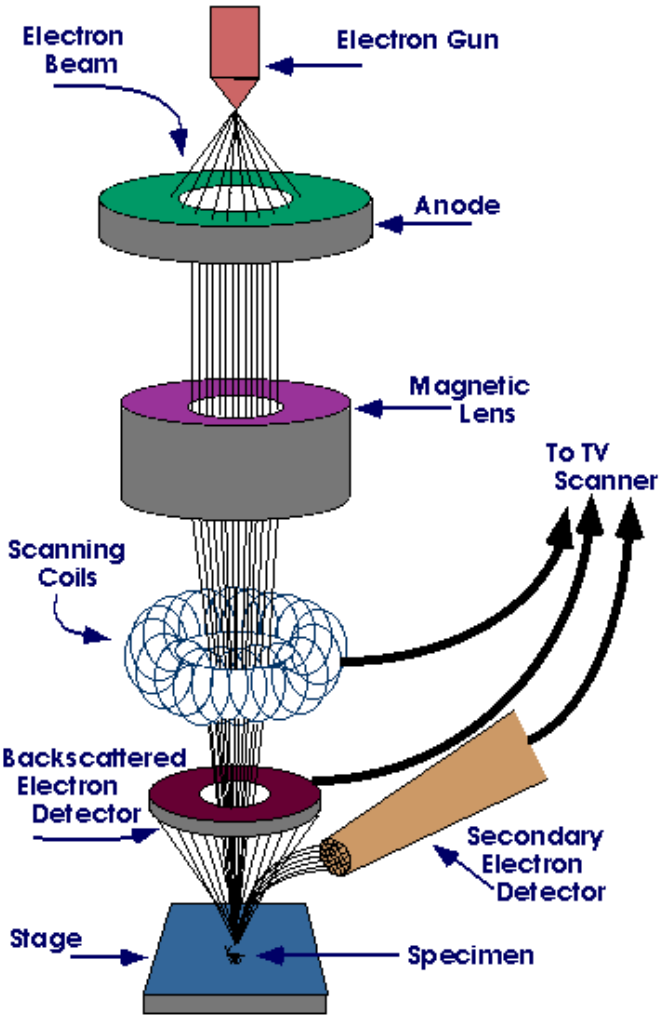

Figure 3.3: Schematic representation of a SEM.

Essential components of all SEMs include the following:

1. Electron Source ("Gun")
2. Electron Lenses
3. Sample Stage
4. Detectors for all signals of interest
5. Display / Data output devices
6. Infrastructure Requirements:
    - Power Supply

- Vacuum System
- Cooling system
- Vibration-free floor
- Room free of ambient magnetic and electric fields

SEMs have always at least one detector (usually a secondary electron detector) and most of them have additional detectors. The specific capacity of a particular instrument critically depends on its detectors.

In this PhD research activity, the SEM analysis was performed by means of a FEI Quanta 200 FEG (Eindhoven, The Netherlands) equipped with a secondary electron detector. SEM micrographs were collected operating in high vacuum mode and using an acceleration voltage of 20 *kV*. Before the analysis, samples were placed on SEM stubs through double sided adhesive conductive carbon discs and afterwards coated with a 15-20 *nm* thick Au-Pd layer by means of a Baltec-Leica Med 020 sputter coater equipment (Vienna, Austria).

In particular, top views and cross-sections of ZnO thin films were observed. All analysed films are listed in Table 3.3.

Table 3.3: Analysed films by SEM technique.

Films	**F5**	**F27, F32, F39**	**F28, F33, F40**	**F29, F34, F34b, F41**	**F30, F35, F35b, F37, F37d, F38, F38b, F42**	**F31, F36, F36b, F43**
N° of layers	1	2	4	6	8	10
Top View	x	x	x	x	x	x
Cross Section	x	x	x	x	x	x

1.4. Optical Characterisation of ZnO Thin Film Materials

TCO optical properties are very important for its use in PV applications. Reflection, transmittance and absorbance have to be measured.

Reflection is the process by which electromagnetic radiation is returned either at the boundary between two media (surface reflection) or at the interior of a medium (volume reflection), whereas transmission is the passage of electromagnetic radiation through a medium. Both processes can be accompanied by diffusion (also called scattering), the process of deflecting a unidirectional beam into many directions. In this case, it deals with diffuse reflection and diffuse transmission. When no diffusion occurs, reflection or transmission of a unidirectional beam results in a unidirectional beam according to the laws of geometrical optics. In this case, regular reflection (or specular reflection) and regular transmission (or direct transmission) take place. Reflection, transmission and scattering leave the frequency of the radiation unchanged. Exception: the Doppler Effect causes a change in frequency when the reflecting material or surface is in motion.

Absorption is the transformation of radiant power to another type of energy (usually heat) by interaction with material.

In general, reflection, transmission and absorption depend on the wavelength of the affected radiation. Thus, these three processes can either be quantified for monochromatic radiation (in this case, the adjective "spectral" is added to the respective quantity) or for a certain kind of polychromatic radiation. For the latter, the spectral distribution of the incident radiation has to be specified. In addition, reflectance, transmittance and absorbance might also depend on polarization and geometric distribution of the incident radiation, which therefore also have to be specified.

Total reflectance is further subdivided in regular reflectance (R_r) and diffuse reflectance (R_d), which are given by the ratios of regularly (or specularly) reflected radiant power and diffusely reflected radiant power to incident radiant power. From this definition, it is obvious that:

$$R = R_r + R_d \qquad (3.1)$$

The transmittance (*T*) of a medium is defined by the ratio of transmitted radiant power to incident radiant power. Total transmittance is further subdivided in regular transmittance T_r and diffuse transmittance T_d, which are given by the ratios of regularly (or directly) transmitted radiant power and diffusely transmitted radiant power to incident radiant power. Again:

$$T = T_r + T_d \qquad (3.2)$$

Finally, the absorbance (*A*) of a medium is defined by the ratio of absorbed radiant power to incident radiant power.

Being defined as ratios of radiant power values, reflectance, transmittance and absorbance are dimensionless.

Quantities such as reflectance and transmittance are used to describe the optical properties of materials. They are dependent on many parameters such as:

- Thickness of the sample;
- Surface conditions;
- Angle of incidence;
- Temperature;
- The spectral composition of the radiation;
- Polarisation effects.

The measurement of optical properties of materials using integrating spheres is described in DIN 5036-3 and CIE 130-1998.

It is to be noted that a total transmittance higher than 80-85% (average value) in the visible region of solar spectrum is required. Moreover, the diffuse transmittance is an important parameter that should be monitored. Values higher than 25-30% (average value) are required to increase the optical pathway of incident light inside the solar cell active layers.

In this PhD research activity, optical transmittance and reflectance in the UV–vis-NIR region were measured by a double-beam Perkin Elmer Lambda 900 spectrometer equipped with a 10 *cm* diameter integrating sphere. The optical bandgap was evaluated according to the following equation [8]:

$$(\alpha h\nu) = A(h\nu - E_g)^{1/2} \qquad (3.3)$$

Where A is a constant having values between $1x10^5$ and $1x10^6$ cm^{-1} eV^{-1} [9] and E_g is the optical bandgap. The absorption coefficient is directly related to the transmittance (*T*) and film thickness (*t*) by the formula:

$$T = Be^{-\alpha t} \qquad (3.4)$$

where the constant B is approximately 1, for ZnO materials.

In this research, optical properties of all prepared ZnO films are been measured. Expermental results are reported in the next chapter.

1.5. Electrical Characterisation of ZnO Thin Film Materials

Electrical characterisation can be used to determine resistivity, carrier concentration, mobility, contact resistance, barrier height, depletion width, oxide charge, interface states, carrier lifetimes, and deep level impurities.

In this research activity, the electrical resistivity, the interface states and the carrier lifetimes were evaluated. In particular, the electrical resistivity has been evaluated by means of four-point probe measurements.

By applying this method the sheet resistance (R_s) may be measured. It is the ratio between the resistivity and the film thickness.

As Figure 1.a. shows, several resistances need to be considered while performing a resistance measurement. The probe has a probe resistance (R_p). It can be determined by shorting two probes and measuring their resistances. At the interface between the probe tip and the semiconductor, there is a probe contact resistance (R_{cp}). A spreading resistance (R_{sp}) can be observed while the current flows from the small tip into the semiconductor. Finally the semiconductor itself has a sheet resistance.

Figure 1.c shows the equivalent circuit for the measurement of semiconductor sheet resistance by using the four-point probe. Two probes carry the current and the other two probes sense the voltage. Each probe has a probe resistance, a probe contact resistance and a spreading resistance associated with it. However, these parasitic resistances can be neglected for the two voltage probes as the voltage is measured with a high impedance voltmeter drawing few electric current. Thus, the voltage drops across these parasitic resistances are very small. The voltage reading from the voltmeter is approximately equal to the voltage drop across the semiconductor sheet resistance.

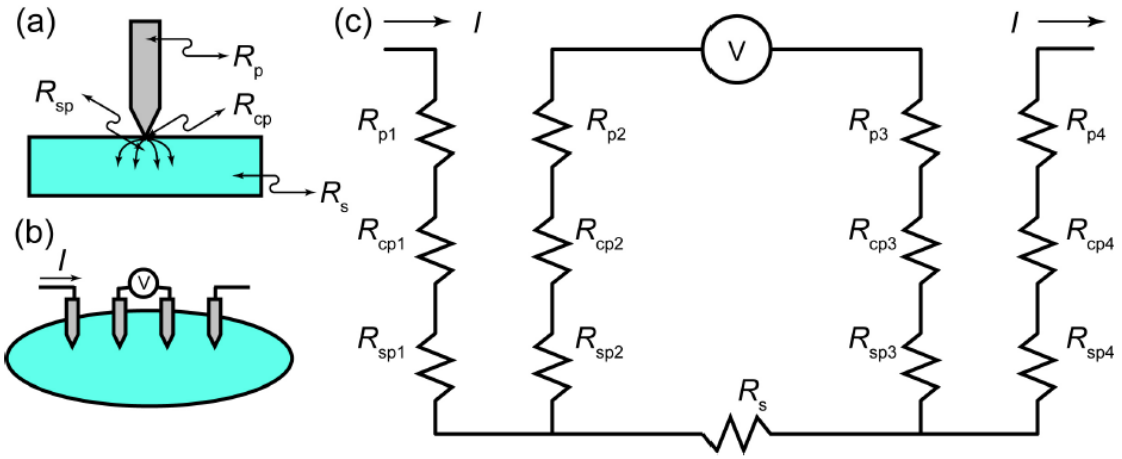

Figure 3.4: Four-point probe measurement of sheet resistance.

The semiconductor sheet resistance can be calculated by using the four-point probe method:

$$R_S = F \times \left(V / I \right) \qquad (3.5)$$

Where V is the voltage reading from the voltmeter, I is the current carried by the two current probes, and F is a correction factor. For collinear or in-line probes with equal probe spacing, the correction factor F can be written as a product of three separate correction factors:

$$F = F1 \cdot F2 \cdot F3 \qquad (3.6)$$

F1 corrects for finite sample thickness, F2 corrects for finite lateral sample dimensions and F3 corrects for placement of the probes with finite distances from the sample edges. For very thin samples with the probes

being far from the sample edge, F2 and F3 are approximately equal to one (1.0), and the expression of the semiconductor sheet resistance becomes:

$$R_S = \left(\frac{\pi}{\ln 2}\right) \times \left(\frac{V}{I}\right) \qquad (3.7)$$

The four-point probe method can eliminate the effect introduced by the probe resistance, probe contact resistance and spreading resistance [2]. Therefore, it has more accuracy than the two point probe method.

In this PhD research activity, the electrical resistivity of all deposited films was measured.

1.6. Capacitance-Voltage Characterisation of ZnO/Active Layer Interface

Capacitance-voltage (C-V) measurements are commonly used in studying oxide-semiconductor interface quality in detail. These measurements are made on a two-terminal device called Metal-Oxide-Semiconductor (MOS) capacitor, Figure 3.5.

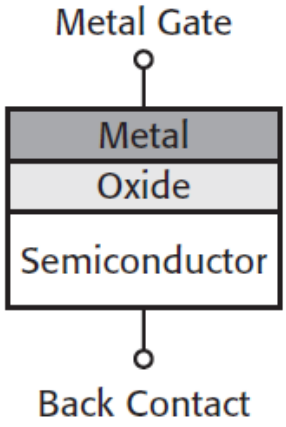

Figure 3.5: MOS Capacitor.

In this PhD research activity, the MOS structure was fabricated by depositing p-type a-Si:H on gel derived ZnO thin film. The p-type a-Si:H (0.5 μm thick) layer was deposited by VHF-PECVD at ENEA Portici

labs. Its characteristics are the same of the front p-layer used in thin film solar cells [10]. The gel-derived ZnO thin film is deposited on glass substrates by Sol-Gel method starting from S5 solution (see Table 2.1).

Figure 3.5 illustrates the construction of a MOS capacitor. Essentially, the MOS capacitor is an oxide placed between a semiconductor and a metal gate. The semiconductor and the metal gate are the two plates of the capacitor. The oxide layer is the dielectric. The area of the metal gate defines the area of the capacitor. The most important property of the MOS capacitor is that its capacitance changes with an applied DC voltage. As a result, the modes of operation of the MOS capacitor change as a function of the applied voltage [2]. The simplified equivalent circuit of a MOS structure is reported in Figure 3.6 [11].

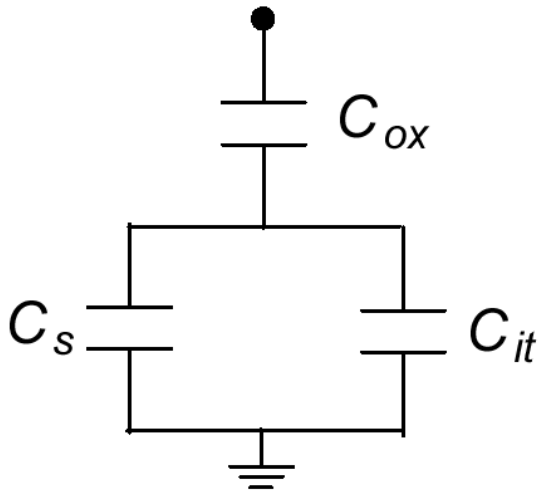

Figure 3.6: Simplified equivalent circuit of a MOS capacitor.

Where C_S is the space charge region capacitance, C_{it} the interface trapped charge capacitance and C_{ox} the gate oxide capacitance. The capacitance C_S depends on the voltage applied to the gate. There are three regimes of operation which can be described by what occurs to the semiconductor surface:

Accumulation: in which mobile carriers of the same type as the semiconductor (substrate) accumulates at the surface – in this condition the total capacitance is equal to C_{ox} [2].

Depletion: in which the surface is devoid of any mobile carriers leaving only a charge space or depletion layer – in this case the total capacitance is the series of C_{ox} with the parallel of C_s and C_{it};

Inversion: with increasingly applying positive voltage, the surface depletion region will continue to widen until the onset of surface inversion conductivity is observed. An inversion layer is formed. This layer is very thin and separated from the bulk of silicon by the depletion layer [2]. As the charge density in the inversion layer may or may not be able to follow the ac variation of the applied gate voltage, it has to be intended that the capacitance under inversion conditions will be a function of frequency. In particular, the capacitance of the structure, in inversion regime at low frequency (typically less than 10 *Hz*) is equivalent to the one of the oxide layer, rights as in the accumulation mode. Instead, the increase of charge in the metal side at higher frequency (typically higher than 10^4 *Hz*) is balanced by the substrate charge as the minority carriers can no longer adjust their concentrations. Therefore the high frequency (HF) capacitance of the MOS structure (C_{HF}), is given by:

$$\frac{1}{C_{HF}} = \frac{1}{C_{OX}} + \frac{1}{C_{S\lim}} \qquad (3.8)$$

where C_{Slim} is given by:

$$C_{S\lim} = \frac{\varepsilon_0 \varepsilon_S}{W_S} \qquad (3.9)$$

In equation 3.9, W_S represents the width of depletion region and it is given by the formula:

$$W_S = \sqrt{\frac{4\varepsilon_0 \varepsilon_S kT \ln(\frac{N_A}{n_i})}{q^2 N_A}} \qquad (3.10)$$

Moreover, it has to be noted that C_{it} ($C_{it}=q^2 \cdot D_{it}$) depends on the working frequency. At sufficiently high frequencies the trapping phenomena do not follow the signal [2, 11]. Therefore, high frequency curve is not affected by D_{it}. Instead, low frequency (LF) capacitance is affected by D_{it} and in depletion/inversion regime it becomes:

$$\frac{1}{C_{LF}} = \frac{1}{C_{OX}} + \frac{1}{C_{S\lim} + C_{it}} \qquad (3.11)$$

the D_{it} distribution can be evaluated from equation 3.11 (by applying the C_{it} definition):

$$D_{it} = \frac{1}{q^2}\left(\frac{C_{OX}C_{LF}}{C_{OX} - C_{LF}} - C_{S\lim}\right) \qquad (3.12)$$

the capacitance C_{Slim} can be measured from HF C-V curve [2]. Equation 3.12 becomes:

$$D_{it} = \frac{1}{q^2}\left(\frac{C_{OX}C_{LF}}{C_{OX} - C_{LF}} - \frac{C_{OX}C_{HF}}{C_{OX} - C_{HF}}\right) \qquad (3.13)$$

In this activity, C-V curves have been measured by a Solartron 1260 Impedance Gain-Phase Analyser at a frequency of 1 *MHz*, for HF C-V and 1 *Hz* for LF C-V.

The D_{it} extraction method has been applied on MOS structures fabricated on F37d and F42 gel derived ZnO films.

2. Innovative Characterisation Technique

As previously discussed, measurement techniques based on MOS capacitance operation are the most widely accepted characterisation tools for investigating interface and near-interface properties of semiconductors.

Many approaches have been proposed for the modelling of Oxide-Semiconductor interface physics: full analytical models [12], transmission lines method [13], equivalent circuit models [14-16]. Among others, equivalent circuits have the advantage of providing an immediate and intuitive understanding of individual phenomena taking place in the MOS structure.

In particular, in the inversion regime the behaviour of the MOS structure can be represented by the equivalent circuit shown in Figure 3.7, where C_S, C_{it} and C_{ox} have the same meaning as previously discussed, R_{it} describes losses due to recombination/generation through interface states and G_N is the conductance related to thermal generation supplying electrons to the inversion layer.

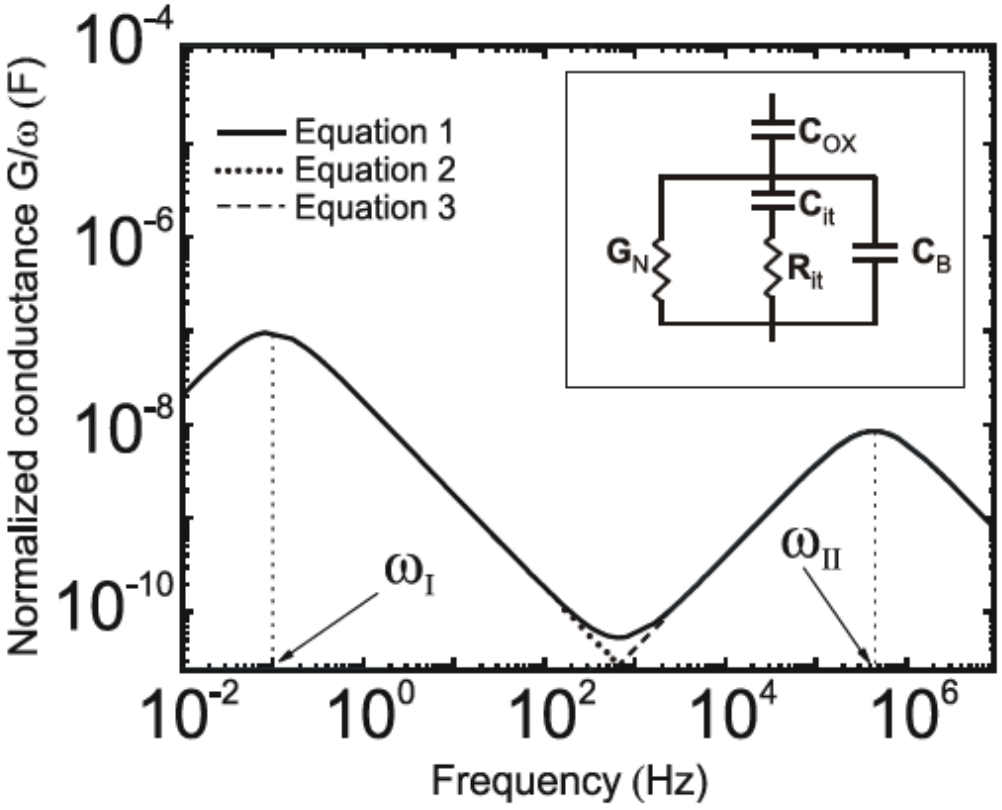

Figure 3.7: Equivalent MOS circuit (inset) and corresponding normalised conductance G/ω (full line). The dotted and dashed lines are respectively, the simplified forms of equation 3.14 given by 3.15 and 3.16. The following values were used for the parameters: $C_{ox}= 2.2\cdot10^{-7}$ *F*, $C_{it}= 2.1\cdot10^{-8}$ *F*, $C_S= 1.4\cdot10^{-8}$ *F*, $G_N= 2.9\cdot10^{-9}$ *S* and $R_{it}= 10^2$ *Ω*.

Among circuit parameters the terms C_{ox}, C_B and C_{it} can be easily extracted from static C-V curves [2] (as discussed in the previous paragraph) while no straightforward methods exist for extracting G_N and R_{it}.

In this paragraph, a procedure to extract the above parameters from a single Conductance –frequency (G-ω) curve is shown. Closed form analytical expressions for both the conductive term G_N and the dissipative term R_{it} are given as a function of C_{ox}, C_B and C_{it}. The reliability of the procedure is expressed through experimental measurements and numerical analysis performed in the Synopsys-Sentaurus TCAD environment [17].

In this PhD research activity, G-ω curves were collected by the Solartron 1260 Impedance Gain-Phase Analyser. F37d as well as F42 gel-derived ZnO films were characterised.

2.1 Model Description

According to the equivalent circuit model in Figure 3.7 the analytical description of the overall conductance G, normalised to ω is expressed in the form given in equation 3.14, where $\tau_{it}=R_{it}\cdot C_{it}$. The plot of equation 3.14 is reported in Figure 3.7 as well. As can be noticed, it usually exhibits two clearly detectable maxima.

$$\frac{G}{\omega}=\frac{\frac{\omega\cdot C_{ox}}{G_N}\cdot\left(1+\frac{\omega^2\cdot C_{it}}{G_N}\tau_{it}+\left(\omega\tau_{it}\right)^2\right)}{1+\left(1+\left(\omega\tau_{it}\right)^2\right)\cdot\left(\frac{\omega\cdot C_{ox}}{G_N}+\frac{\omega\cdot C_B}{G_N}\right)^2+\frac{2\omega^2\cdot C_B\cdot C_{it}}{G_N^2}+\frac{2\omega^2\cdot C_{ox}\cdot C_{it}}{G_N^2}+\left(\frac{\omega\cdot C_{it}}{G_N}\right)^2+2\omega\tau_{it}\frac{\omega\cdot C_{it}}{G_N}+\left(\omega\tau_{it}\right)^2}\cdot C_{ox} \tag{3.14}$$

$$\frac{G}{\omega}=\frac{\omega\cdot C_{ox}G_N}{G_N^2+(\omega\cdot C_B+\omega\cdot C_{ox})+2\omega^2\cdot C_B\cdot C_{it}+2\omega^2\cdot C_{ox}\cdot C_{it}+\omega^2\cdot {C_{it}}^2}\cdot C_{ox} \tag{3.15}$$

$$\frac{G}{\omega}=\frac{\omega\cdot C_{it}\cdot\tau_{it}}{(1+\left(\omega\cdot\tau_{it}\right)^2)\cdot\left(C_B+C_{ox}\right)^2+2C_B\cdot C_{it}+2C_{ox}\cdot C_{it}+{C^2}_{it}}\cdot {C^2}_{ox} \tag{3.16}$$

When the abscissas of the maxima are sufficiently spaced (this point will be discuss shortly) the curve can be built as the superposition of the dotted plus the dashed lines (see Figure 3.7).

The dotted line corresponds to the equivalent circuit when R_{it} is short circuited. In this case the analytical expression of G/ω is given by equation 3.15. This equation can be analytically solved to find the abscissa of its maximum:

$$\omega_I=\frac{G_N}{C_{ox}+C_S+C_{it}} \tag{3.17}$$

so that G_N is expressed as:

$$G_N = \omega_I \cdot (C_{ox} + C_S + C_{it}) \qquad (3.18)$$

The value of G_N, allows the extraction of the recombination lifetime τ_r in the p-type substrate. As a matter of fact [11] it is possible to write:

$$G_N = K_1 + \frac{K_2}{\sqrt{D_N \cdot \tau_r}} \qquad (3.19)$$

with K_1 given by:

$$K_1 = \frac{2\varepsilon_r n_i}{N_A W \tau_g} \qquad (3.20)$$

and K_2 given by:

$$K_2 = \frac{q\mu_n {n_i}^2}{N_A} \qquad (3.21)$$

In these expressions q represents the electron charge, ε_r the silicon dielectric constant, W the extend of the space charge region, N_A the substrate doping, n_i is the semiconduor intrinsic carrier concentration and μ_n the electron mobility.

The dashed line in Figure 3.7 corresponds to the equivalent circuit when the branch including G_N is open. In this case the analytical expression of G/ω is given by equation 3.16. This equation can be analytical solved as well. The abscissa of the maximum is given by:

$$\omega_{II} = \frac{C_{ox} + C_S + C_{it}}{R_{it} \cdot C_{it} \cdot (C_{ox} + C_S)} \qquad (3.22)$$

and R_{it} can be expressed as:

$$R_{it} = \frac{C_{ox} + C_S + C_{it}}{\omega_{II} \cdot C_{it} \cdot (C_{ox} + C_S)} \qquad (3.23)$$

The above approach may be applied to G/ω curves that exhibit two clearly distinguishable maxima. In this case the two branches of the curve are almost independent of each other and the error made by using equation 3.17 and 3.22 is plainly negligible. The method should not be applied when the two branches cannot be unambiguously identified. However, it is easy to verify that in a wide range of meaningful values of the parameters, G/ω curves like the one represented in Figure 3.7 should be expected. From equation 3.17 and 3.22, we deduce that two separate maxima exist only if:

$$\frac{G_N}{C_{ox}+C_{it}+C_B} << \frac{C_{it}+C_{ox}+C_B}{R_{it}C_{it}\cdot(C_B+C_{ox})} \qquad (3.24)$$

Equation 3.24 *a fortiori* holds if:

$$G_N R_{it} << 1 \qquad (3.25)$$

The above relation is satisfied in almost all practical cases because typical values of G_N fall in the range 10^{-9}–10^{-6} S/cm^2 [2, 11], hence, only values of R_{it} greater than 10^6 $\Omega \cdot cm^2$ can affect equation 3.25. We evaluate that for such a large value the second maximum vanishes (the branch with R_{it} opens) and the curve would show only one maximum. Thus, if two maxima exist, their distance is greater than one order of magnitude.

2.2 Numerical Analysis

In order to verify the reliability of the proposed method an experiment by exploiting the numerical simulation environment Synopsys Sentaurus TCAD [17] has been made. The simulator has been used to model the behaviour of a MOS structure (ZnO on p-type Silicon): the used geometry and physical parameters are reported in Table 3.1.

To carry out the experiment, doping-dependent mobility degradation model [18], mobility degradation at interfaces [19], surface SRH recombination [17] and trap occupation dynamics model (V-model) [17] were used.

Figure 3.8 shows the G/ω curve achieved by the simulator. It is important to underline that this result is not trivial because the analytical model coming from the equivalent circuit has a totally different approach compared to numerical simulation directly solving fundamental semiconductor equations.

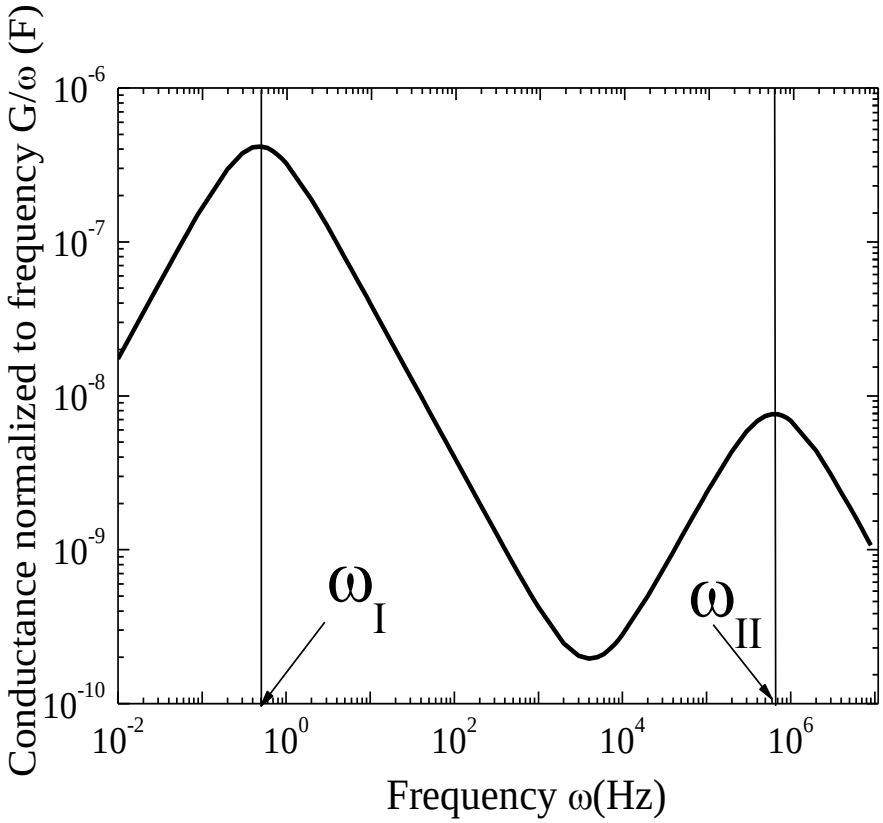

Figure 3.8: Conductance of the simulated MOS structure.

As it can be understood by Figure 3.8 $\omega_I = 5 \cdot 10^{-1} Hz$ and $\omega_{II} = 6.68 \cdot 10^5$ *Hz*. Equations 3.17 and 3.22 express that $G_N = 2.8 \cdot 10^{-7}$ *S* and $R_{it} = 100$ *Ω*. A recombination lifetime equal to 20 *μs* can be found by applying equation 3.18.

Therefore, the extract parameters (by applying the extraction method) are coincident with the input parameters in the simulator. This confirms the reliability of the used approach.

Table 3.4: Geometry and Physical parameters set in input in the simulator.

	Quantity	Value
t_{ox}	Oxide thickness	$1.55 \cdot 10^{-6}\, cm$
N_A	p-type substrate doping	$10^{15}\, cm^{-3}$
A	Area	$1\ cm^2$
D_{it}	Interface trap capacitance	$1.6 \cdot 10^{-8} F$
τ_g	Generation lifetime	$10\ \mu s$
τ_r	Recombination lifetime	$20\ \mu s$
R_{it}	Interface resistance	$100\ \Omega$

References

[1] M. W. Rowell and M. D. McGehee, *Energy Environ. Sci.*, 4, pp. 131-134 (2011).

[2] D. K. Schroder, Semiconductor Material and Device Characterisation, 3rd ed. New York: Wiley, pp. 319–387 (2005).

[3] M.F. Doerner and S. Brennan, J. Appl. Phys., 63 (1), pp. 128-136 (1988).

[4] H. Mohrbacher, K. Van Acker, B. Blanpain, P. Van Houtte and J.-P. Celis, J. Mater. Res., 11 (7), pp. 1776-1782 (1996).

[5] P. Debye and P. Scherrer, Physik. Z., 17, pp. 277–283 (1916).

[6] A. N. Geisse, Materials Today, 12 (7-8), pp. 40-45 (2009).

[7] Y. Roiter and S. Minko, J. Am. Chem. Soc., 127 (45), pp. 15688–15689 (2005).

[8] J. Tauc, R. Grigorovici and A. Vancu, Physica Status Solidi, 15, pp. 627-637 (1966).

[9] E.A. Davis and N.F. Moh, Philosophical Magazine, 22, pp. 903-922 (1970).

[10] P. Delli Veneri, P. Aliberti, L. V. Mercaldo, I. Usatii and C. Privato, Thin Solid Films, 516, pp. 6979-6983 (2008).

[11] D.K. Schroder, J.E. Park, S.E. Tan, B.D. Choi, S. Kishino and H. Yoshida, IEEE Trans. Electron. Dev., 47 (8), pp. 1653-1661 (2000).

[12] W. Shockley and W.T. Read, Phys. Rev., 87, pp. 835-842 (1952).

[13] G. Baccarani, C.A. Baffoni, M. Rudan and G. Spadini, Solid-State Electron., 18, pp. 1115-1122 (1975).

[14] K. Lehovec and A. Slobodskov, Solid-State Electron., 7, pp. 59-79, (1964).

[15] S. R. Hofstein and G. Warfield, Solid-State Electron., 8, pp. 321-341 (1965).

[16] C.T. Sah, Solid-State Electron., 13, pp. 1547-1575 (1970).

[17] Sentaurus Device User Guide Version Z-2007.03, March 2007, Synopsys.

[18] N. D. Arora, J. R. Hauser, and D. J. Roulston, IEEE Transactions on Electron Devices, 29 (2), pp. 292–295 (1982).

[19] C. Lombardi, IEEE Transactions on Computer-Aided Design, 7 (11), pp. 1164–1171 (1988).

CHAPTER 4

ZnO Films Characterisation

This chapter deals with the characterisation of gel derived ZnO thin films. It is divided into three sections. The first part will explain the structural, morphological, optical and electrical analysis of single layer ZnO films. Characterisation will be considered in order to found the optimal synthesis conditions for ZnO films deposition. The second section will analyse the standard characterisation of multi layer ZnO films, the effect of pH on the ZnO synthesis as well as those of Boron and Aluminium doping on thin films. Lastly, the third section, instead, will investigate the interface between some selected ZnO films and the a-Si:H (p-type) by following the developed G-ω method. Finally, single junction thin film solar cells (made by a-Si:H) deposited on ZnO films are presented and characterised.

1. ZnO thin films – Single layer

1.1 The effect of additives on film properties

From S1 and S2 solutions (see Table 2.1), by a single dipping step at room temperature amorphous thin films were achieved, as ascertained by XRD patterns. ZnO films (F1 and F2, see Table 2.5) were obtained by annealing in air at 600 °*C* for 2 *h* the dried films. Their GIXRD patterns are displayed in Figure 4.1.

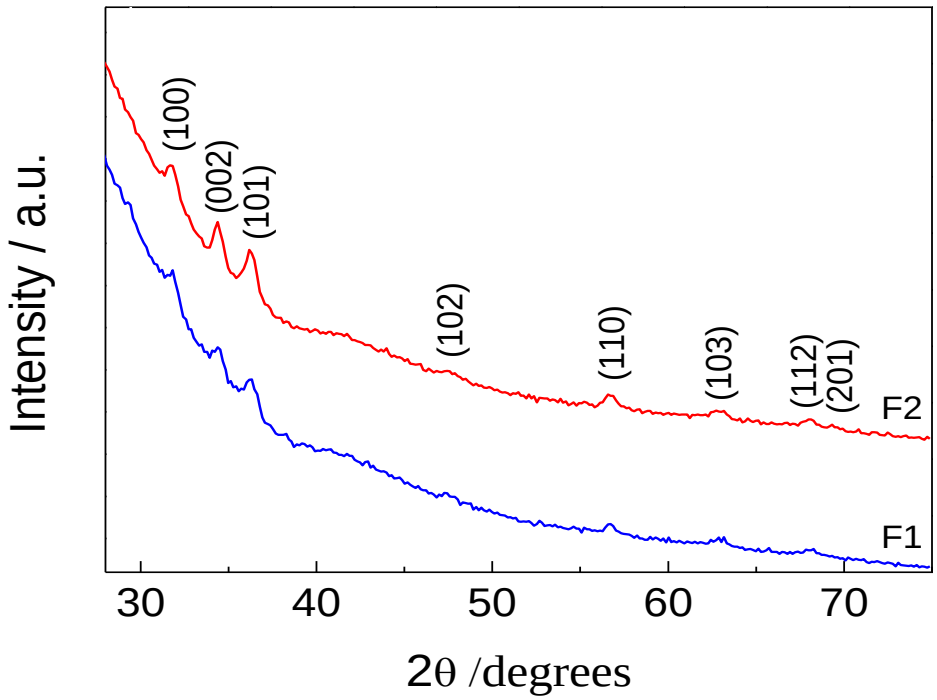

Figure 4.1: GIXRD patterns of films obtained starting from solutions containing HAc (F1) and TEA (F2) as additives and annealed in air at 600°C for 2 *h*. The Miller indices for the ZnO peaks are labelled.

All XRD peaks were indexed and found to be in agreement with those of the hexagonal wurtzite phase of ZnO (ICDD card No. 36-1451). ZnO nanocrystals appeared randomly oriented in both films. Moreover, from XRD peaks intensity, the crystallinity degree appeared higher in F2 than in F1 even if the average size of nanocrystals was very similar: 16 *nm* (F2), 12 *nm* (F1). This result confirmed the effect of pH on ZnO crystal grain size, as discussed in the second chapter and as reported in [3].

F1 and F2 showed different thickness: F2 (80 *nm*) was thicker than F1 (70 *nm*). This was mainly due to the different viscosities of starting solutions, being S2 more viscous than S1.

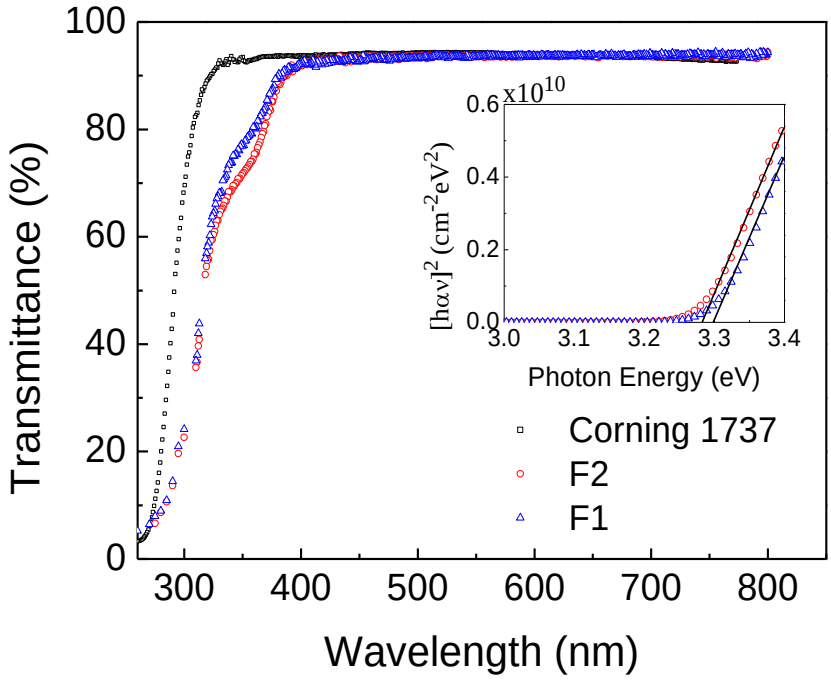

Figure 4.2: Optical transmittance spectra of films obtained starting from solutions containing HAc (F1) and TEA (F2) as additives and annealed in air at 600°C for 2 *h*. The spectrum of the glass substrate is also reported. The inset shows the plot of $(\alpha h\nu)^2$ versus photon energy.

Figure 4.2 displays the optical transmittance spectra of F1 and F2 in the UV–Vis range, together with the spectrum of the glass substrate. The optical transmission of films in the visible region was extremely high, comparable to that of the glass substrate. Both films exhibited, in the visible range, an average transmittance higher than 92%. The transmission decreased sharply near the ultraviolet region due to the band gap absorption of ZnO. It was expected that the optical transmittance of zinc oxide should vanish abruptly in the near-UV region. Instead, the spectra of F1 and F2 displayed an absorption tail at about 350 *nm*, as found for other ZnO gel derived films [4, 5], that could be due either to the low crystallinity and defects [6-8] or to the residual porosity [9] of the films.

E_g values were evaluated by extrapolating the linear absorption edge and its intercept with energy axis, as shown in the inset of Figure 4.2, obtaining about 3.30 *eV* for F1 and about 3.29 *eV* for F2 that are lower than the ZnO crystal bandgap (3.37 *eV*) because of their polycrystalline nature [10]. Finally, the electrical resistivity

of F1 and F2 was evaluated, from the current-voltage (I-V) curves (here not reported), giving $8 \cdot 10^3$ and $6 \cdot 10^3$ $\Omega \cdot cm$, respectively.

The above results with the high solubility of ZnO in HAc that hinders the possibility to obtain multilayer films indicate that TEA is a more suitable additive in this Sol–Gel route. In fact, it allows performing the whole synthesis procedure at room temperature obtaining ticker films with a lower resistivity.

1.2 The role of ZnO precursors solution concentration.

Stock solutions more concentrated than 0.50 M were prepared by using TEA as additive. By increasing the TEA amount, both the pH and the chemical stability of the solution rise (see Table 2.1). As expected, ticker ZnO films were obtained from these solutions (see Table 4.1). As a matter of fact, despite the withdrawal speed was the same, the film thickness was influenced both by the viscosity and by the density of the stock solution [11]. The solution viscosity was strongly influenced by the TEA amount. TEA molar ratio was kept constant at 1, the viscosity of the solution rose by increasing the ZAD concentration but, at the same time, the density of the solution increased as well. As a consequence, the ZnO film thickness changed from 80 (F2) to 125 *nm* (F6) altering the solution concentration from 0.50 M (S2) to 1.2 M (S6) (see Table 3.1). It should be noted that these values were referred to the thickness of a single layer.

Table 4.1: Thickness (*t*), average ZnO crystal size (*d*) and optical characteristics of films annealed in air at 600 °C for 2h. (*T*): transmittance; (*A*): absorbance; (*R*): reflectance; these are the average values in the range 400-800 *nm*. (*Eg*): optical bandgap.

Film	***t* (*nm*)**[a]	***d* (*nm*)**	***T* (%)**	***R* (%)**	***A* (%)**	E_g **(*eV*)**
F2	80	15	92.5	7.0	0.50	3.29
F3	90	16.5	92	7.1	0.90	3.29
F4	100	18	91.3	7.5	1.2	3.29
F5	120	22	90.2	8.4	1.4	3.28
F6	125	23	88.3	9.8	1.9	3.28

[a] This value is related to single layer

GIXRD patterns of F2–F6 ZnO films are displayed in Figure 4.3. All diffraction lines were indexed and found to be in agreement with those of the hexagonal wurtzite phase of ZnO. All films appeared polycrystalline and randomly oriented.

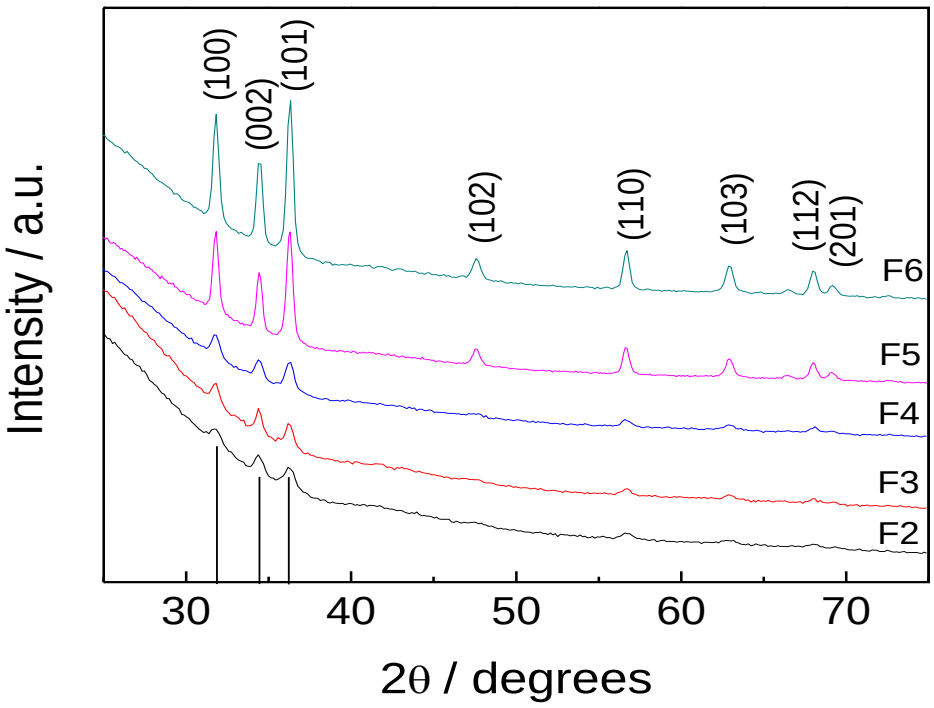

Figure 4.3: XRD patterns of films obtained from solutions with different ZAD molar concentration (F2-F6) and annealed in air at 600°C for 2 *h*. The Miller indices for the ZnO peaks are labelled.

As expected [4, 12-15], both the crystallinity degree and the average size of ZnO nanocrystals increased both with the concentration of stock solution (see Table 4.1) and with the solution pH [3]. The morphological analysis of the annealed films well agreed with these results. All films have appeared to be formed by rounded shape ZnO nanoparticles uniformly distributed on the film surface as shown in Figure 4.4, where AFM micrographs of F2 and F5 ZnO films are displayed. They were representative of ZnO films obtained from low and high stock solution concentration, respectively. It was possible to see that the mean size of ZnO grains was larger with respect to the values estimated by the Scherrer formula.

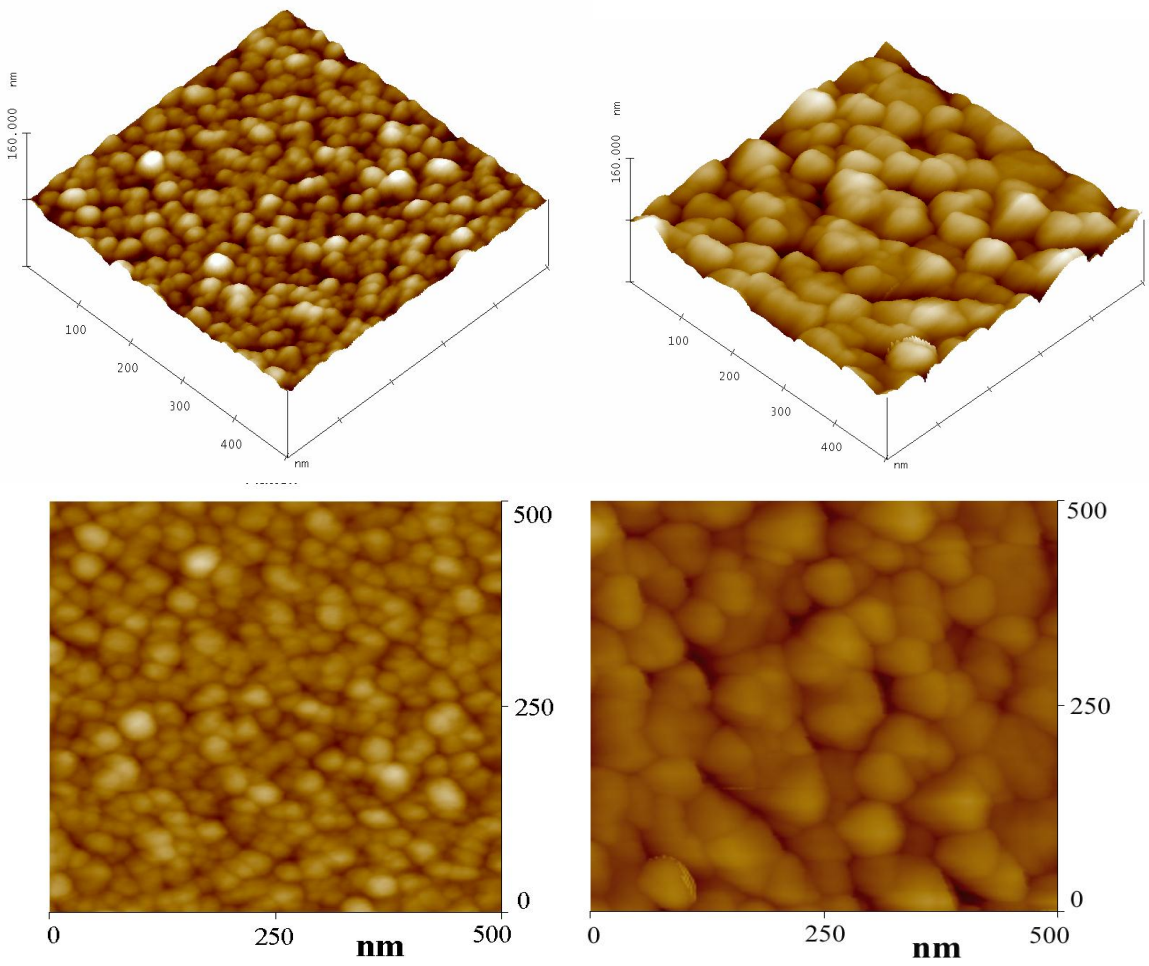

Figure 4.4: AFM micrographs of the films annealed in air at 600°C for 2 *h*. Left images: ZAD solution 0.5 M (F2); right images: ZAD solution 1 M (F5).

The discrepancy between the values measured by means of GIXRD and AFM images could be explained by two different hypotheses. According to the former, the crystallite size calculated with the Scherrer equation could be directly related to crystallographic coherent crystalline unit that diffracts the X-ray. This was the average value of all the film thickness, whereas the grain size calculated from the AFM images was related to the film surface as distance between two visible grain boundaries. According to the latter, the grain estimated by AFM image could be hypothesised as a crystallite rounded by an amorphous shell.

Finally, both films showed a low residual porosity. The Root Mean Square (RMS) values of the surface roughness were evaluated thanks to the images of F2-F6 films. They ranged from 6 *nm* for F2 to about 9 *nm* for F5 and F6 (as shown in Figure 4.5) showing an increasing trend with the film thickness and the grain size. This

trend is very interesting in view of thin film PV applications where high TCO texturing was required due to the light scattering ability.

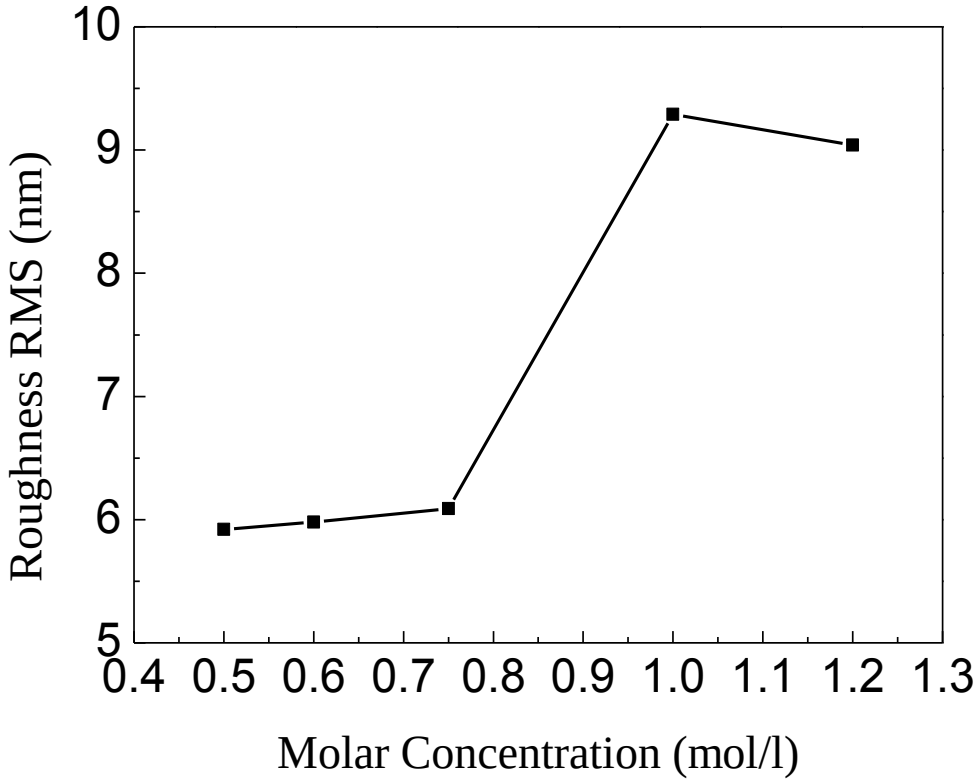

Figure 4.5: Root main square (RMS) of F2-F6 films surface roughness, evaluated by AFM images.

The SEM images of F5 film are shown in Figure 4.6. The cross-section image confirmed good film uniformity, granular nature and allowed us to estimate the film thickness that agrees with the value carried out by profilometric analysis (reported in Table 4.1). Moreover, the top image shows low residual porosity according to the AFM analysis.

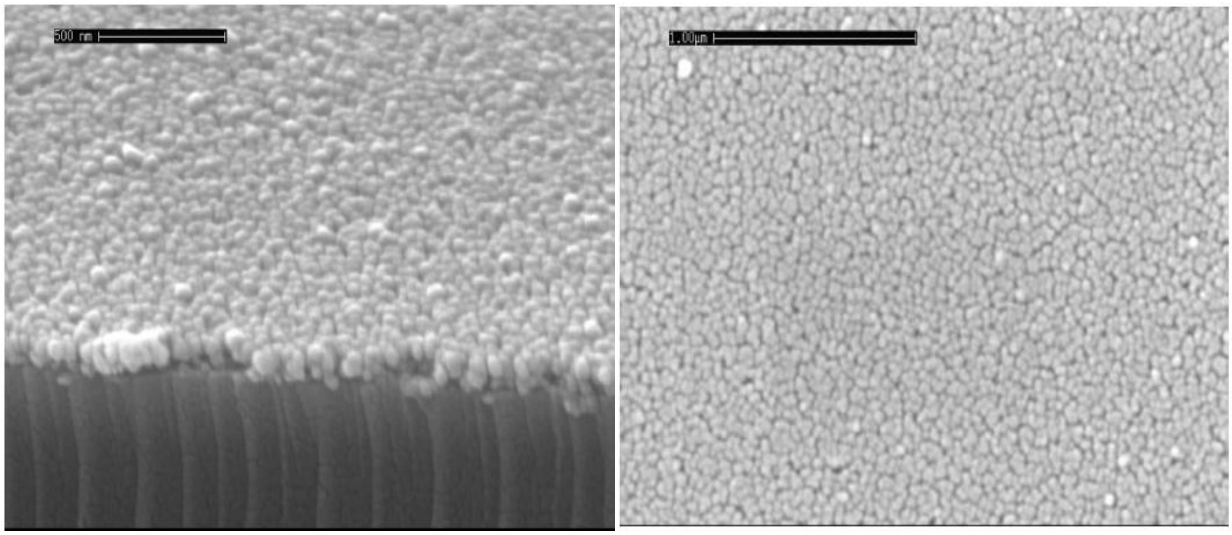

Figure 4.6: SEM images of F5 films. Left images: cross-section; right images: top-view.

The optical characteristics of the films annealed in air at 600°C for 2 *h* (Table 4.1) were obtained by elaborating their transmittance spectra displayed in Figure 4.7 and the reflectance ones. The values reported in Table 4.1 are the average ones in the whole 400-800 *nm* range (visible region). As expected, increasing the film thickness the average absorbance increased going from 0.50% (F2) to 1.9% (F6). Nevertheless, the average transmittance of films was higher than 90% except for the thickest film F6 being equal to 88.3% (Table 3.1). The optical bandgap values revealed that the electronic structure of ZnO nanocrystals was almost the same for these films. The extracted values were typical for ZnO Sol-Gel derived films [15]. The greater difference between the transmittance curves displayed in Figure 4.7 concerned the near-UV region where an absorption tail was noticed for each film. This tail appeared enhanced by increasing the concentration of the stock solution (Figure 4.7). This behaviour could be related to the different residual porosity of the films due to the solvent evaporation and to the decomposition of organic molecules originating during the transformation from amorphous to nanocrystalline ZnO films.

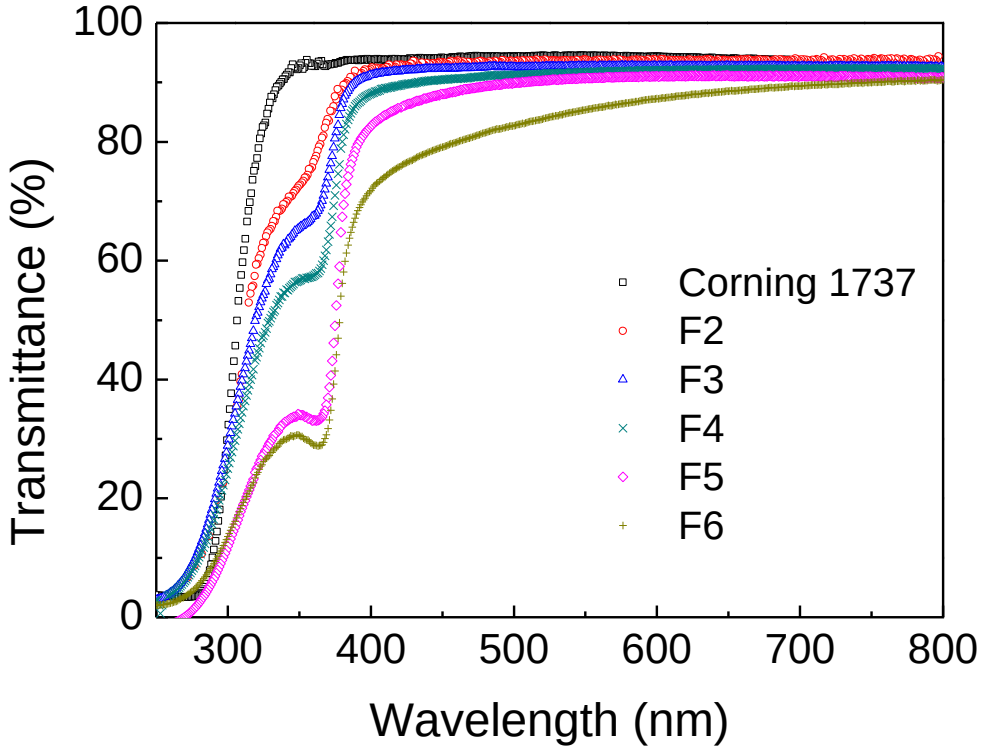

Figure 4.7: Optical transmittance spectra of ZnO F2–F6 films obtained from solutions with different ZAD molar concentrations. The spectrum of the glass substrate is reported.

1.3 ZnO crystallization: the role of the heat treatments

In Figure 4.8 the electrical resistivity (ρ) values of the films annealed in different conditions are displayed in comparison with the average ZnO nanocrystals size.

All F2-F6 films were annealed in air at 600°C for 2 *h*. Some F2-F6 films were subjected to an additional annealing (after the annealing in air) at 250°C for 0.5 *h* either in nitrogen (F2b-F6b)* or in forming gas (F5c). The scheme of the heating treatment is shown in Figure 4.9.

With respect to the literature data, the values obtained for the films annealed in air were in the same order of magnitude [16] or lower [6, 12].

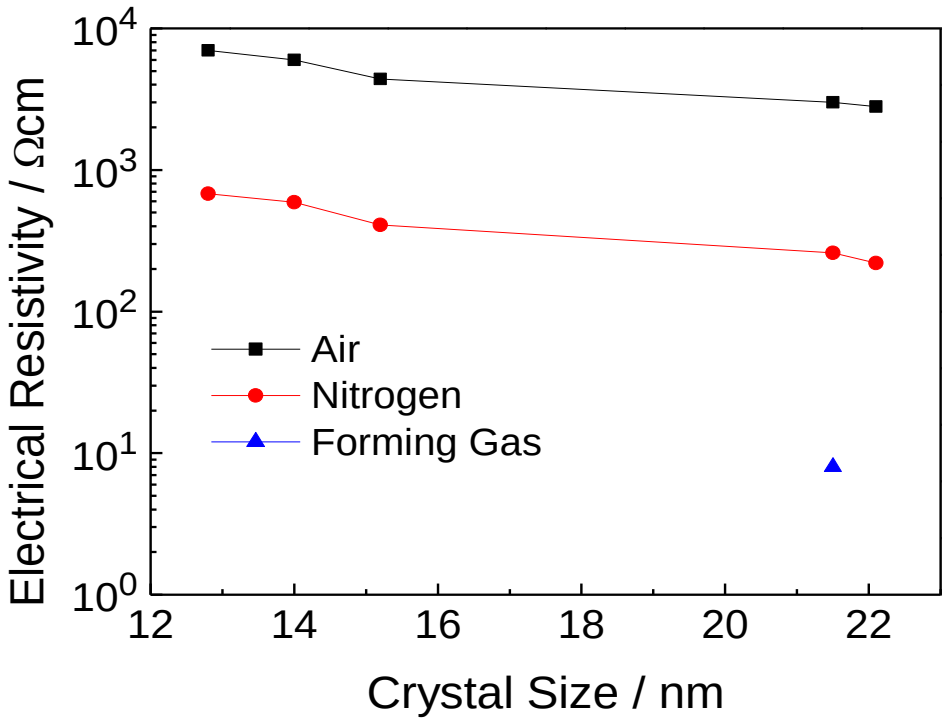

Figure 4.8: Electrical resistivity vs. average crystal size of F2-F6 ZnO films in different annealing conditions: (■) in air at 600°C for 2 *h*, (●) post-annealed in nitrogen at 250°C for 0.5 *h*, (▲) post-annealed in forming gas at 250°C for 0.5 *h*.

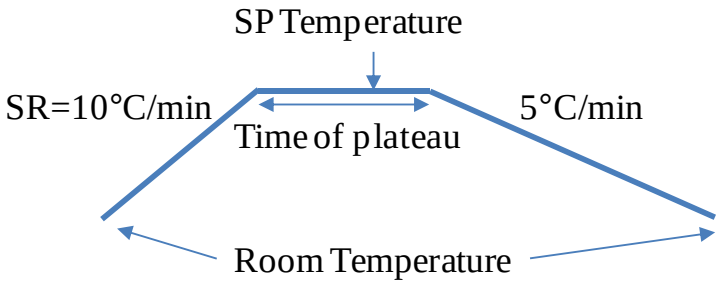

Figure 4.9: Scheme of annealing treatments.

The electrical resistivity decreased as the average of ZnO nanocrystals size increased. This corresponded to an increase of the film crystallinity degree as well (see Figure 4.3). This effect can be attributed to an enhancement of the carrier mobility. As a matter of fact, when the grain size and the film crystallinity increased, the grain boundary density and the scattering of the free carriers at grain boundaries decreased [5], so that the carrier mean free path and the carrier mobility increased [17] leading to a reduction of the resistivity [18]. On the other hand, films post-annealed in nitrogen ambient (F2b-F6b) showed a lower electrical resistivity with respect to films annealed in air (about one order of magnitude). Furthermore, the film post-annealed in forming gas (F5c) showed a lowest resistivity (8 $\Omega \cdot cm$), about three order of magnitude lower than the resistivity of films annealed in air (Figure 4.8). In fact, ZnO is an intrinsic semiconductor whose electrical conduction depends on lattice defects like oxygen vacancies, interstitial (Zn^{2+} - 2e) pairs, cation and anion vacancies, which contribute to a reduction of the electrical resistivity [19] by increasing the free electron and hole densities. Therefore, both inert and reducing annealing induces an increased oxygen vacancies concentration, thus decreasing the electrical resistivity of the films [20].

The crystallization of ZnO starting from an amorphous film was deeply investigated by Fujihara et al. [21]. They underlined that the Sol-Gel process was characterised by the post-deposition crystallisation with the temperature and rate of the crystallisation strongly influenced by solution chemistry. Moreover, the heterogeneous nucleation prevailed on the homogeneous nucleation due to the low thickness of the films and the presence of defects at the film/substrate interface, such as pores and decomposed organic molecules favouring the formation of nuclei [21]. In this PhD research a crystallisation temperature range from 500 to 600°C was explored as the decomposition temperature of zinc complexes containing TEA was expected to be higher than 400°C [22]. In particular, in order to evaluate the combined effect of both time and temperature on the crystallisation, three different times were selected (0.5 *h*, 1 *h* and 2 *h*, and heat treatments were performed at 500, 550 and 600°C, (see Table 2.5). From the XRD patterns of the F5 - F14 annealed films, the ZnO average crystal sizes were evaluated. Their trend is displayed in Figure 4.10. These data indicate that in order to obtain ZnO nanocrystals with an average size of about 20 *nm* at the lowest temperature (500°C) a longer time (2 *h*) is required whereas at the highest temperature (600°C) a shorter time (0.5 *h*) suffices.

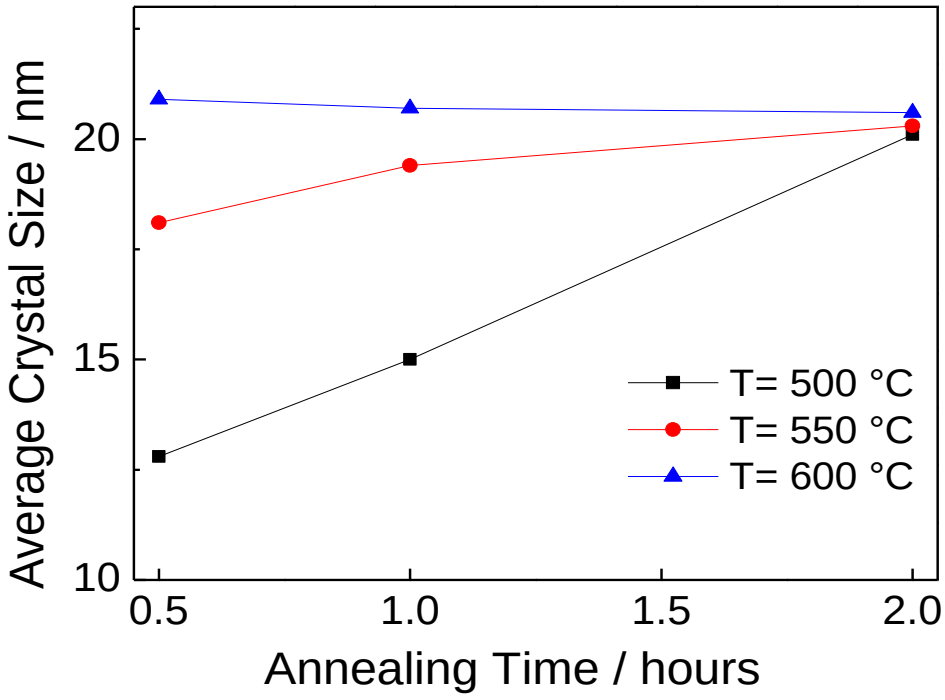

Figure 4.10: Average ZnO crystal size vs. annealing time at three different temperatures: 500, 550 and 600°C.

When the crystallisation started from an amorphous matrix, the driving force for the nucleation was related to the reduction of free energy connected to the transformation from the metastable amorphous state to the corresponding crystalline one. At lower temperatures the difference between the melting point of the crystalline phase and the nucleation temperature was higher, making the driving force for the crystallization larger. Simultaneously, the growth rate was low, giving nanocrystals a low average size. On the other hand, at higher temperatures the crystals growth rate progressively increased thus reducing the crystallization under kinetic control. Therefore at 600°C, increasing the annealing time, the average ZnO nanocrystals size kept its value of about 20 *nm*. The resistivity was strongly influenced by the grain size. Consequently, it was expected that the resistivity of the F8, F10 and F12 (see Table 2.5) would be the same. In fact, when films were annealed in air their resistivity was ~ $3 \cdot 10^3$ $\Omega \cdot cm$. Moreover, the optical characteristics were the same, as shown in Figure 4.11.

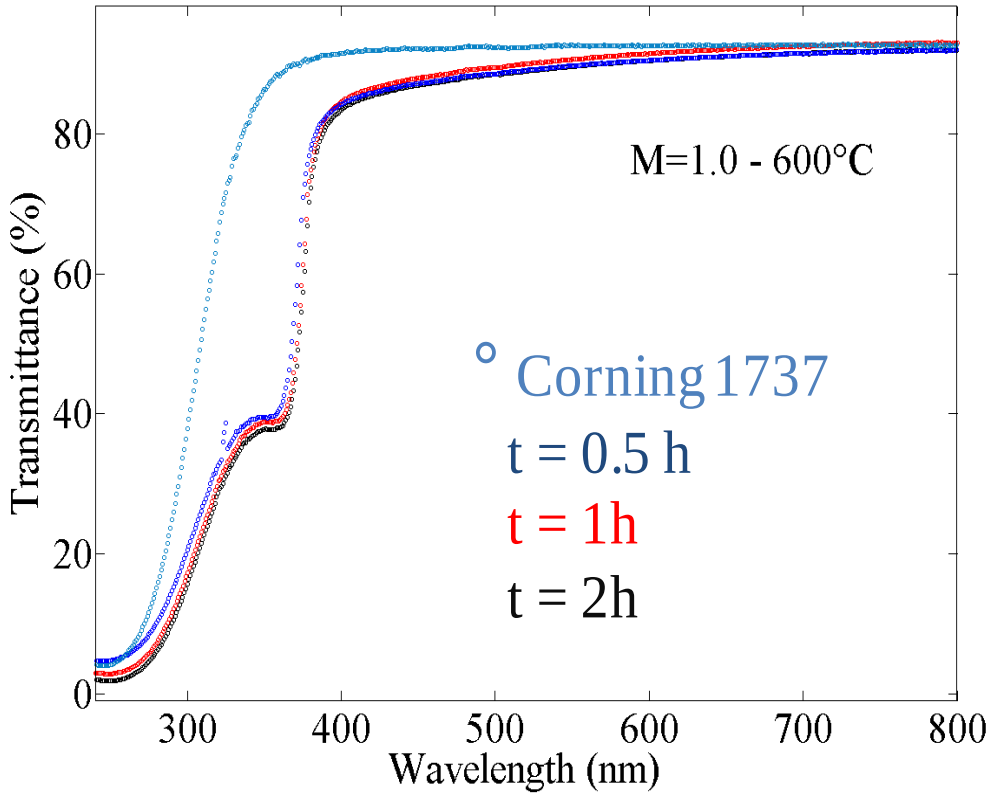

Figure 4.11: Optical Transmittance of ZnO thin films annealed in different conditions: 600°C for 0.5 *h* (F8), 550°C for 1 *h* (F10) and 500°C for 2 *h* (F12).

1.4 The Post-annealing effect

As can be seen from Figure 4.8, the minimum electrical resistivity of ZnO films was about 8 Ω·*cm*. This value was measured on F5 films post-annealed in FG at 250°C for 0.5 *h* (F5c). In literature, the interpretation of this result is still under discussion.

ZnO is an intrinsic n-type semiconductor [23] and the post-annealing in FG may be equivalent to dope films by hydrogen. Nevertheless, the hydrogen should not be able to contribute to the conduction in semiconductor materials because, typically, it acts as an amphoteric impurity. In a p-type semiconductor it acts like H+ (donor) dopant and, vice versa, in an n-type material such as H-(acceptor) dopant [24]. Thus, the

electrical conduction is hindered by hydrogen. However, Van de Walle theoretically showed that hydrogen helps the conductivity of ZnO, acting as a donor atom [25]. This result was experimentally proven by several groups [26, 27].

At present there are two types of shallow hydrogen donors proposed by first-principles calculations. The first one forms when a hydrogen atom is incorporated on an interstitial bond-centred lattice site (H_{BC}) [25], while the other is caused by the occupation of an oxygen vacancy by a hydrogen atom (H_0) [28]. Lavrov et al. [29] investigated these two hydrogen donors in bulk ZnO and found activation energies of 53 *meV* for H_{BC} and 47 *meV* for H_0, respectively. They also found that H_{BC} was unstable by annealing above 200°C and provided evidence that H_{BC} defected recombine to electrically inactive H_2 molecules. The thermal stability of H_0 was mainly studied by photoluminescence spectroscopy.

This research activity shows that H_0 is stable up to 500-550°C. The ZnO resistivity may therefore be reduced thanks to hydrogen doping. Moreover, it was found that using a mixture of hydrogen and nitrogen (FG) for film post-annealing the electrical properties of ZnO thin films were improved.

The next section reports the effect of the post-annealing in FG on electrical resistivity of F5 ZnO films under various conditions*. First of all, the effect of temperature was investigated. The electrical resistivity versus post-annealing temperature is shown in Figure 4.12.

*If not specified, all studied films, in the next, have been deposited from a solution with a molar concentration of zinc precursor equal to 1.0 M and annealed in air at 600°C for 0.5 *h*.

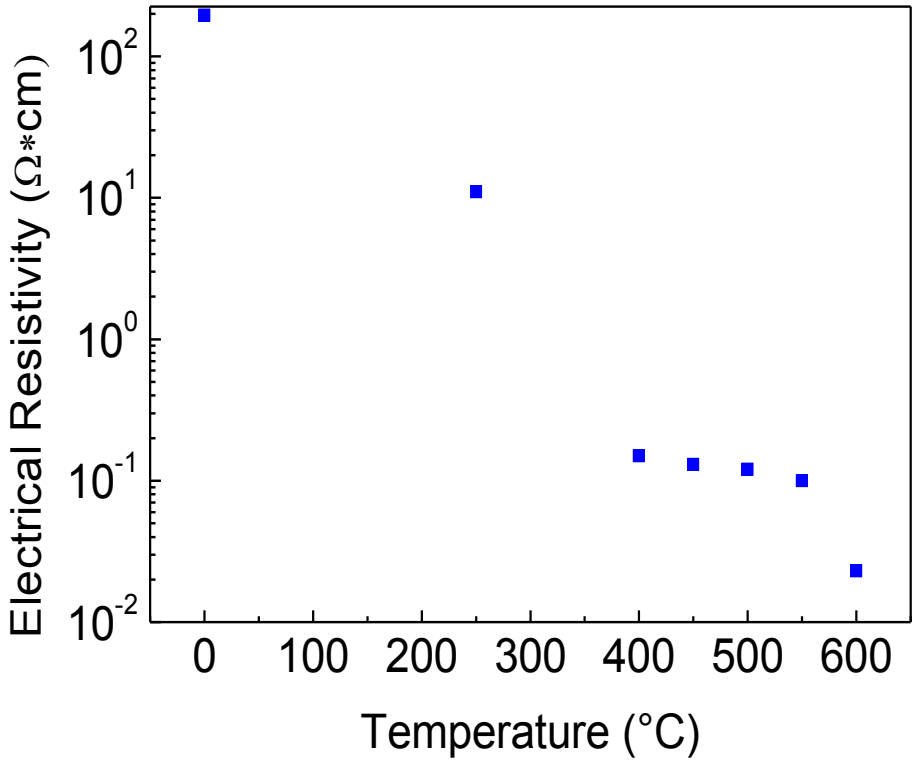

Figure 4.13: Effect of post-annealing temperature in FG on ZnO film resistivity. The time of treatments is 0.5 *h*.

At low temperatures the hydrogen ability to diffuse inside the film was poor, bringing to a higher electrical resistivity ($> 10^1\ \Omega{\cdot}cm$). When the post-annealing temperature increased, the electrical resistivity decreased thanks to the diffusion of hydrogen inside the film structure and the consequent formation of H_0 and H_{BC} defects. However, H_{BC} donors were unstable at high temperatures and therefore by further increasing the temperature the H_0 density increased while the H_{BC} population decreased. As a result, the formation of a plateau in term of electrical resistivity was expected (as also confirmed by the experimental results). At higher temperatures (above 550°C), ZnO films completely reduced to Zn metallic film and the minimum electrical resistivity was obtained as the annealing was performed at 600°C. As a matter of fact, at this temperature the films transparency was very low due to the formation of a great number of metallic zinc atoms (interstitial Zn).

Consequently, the film reflectance increased and the transmittance decreased downstairs to 60% (average value over visible region of solar spectrum). The choice of the optimum treatment depended on the optical characteristics of the film. Figure 4.13 shows both transmittance and reflectance values (average over the entire visible region of solar spectrum) of ZnO single layer films (F5) as a function of heat treatment temperature in FG. The treatment time is equal to 0.5 *h*. In this graph, transmittance and reflectance values of an untreated F5 film in FG are reported.

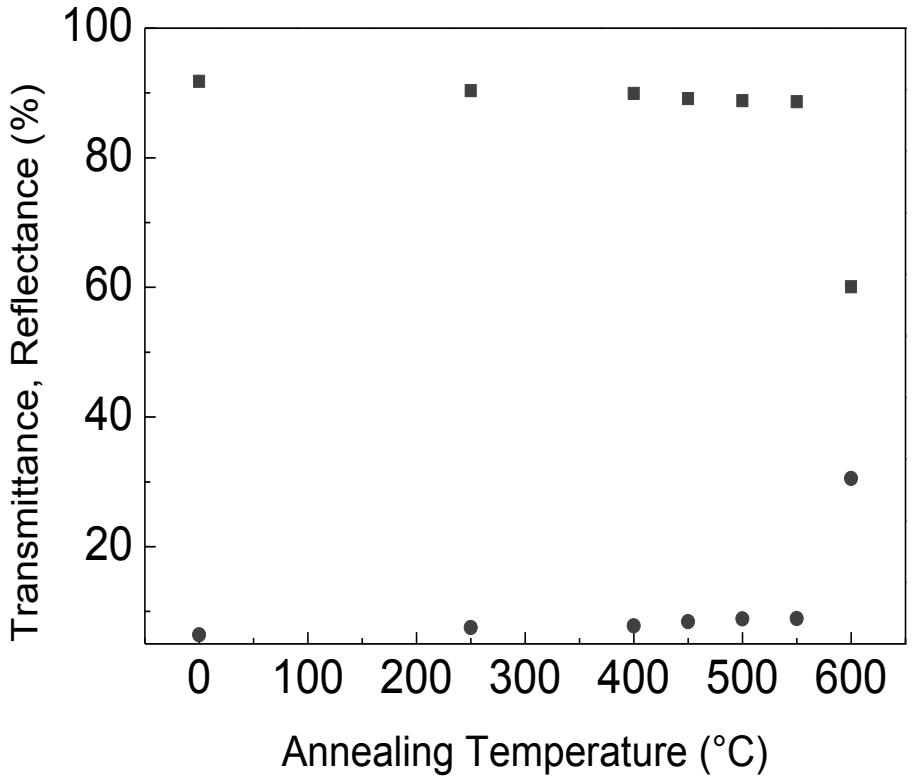

Figure 4.13: Average Transmittance (black square) and Reflectance (grey circles) values of single layer ZnO films (F6) as a function of post-annealing temperature in FG.

The effect of hydrogen amount in FG mixture on electrical resistivity was studied. Figure 4.14 shows the electrical resistivity versus hydrogen amount. All films were treated at 450°C for 0.5 *h*.

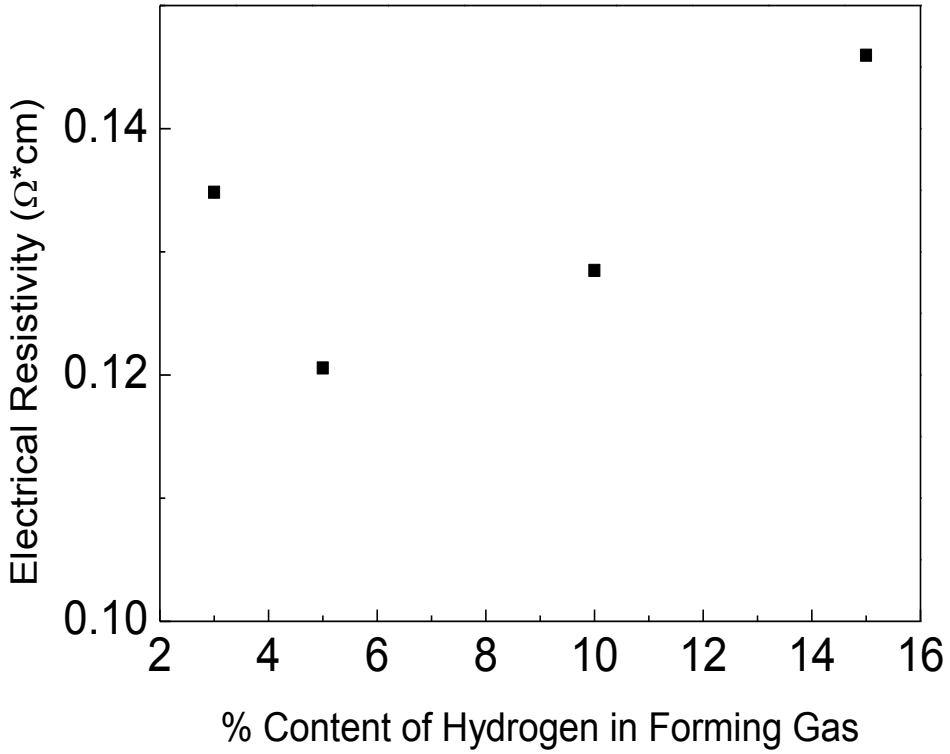

Figure 4.14: Electrical resistivity of single layer ZnO films (F6) treated at 450°C for 0.5 *h* in FG mixture, with a composition of H2 ranging between 3 and 15% (by volume).

As can be seen, the minimum electrical resistivity was measured on films treated in FG with 5% hydrogen content (by volume). Afterwards, all films were post-annealed in this N_2/H_2 mixture.

These results show that the best trade-off between the lowest resistivity and the highest transmittance was obtained by performing the post-annealing at a temperature of 450°C. As a matter of fact, this temperature allowed reaching a resistivity of 0.12 $\Omega \cdot cm$, several orders of magnitude lower than the value obtained on films post-annealed in air or an inert environment (nitrogen). Moreover, an average transmittance of about 90% in the visible region was measured. Treatments at higher temperatures do not modify the resistivity, unless a temperature of 600°C is reached creating an unacceptable condition from an optical point of view.

Finally, the effect of treatment duration has been investigated (Figure 4.15).

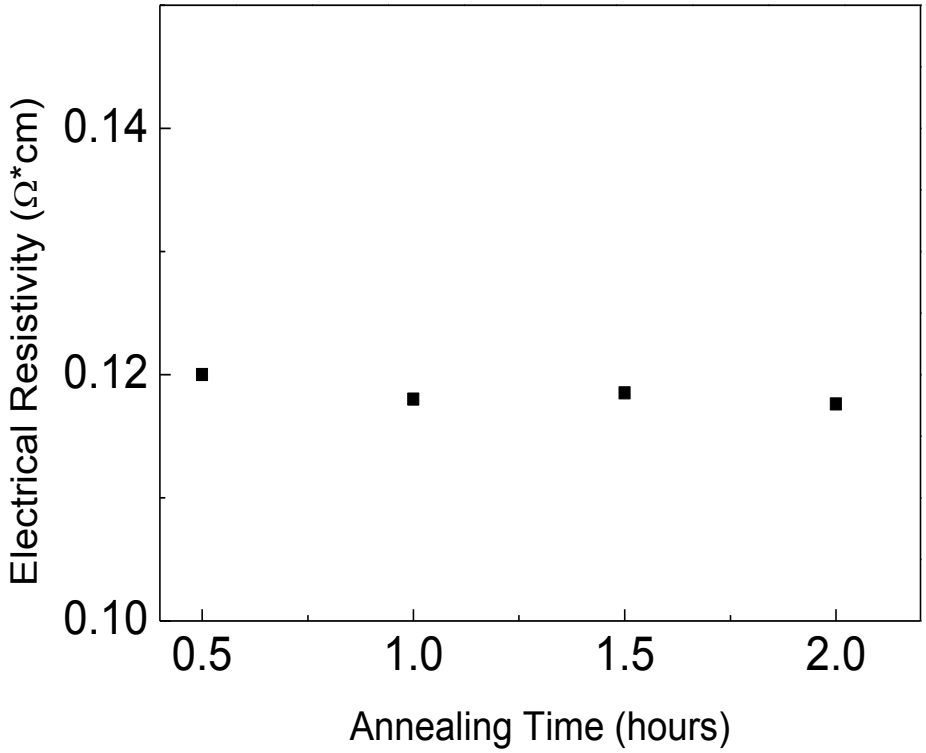

Figure 4.15: Electrical resistivity of single layer ZnO films (F6) as a function of post-annealing time in FG. The Annealing temperature is 450 °*C*.

In the considered time range, the film resistivity was independent from post-annealing time. These results suggested that the doping with H_2 was mainly controlled by the diffusion ability of gas inside the ZnO lattice. As known, this phenomenon depends exponentially on the temperature and it is quite independent from the time, unless considering a time durations higher than 10 *h*, often prohibitive for the dissipated energy amount.

In conclusion, all films analysed in this research, were post-annealed in FG (N_2/H_2 – 5*%*) at 450°C for 0.5 *h*. These conditions have shown the best properties both from an electrical and an optical point of view.

1.5 Boron effect on ZnO single layer films

In order to reduce the ZnO electrical resistivity, the doping with an external element has been studied. In this work, boron (B) has been used as donor element.

The boron precursor was added into the solution in the first step ("solution preparation") to achieve three nominal compositions: 0.5, 0.8 and 1.0% (in atoms) with respect to the zinc amount.

In particular, a systematic study was carried out in order to establish the optimal combination of zinc molar concentration in the solution and the boron atomic concentration.

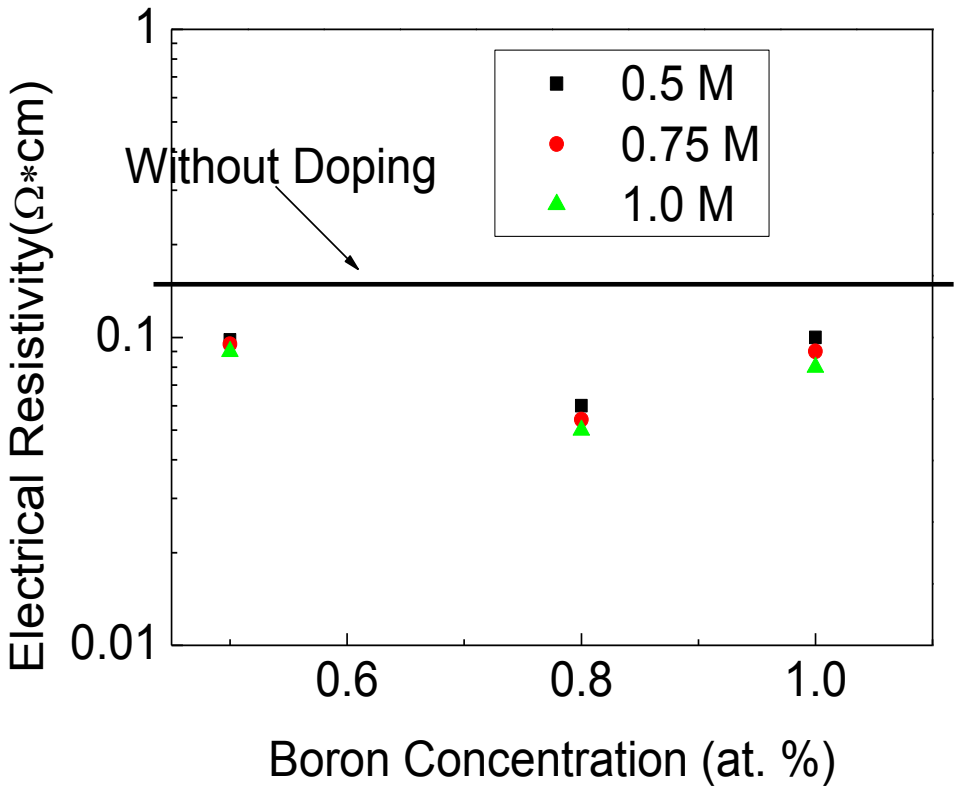

Figure 4.16: Electrical resistivity of ZnO:B single layer films versus atomic concentration of Boron.

The electrical resistivity of ZnO:B single layer films obtained from solutions at three different zinc molar concentrations (0.5, 0.75 and 1.0 M) was measured (solutions: S10 - S18, Table 2.3). These values are reported as a function of doping concentration in Figure 4.16.

This Figure reports the resistivity of ZnO single layer films. As Boron atoms are trivalent elements their incorporation into the ZnO crystal lattice produces free carriers (electrons in the conduction band) with a consequent reduction of electrical resistivity. As expected, the boron doping reduced the resistivity of ZnO films even if the reduction is lower with respect to the expected one [30]. This fact may be due to a low substitution degree of Zn^{2+} with B^{3+} in the ZnO lattice in the case of Sol-Gel synthesis, because of the presence in the solution of complexing agents (such as TEA). Therefore, high temperatures (> 800 °C) are required to activate boron atoms from an electrical point of view, after films deposition. However, these temperatures cannot be used because of the glass substrates softening point. In any case, the lowest resistivity value is found for the ZnO:B film with an atomic percentage of B equal to 0.8 % (in atoms).

The dimensions of B^{3+} ion were lower than those of Zn^{2+}, therefore, their presence within the ZnO lattice constituted a defect. It is generally expected that the crystal growth ability of defective grains is lower than those of not defective [31]. The study of AFM images reported in Figure 4.17 is in line with this prediction. The average grain size of a ZnO single layer film is greater than that of a ZnO:B single layer film.

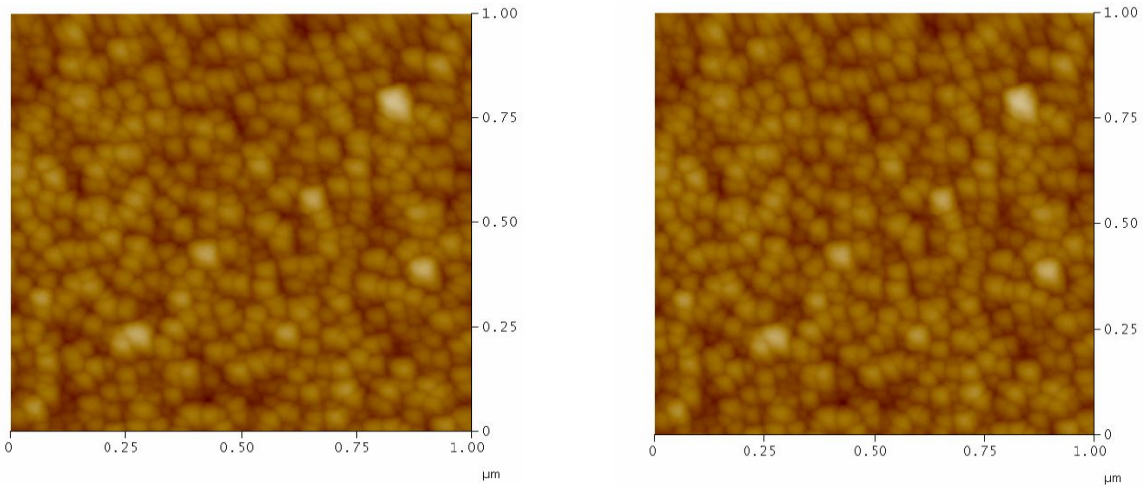

Figure 4.17: AFM micrograph images (top view) of ZnO single layer films. Left image: ZnO:B (0.8%); Right image: ZnO.

As previously discussed, in a Sol-Gel synthesis [30, 32] the substitution of Zn atoms with B (or other doping elements) atoms is usually difficult to be reached. Therefore, the reduction of electrical resistivity can be mainly attributed to an improvement of film morphology (porosity reduction) as Boron is added inside the film. Figure 4.17 clearly shows a lower residual porosity in the case of boron doped ZnO films. This point will be deeply discussed in the case of multi layer ZnO films where the effect of Boron doping on films morphology is more evident.

2. ZnO thin films – Multi layer

The TCO thickness is one of the most important parameter in PV applications as it strongly affects both the electrical and optical film properties and therefore solar cell performances, as already discussed in Chapter 1.

As reported in the first chapter and according to the experimental results previously presented, an increase in the film thickness entails the decrease of both the resistance and the optical transmittance. A sheet resistance in the order of 10 $\Omega/\square$ is given by acceptable values of ZnO films thickness while maintaining the transmittance in the visible region of solar spectrum higher than 80-85%. A usual film thickness is 1-2 μm.

The first part of this research activity paid a special attention to the optimisation of single layer ZnO film thickness by increasing the starting solution viscosity and the zinc precursor molar concentration according to Landau-Levich equation:

$$t = 0.94 \frac{(\eta \cdot \nu)^2}{\gamma_{LV}^{1/6} \cdot (\rho \cdot g)^{1/2}} \qquad (4.1)$$

This equation was already discussed in Chapter 2 and it shows clearly that the film thickness tends to increase by increasing the viscosity (ν) and it decreases by increasing the solution density (ρ). In this research the viscosity was increased according with the Zn molar concentration. The sol density increased by increasing the solution viscosity. A trade-off was expected on film thickness, as shown in Figure 4.18.

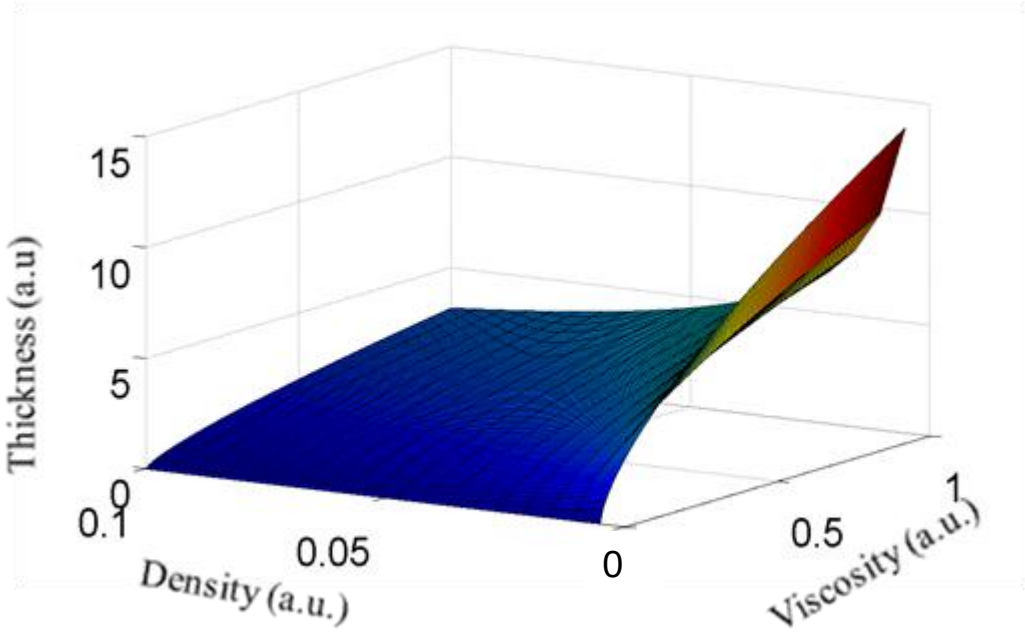

Figure 4.18: Film thickness versus Sol viscosity and density at a fixed value of liquid–vapour surface tension and withdrawn speed.

The Landau-Levich equation was implemented and the film thickness shape was reported versus sol viscosity and the density in Figure 4.18 by fixing the liquid-vapour surface tension and the withdrawn speed. It comes that by increasing the sol density the effect of sol viscosity on film thickness is poorer, according with the experimental results previously reported. The film thickness increases with molar concentration (from 50 up to 125 *nm*) but a saturation effect occurs when the molar concentration is higher than 1.0 M. The maximum single layer ZnO film thickness is about 125 *nm*.

In order to have thicker films, multi layer ZnO films were deposited by following the procedure reported in Figure 2.8. The next part of this chapter will focus on the characterisation of multi layer ZnO films and on the effect of Boron on films properties (0.8% atomic percentage).

All films were deposited starting from solutions with a molar concentration of zinc precursor equal to1.0 M and with different pH value. They were annealed in air at 600°C for 0.5 *h* (film crystallisation) and then post–annealed in FG at 450°C for 0.5 *h*.

2.1 Multi layer ZnO films at pH=7.66

Figure 4.19 shows the SEM images (top views) of multi layer films surfaces for both ZnO (left column) and ZnO: B – 0.8% (right column). Pictures on the top represent a case of 2 layers, pictures in the middles in case of 4 layers and finally, the pictures at the bottom in case of 8 layers.

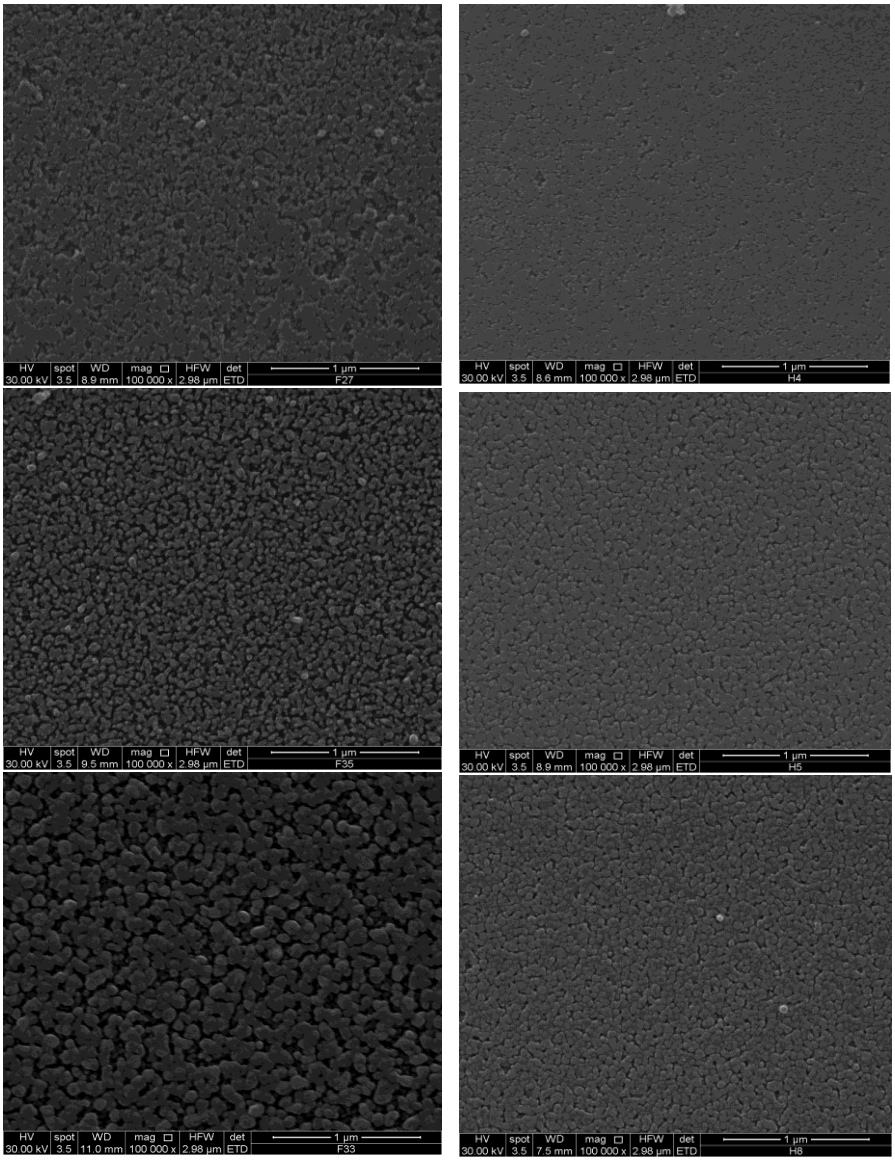

Figure 4.19: SEM images (top views) of multi layer ZnO films at a magnification of 100 000 x: undoped ZnO (Left side) and ZnO:B – 0.8% (Right side). Top: 2 layers; middle: 4 layers; bottom: 8 layers.

These images show good film uniformity even at low number of layers. Their porosity, which is already low even for 2 layers films (undoped: F27; doped: F39) decreases by increasing the number of layers while the cluster size (group of ZnO grains) increases as the number of layers gets higher.

To better highlight films homogeneity and low porosity a series of SEM images at different magnification (50 000, 100 000 and 150 000 x) of a 4 layers ZnO: B (F40) film are shown in Figure 4.20.

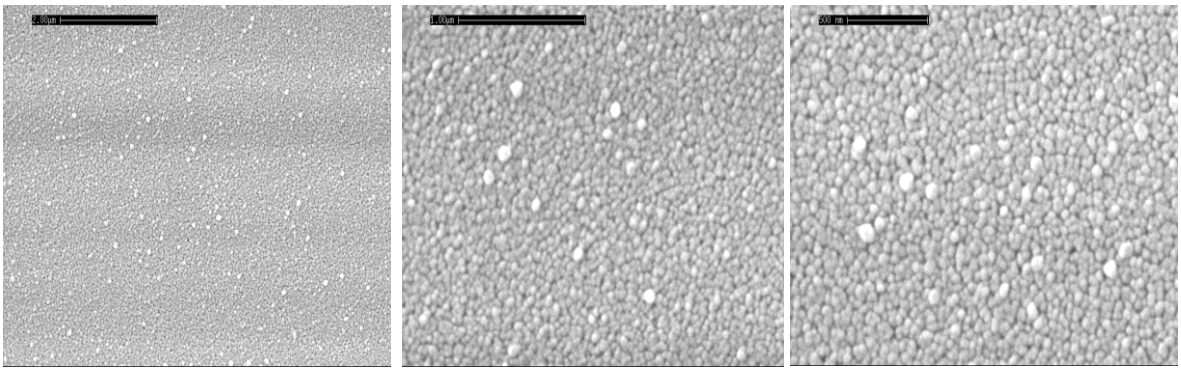

Figure 4.20: SEM images (top views) of 4-layered ZnO:B (F48) film at three magnifications: left image (50 000 x), central image (100 000 x) and right image (150 000 x).

Moreover, it is important to underline that B doped films appear more uniform than undoped films, as shown in Figure 4.19.

The thickness of multi layer ZnO films was evaluated from the cross-section of SEM images reported in Figure 4.21. The thickness was measured in several points of the layer. The average results of all measurements are presented in Figure 4.22.

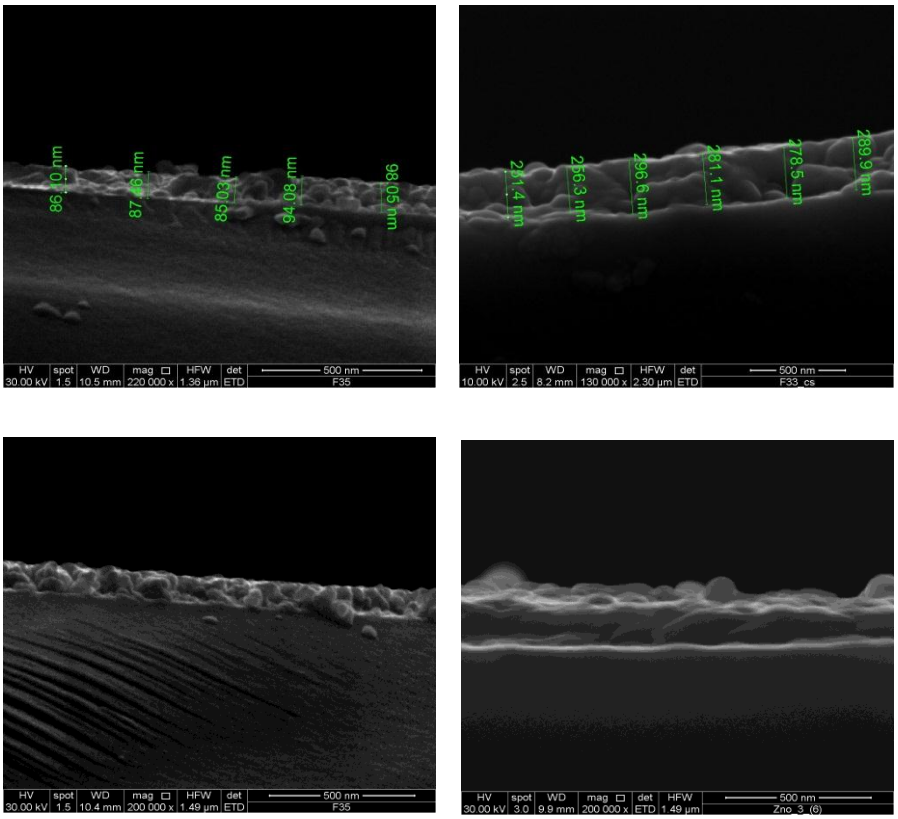

Figure 4.21: Cross-section SEM images of ZnO films: 2-layers (top left); 8-layers (top right); 2-layers ZnO:B (bottom left); 8-layers ZnO:B (bottom right).

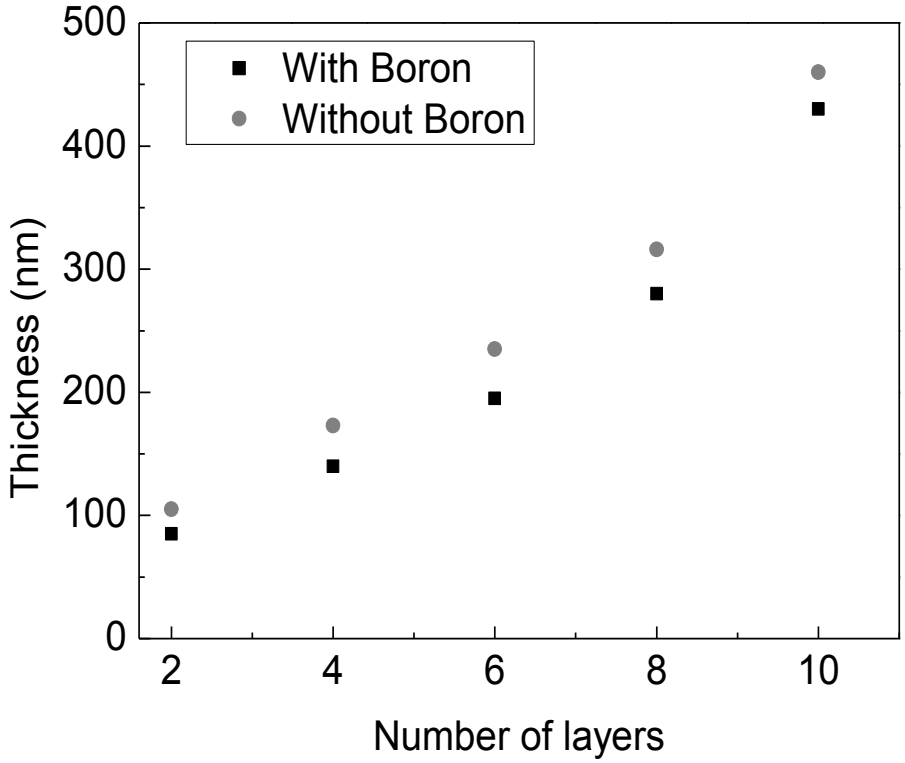

Figure 4.22: Film thickness versus number of layers for undoped (F27-F31) and B doped (F39-F43) multi layer ZnO films.

The film thicknesses range from 100 to 474 *nm* going from single layer to 10 layer film. The experiments showed that the film thickness of a 2 layer ZnO film is lower than the one of single layer film. This effect can be explained by two different hypotheses. According with to the first hypothesis, the film thickness decreases by repeat the number of TEA depositions because of the intermediate pre-annealing at 400°C for 10 *min* (see Figure 2.8) with the reduction of the film thickness. According to the second hypothesis, instead, the film thickness reduction would occur as a consequence of the partial dissolution of the film during its second immersion into the sol. As a matter of fact, the formation of ZnO film occurs only after the annealing at 600°C (final step of the procedure, see Figure 2.8).

AFM analysis also permitted to study the film morphology. AFM images are reported in Figure 4.23. These images confirm a films granular nature and the particle size trend obtained from SEM analysis.

For both doped and undoped ZnO films the RMS increased by increasing the number of layers. RMS for undoped ZnO films is equal to about 10 *nm* for 8-layer film and 12 *nm* for 10-layer film while for doped ZnO films it is about 9.8 *nm* for 8-layer film and 11.8 *nm* for 10-layer film.

Therefore, it can be said that RMS increases with the film thickness, as expected.

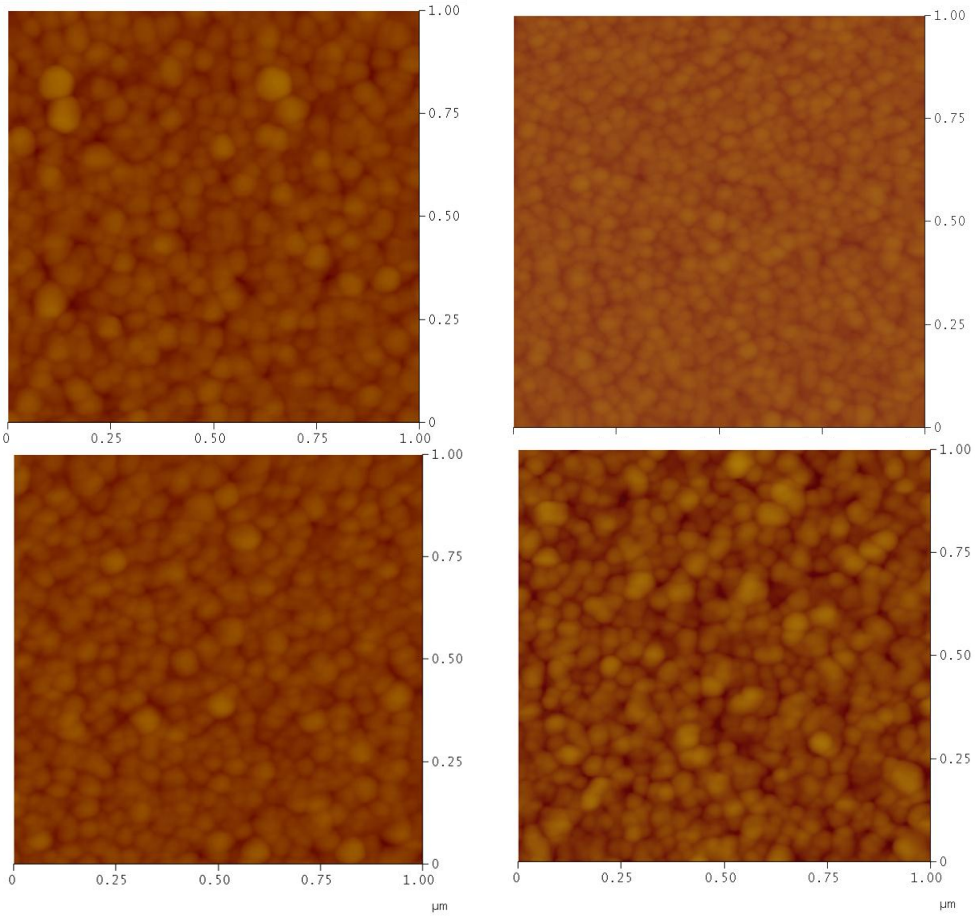

Figure 4.23: AFM micrographs of undoped (left column) and doped (right column) – 0.8% in atoms – ZnO films: 8 (top) and 10 (bottom) layers.

Both SEM and AFM analyses proved that the surface morphologies of ZnO films are strongly affected by the B doping. The granular structures disappeared with doping while grains got smaller. Furthermore, the homogeneity of surface morphology increased [30, 32].

Figure 4.24 reports the GIXRD spectra of multi layer ZnO films.

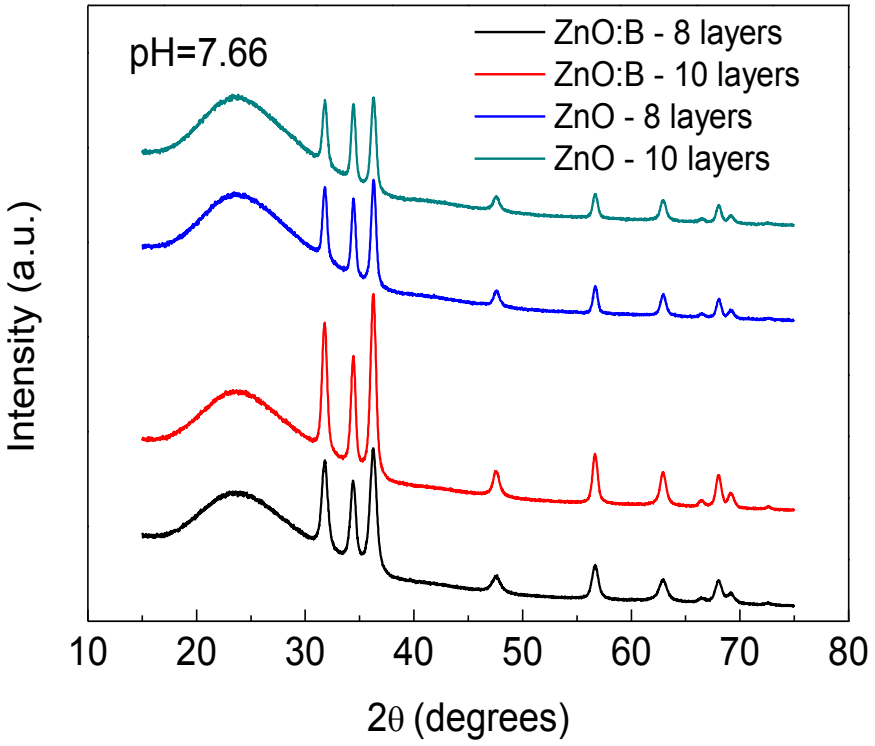

Figure 4.24: GIXRD spectra of ZnO films (Zinc molar concentration of starting solution equal to 1.0M).

The intensity of (101) and (002) peaks was lower in the case of B doped films. It is proved that in this case some lattice defects and distortions of the crystal lattice may occur [33]. The GIXRD patterns suggest that the incorporation of boron atoms leads to a suppression of the crystal growth. Therefore, the crystallinity of the doped films deteriorated. The crystallite size of films was calculated for both (101) diffraction planes by using Scherrer's equation. Results are reported in Table 4.2. As it can be seen, the crystal size of ZnO:B films is lower than ZnO films. In the case of B doping (which is a trivalent element) the concentration of zinc interstitials was reduced in favour of charge compensation, resulting in the suppression of ZnO grain growth and in the deterioration of cristallinity [34]. A similar trend was observed by both Addonizio and Diletto [35] and by Kim et al. [33].

Nevertheless, the reduction due to the B doping was lower than expected [33-35] as the doped ZnO films were deposited by either a sputtering or by a CVD technique. In the Sol-Gel method the doping with external

elements is a difficult point, as previous mentioned; in fact, the substitution of Zn atoms with B, Al or other dopants has to take place in the solution before the film deposition or after, during the annealing. This last requires very high temperatures (> 700-800°C) that are not acceptable for the softening point of the glass substrates. Moreover, the substitution in the solution is difficult to control and strongly affected by many factors such as pH, temperature or chelating agents. Boron atoms can therefore only partially substitute Zn inside the crystal lattice. The rest may give B-B clusters [31] in intra-grains regions or it can accumulate in grain boundaries. This hypothesis can possibly explain the higher uniformity and homogeneity of doped ZnO films respect to pure ZnO.

Table 4.2: Thickness (*t*) and average ZnO crystal size (*d*) of multi – layers doped and undoped ZnO films.

Film/N° layers	***t* (*nm*)**	***d* (*nm*)**
F30/8 (ZnO)	235	20.1
F31/10 (ZnO)	315	20.7
F42/8 (ZnO:B)	208	19.1
F43/10 (ZnO:B)	295	20.1

Figure 4.25 reports the electrical resistivity versus number of layers (for both undoped and doped ZnO films).

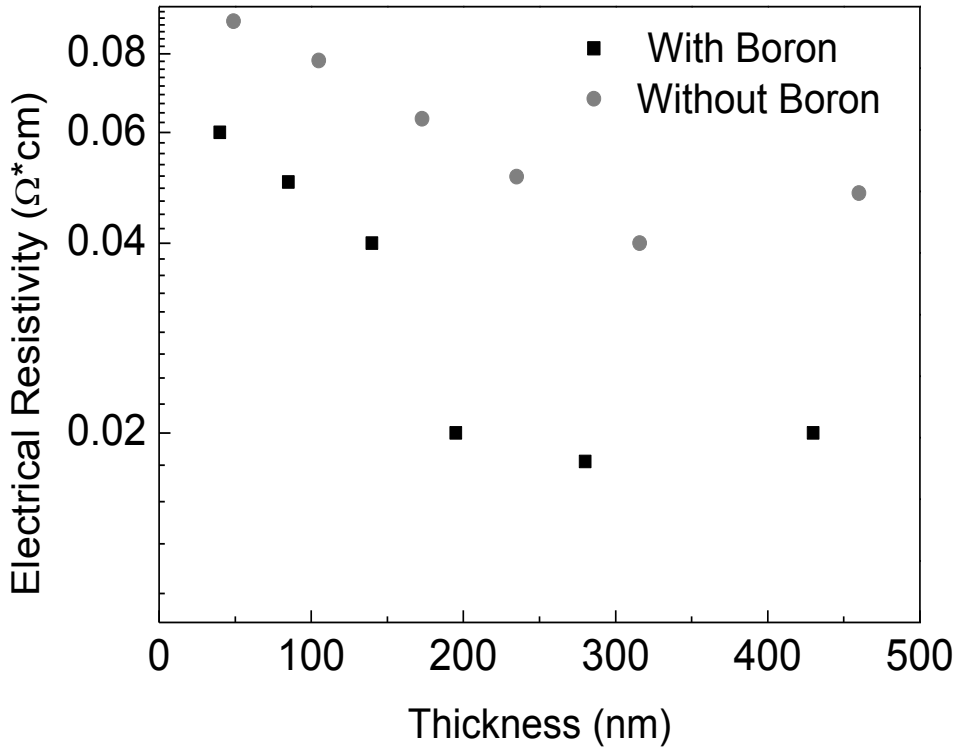

Figure 4.25: Electrical resistivity versus film thickness. Undoped ZnO films (F27-F31) and ZnO:B films (F39-F43).

The electrical resistivity decreased by increasing the film thickness. Its minimum value ranged between $1.96 \cdot 10^{-2}$ $\Omega \cdot cm$ for ZnO:B films and $4 \cdot 10^{-2}$ $\Omega \cdot cm$ for undoped ZnO. The difference was due to the Boron doping, as previously discussed.

An increase of the film thickness brought about the increase of grain crystal size and a decrease of the film porosity (as it can be seen from SEM and AFM images). As a consequence, the resistivity decreased thanks to an improvement of carriers' mobility.

Finally, the optical transmittance for F27-F31 films (see Table 2.6) is reported in Figure 4.26.

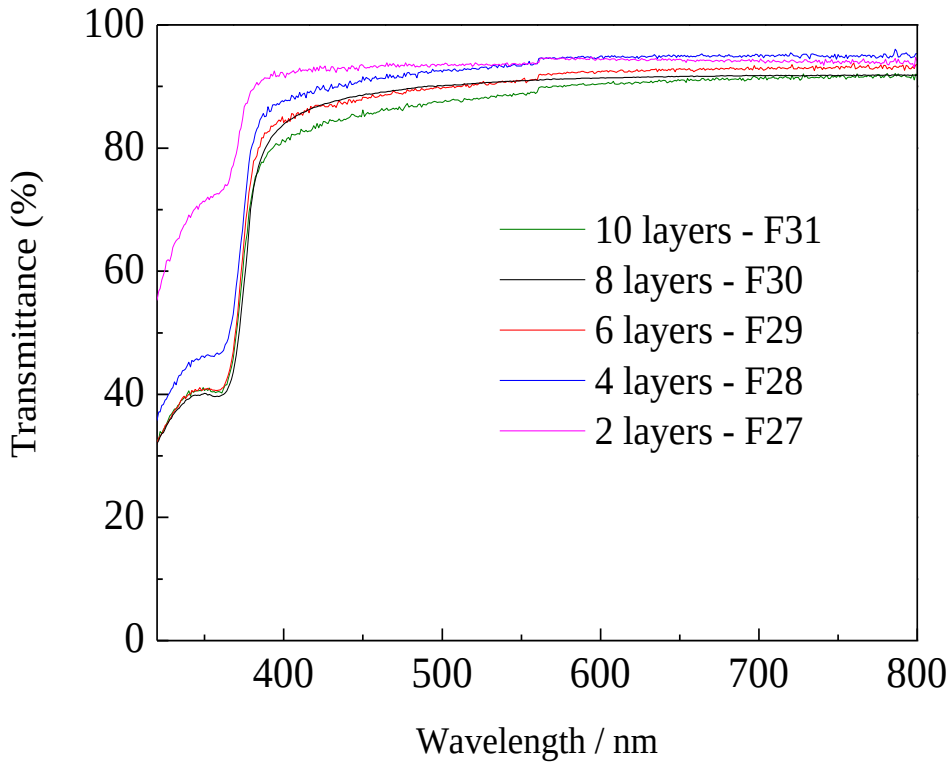

Figure 4.26: Optical Transmittance of F27-F31 undoped multi layer ZnO films.

As it can be seen, transmittance decreased by increasing the number of layers (film thickness). The average value over the visible region of solar spectrum was always higher than 88.5%. In the case of multi layer ZnO:B films the optical transmittance was a little bit higher, by 2%.

2.2 Effect of pH value

As discussed in Chapter 2, the solution pH value strong affected the ZnO crystal growth. ZnO crystal size was expected to increase by increasing the solution of pH level while falling in the range 7 - 9 [36].

Moreover, it is well known [36] that the pH affects the hydrolysis and condensation behaviour of the solution during gel formation and therefore, it influences the morphology of ZnO films [37].

The increase in pH clearly indicates an increase of alkaline nature of the prepared sols. This increase is attributed to hydrolysis of salts of weak acid in strong medium base.

In this PhD research the effect of pH on ZnO film properties is investigated. In order to do it, multi layer ZnO films were deposited from solutions with pH 7.66, 8.12 and 8.76 (Solutions S5, S7 and S8, see Table 2.1 and Table 2.2). Properties of multi layer ZnO films at pH 7.66 and the effects of multi-deposition were largely presented in the previous paragraph. It is to be noted that the best results in term of film transparency, electrical resistivity and uniformity were carried out on 8 layered ZnO films. Here the effect of pH on film properties is presented by considering 8-layerd ZnO films (both doped and undoped).

The film thickness is reported both for undoped and doped (0.8% B) ZnO films in Figure 4.27 as a function of pH value. The film thickness increased by increasing the pH value. This trend was due to an enhancement of ZnO crystal size [36-38]. The graph clearly shows that a reduction of the film thickness with the boron doping took place. This experimental result does not agree with previously published data [32]. Therefore our hypothesis is that the film porosity decreases by adding boron (as confirmed by AFM photographs) with a consequent thickness reduction.

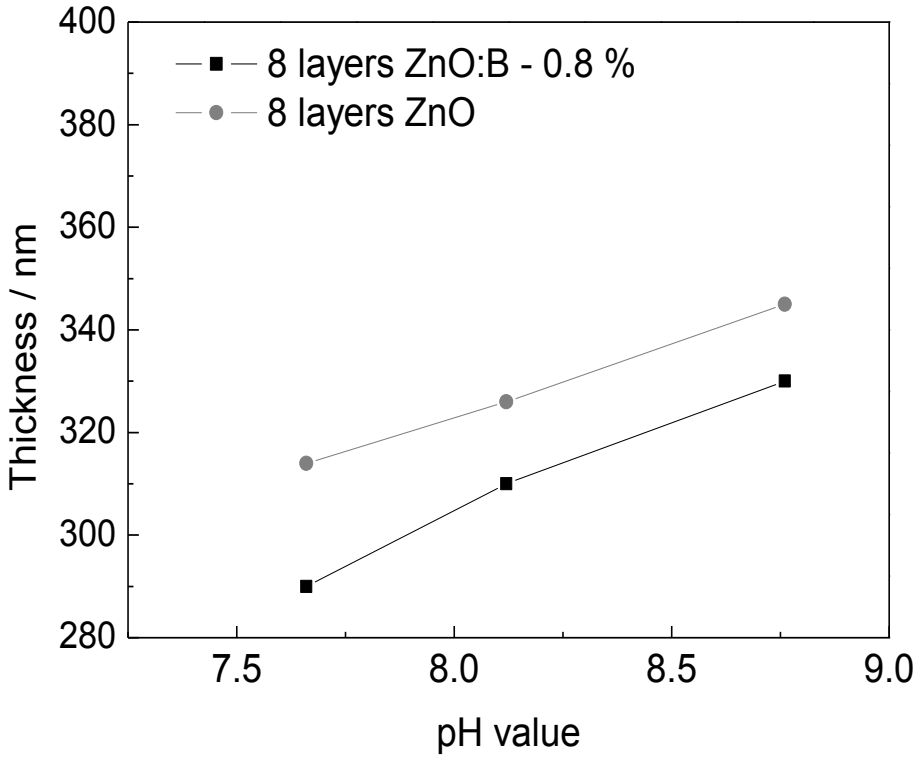

Figure 4.27: Effect of solution pH and doping on film thickness.

The film morphology was studied by SEM microscopy. The next Figure reports the SEM cross-section images of films F30/F42 (7.66 pH, undoped and B doped) and F37/F37d (8.76 pH undoped and B doped) (see Table 2.6). As it can be seen, the deposited ZnO films have good film uniformity and a granular nature.

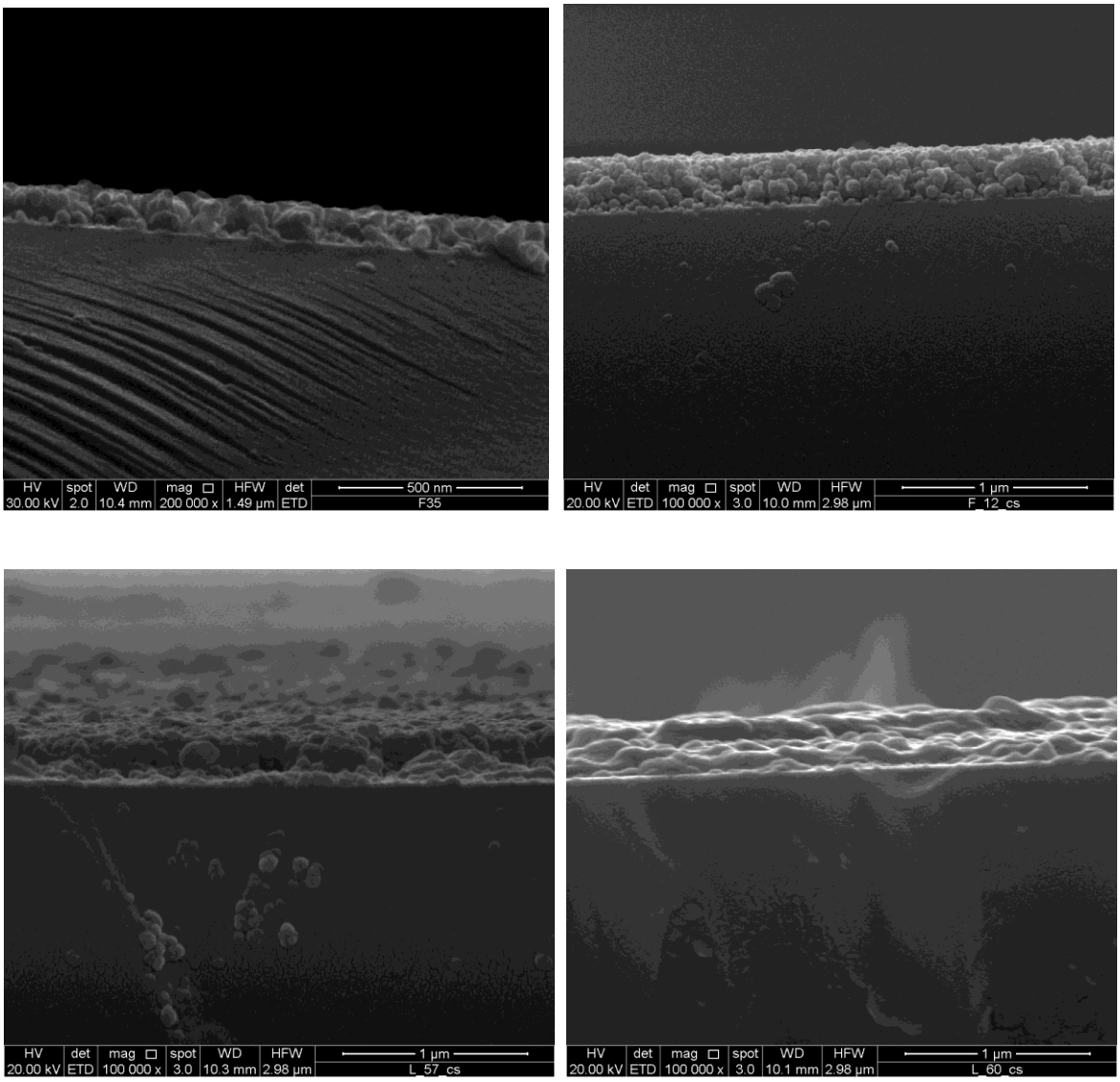

Figure 4.28: SEM Cross-Section of F30/F42 (Top) and F37/F37d (Bottom) ZnO films. In the left side undoped ZnO fims are reported. In the right side, ZnO:B films are shown.

The granular nature and the film porosity may be also observed from top-view SEM images, reported in Figure 4.29. F30/F42, F35/F35b (pH=8.12 undoped and B doped) and F37/F37d micrographs of ZnO films are presented (for films details see Table 2.6).

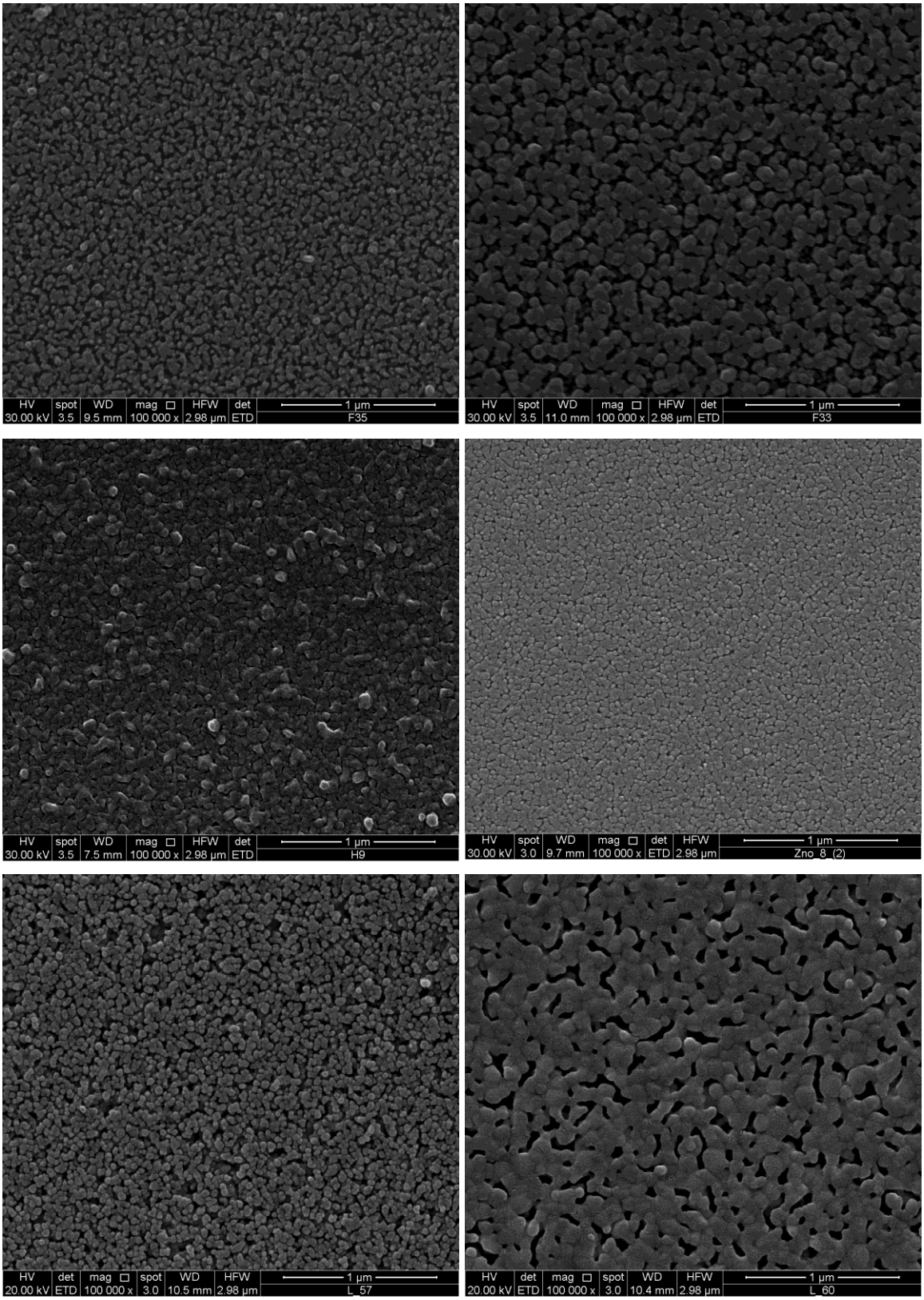

Figure 4.29: SEM micrographs of 8-layered ZnO films: left column (undoped); right column (ZnO:B – 0.8%). Top: pH=7.66; Middle: pH=8.12 and Bottom: pH=8.76.

Both Figure 4.28 and Figure 4.29 show a strong pH effect on film morphology. By increasing the pH the cluster size increased while the porosity decreased. Moreover, by doping the ZnO film, the formation of grains agglomerates was enhanced (see Figure 4.29). This behaviour was also observed in [32] and it may be due to the presence of the Boron into the ZnO lattice as interstitial element [39]. Consequently, the porosity decreased possibly causing a thickness reduction, as previously discussed. As a matter of fact, the formation of grains agglomerates also occurred in the case of Aluminium doped ZnO films (F37b – see Table 2.6), as can be seen from Figure 4.30.

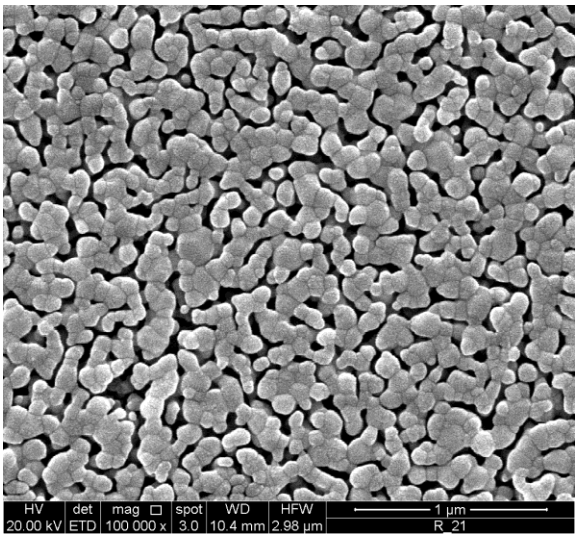

Figure 4.30: SEM micrograph of ZnO:Al (0.8% in atoms) deposited from S8b solution (see Table 2.2).

The morphology of the film reported in Figure 4.30 is very similar to that of F37d ZnO:B film (reported in Figure 4.29 –right bottom micrograph) confirming the effect of external elements (such as B or Al) on film morphology. In conclusion, in our procedure, the doping process improved the film uniformity by increasing the carriers' mobility rather than the electrical resistivity [18].

The effect of pH on ZnO grain size may be observed in Figure 4.31.

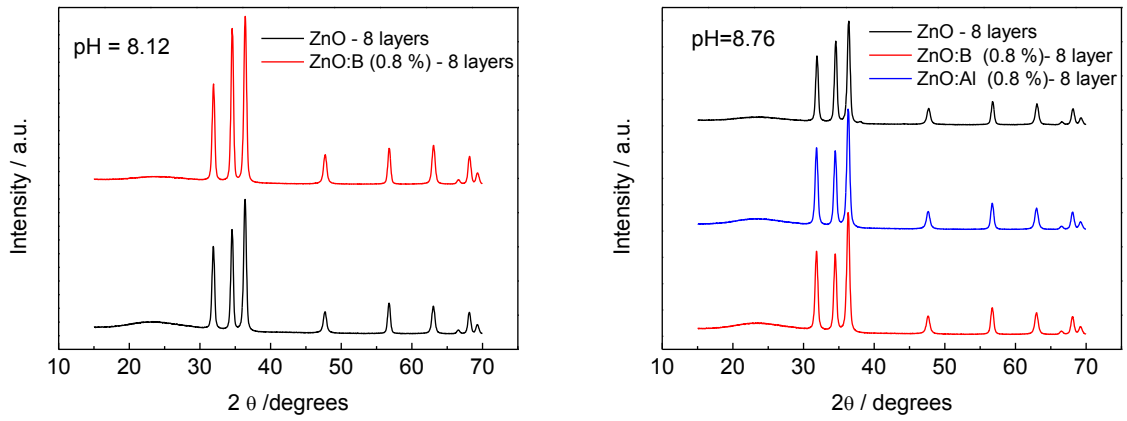

(a) **(b)**

Figure 4.31: GIXRD patterns: (a) 8-layered ZnO films (B-doped and undoped); (b) 8-layered ZnO films (B-doped, Al-doped and undoped).

From the GIXRD patterns shown in Figure 4.31 the average crystal size may be evaluated by applying the Scherrer method. It is about 21 *nm* for film from 8.12 pH and 21.7 *nm* for film from 8.76 pH.

The effect of doping on crystal structure can be observed in the same Figure. When atoms with different sizes are substituted into the ZnO lattice, some lattice defects and distortion of the crystal lattice may occur [33]. The GIXRD result suggests that the incorporation of boron or aluminium atoms leads to a suppression of the crystal growth and to distortion of diffraction planes. Therefore, the crystallinity of the analysed films deteriorated. The crystallite size of the films was calculated by Scherrer's equation. It is for ZnO:B at 8.12 pH about 20.5 *nm*, while for ZnO:B at 8.76 pH 20.8 *nm* and for ZnO:Al at 8.76 pH 21 *nm*. However, results showed that the reduction in crystal size was lower than expected [33, 36] due to the low substitution level of Zn atoms with B/Al atoms in the undertaken procedure (drawback of the Sol-Gel route). The pH level also affects the optical properties. In Figure 4.32, the total transmittance curves of F42 (7.66 pH), F35b (8.12 pH) and F37d (8.76 pH) ZnO:B are reported.

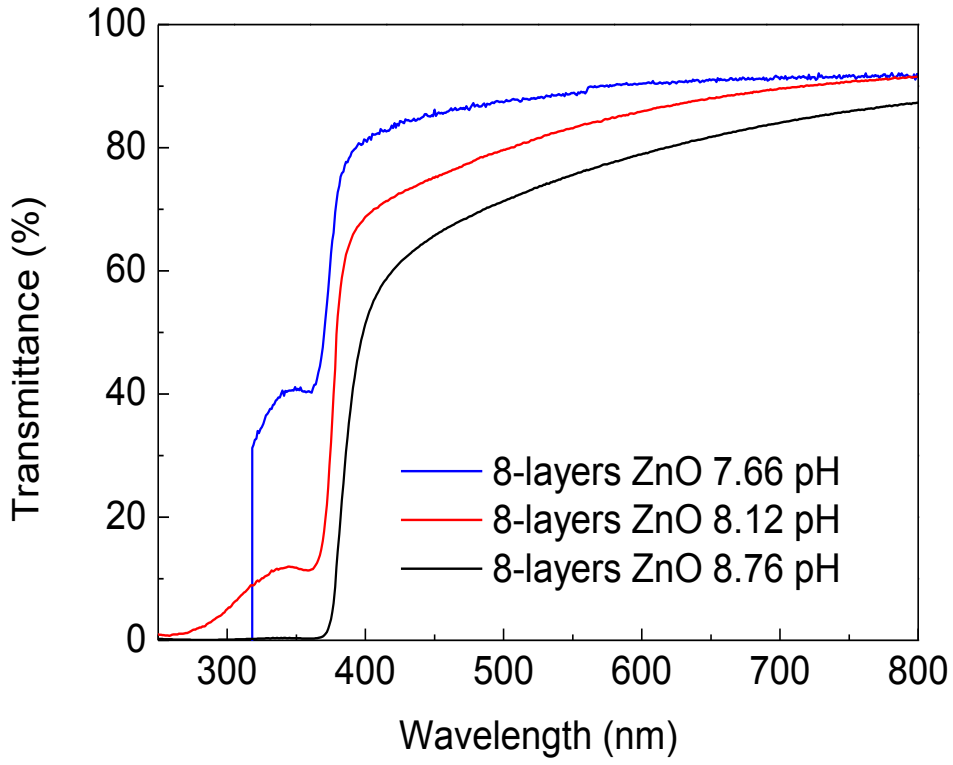

Figure 4.32: Total transmittance curves of 8-layers ZnO:B (0.8% in atoms) films for different pH values.

Figure 4.32 shows optical transmittance spectra of ZnO films prepared at different pH values. The transmittance for the film prepared at lower pH value was observed to be the highest (87% - average value in the visible portion of solar spectrum). The transmittance of the film decreased as the pH value increased. This can be ascribed to the formation of larger particles of ZnO by increasing the pH value which causes scattering of light [36]. The optical bandgap of the ZnO thin films were determined by plotting $(\alpha h\nu)^2$ against the photon energy $h\nu$, as discussed in the Chapter 3. The bandgap was found to be 3.25 *eV*, 3.24 *eV*, 3.22 *eV* for the pH values of 7.66, 8.12 and 8.76, respectively. The grain size increased by increasing the pH of the precursor solution. This may be explained by the increase of grain size [39]. This decrease in bandgap caused a strong red shift in the optical spectra, due to agglomeration of the nanocrystallites into larger crystallites. In the case of ZnO films from 8.12 and 8.76 pH solutions, the total transmittance – average value in the visible region – were 83% and 80.3%, respectively. The reduction in total transmittance was balanced by an increase in the diffuse transmittance

(increase of light scattering). Figure 4.33 shows the diffuse transmittance curves of 8-layers ZnO:B films at the three considered pH levels.

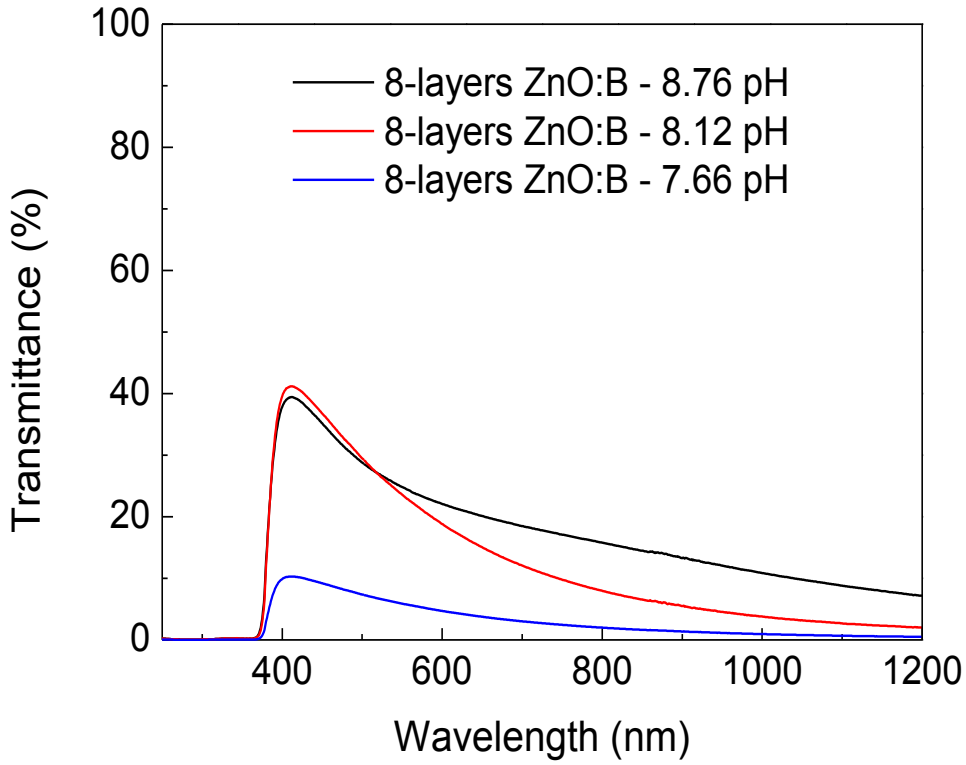

Figure 4.33: Diffuse transmittance curves of 8-layers ZnO:B (0.8% in atoms) films for different pH values.

Finally, the electrical resistivity is reported in Table 4.3. As it can be seen, the resistivity decreased by increasing the pH value. This decrease was attributed to the reduction of film porosity. It has to be noticed that the pH value strongly affected the carriers' mobility.

Table 4.3: Electrical resistivity of 8-layers ZnO films ([Zn]=1.0).

pH	**Dopant**	**ρ (*Ω·cm*)**
7.66	-	$4.5 \cdot 10^{-2}$
7.66	B (0.8% in at.)	$3 \cdot 10^{-2}$
8.12	-	$3.9 \cdot 10^{-2}$
8.12	B (0.8% in at.)	$2 \cdot 10^{-2}$
8.76	-	$2.9 \cdot 10^{-2}$
8.76	B (0.8% in at.)	$1.6 \cdot 10^{-2}$
8.76	Al (0.8% in at.)	$1.7 \cdot 10^{-2}$

Table 4.3 shows the electrical resistivity both for undoped and doped ZnO films. The electrical resistivity decreased by doping with external atoms (B or Al). This was due to an increase of the free electrons in the conduction band of the ZnO.

3. Devices Characterisation

In this section, the characterisation of electrical interface between gel derived ZnO films and a-Si:H (p-type) is presented. The G-ω method and the standard C-V techniques presented in the Chapter 3 are used. Furthermore, the investigation of a-Si:H p-i-n solar cells [40], deposited on ZnO:B films, is reported.

The properties of ZnO:B films chosen to play the role of TCO in TFSC are summarised in Table 4.4. They are 8-layers ZnO:B (F42: 7.66 pH) and 8-layers ZnO:B (F37d: 8.76 pH). Both films were doped with boron at 0.8% in atoms and deposited from a solution with a zinc molar concentration equal to 1.0 M and finally, annealed in air at 600°C for 0.5 *h* and post-annealed in FG at 450°C for 0.5 *h*.

Table 4.4: Properties of gel derived ZnO:B films used for TFSC deposition.

Parameter	**F42 (7.66 pH)**	**F37d (8.76 pH)**	**Optimum**
Electrical Resistivity (*Ω·cm*)	$3.3 \cdot 10^{-2}$	$1.5 \cdot 10^{-2}$	$< 10^{-3}$
Optical Transmittance (*%*)	87.5	80.3	> 80
Thickness (*nm*)	295	328	---
Surface Roughness (*nm*)	9	36	> 35

3.1 Electrical Interface Characterisation

As discussed in the Chapter 1, the electrical performances of a thin film solar cell strongly depend on the interface between the TCO layer and the active layer (a-Si:H), that may be schematised such as a metal-oxide-semiconductor (MOS) structure, see Figure 4.34. Parameters qualifying this interface are the density of states (D_{it}) and the interface resistance (R_{it}).

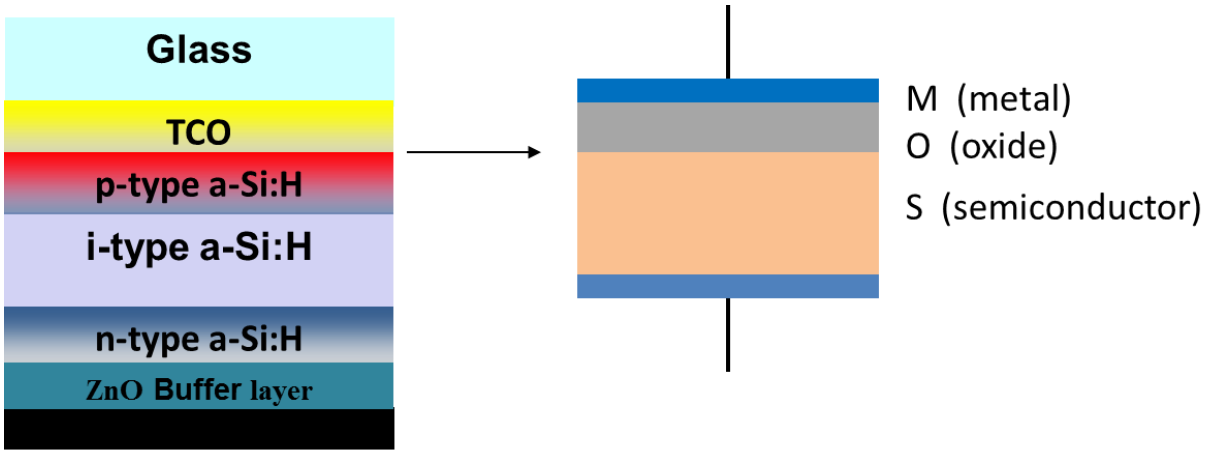

Figure 4.34: MOS schematisation of TCO/a-Si:H interface in TFSC.

In order to evaluate D_{it} and R_{it}, the reported methods in the Chapter 3 were applied on MOS structures fabricated at ENEA Portici labs by depositing p-type a-Si:H (the same used in TFSC) with a thickness of about 0.25 μm on F42 and F37d gel-derived films.

The high and low frequency (HF and LF) capacitance-voltage (C-V) curves were collected (as explained in Paragraph 1.6, Chapter 3) and they are displayed in Figure 4.35. These curves refer to MOS structures deposited on F37d ZnO film. For the MOS structure fabricated by using F42 ZnO film, only the final parameters are reported.

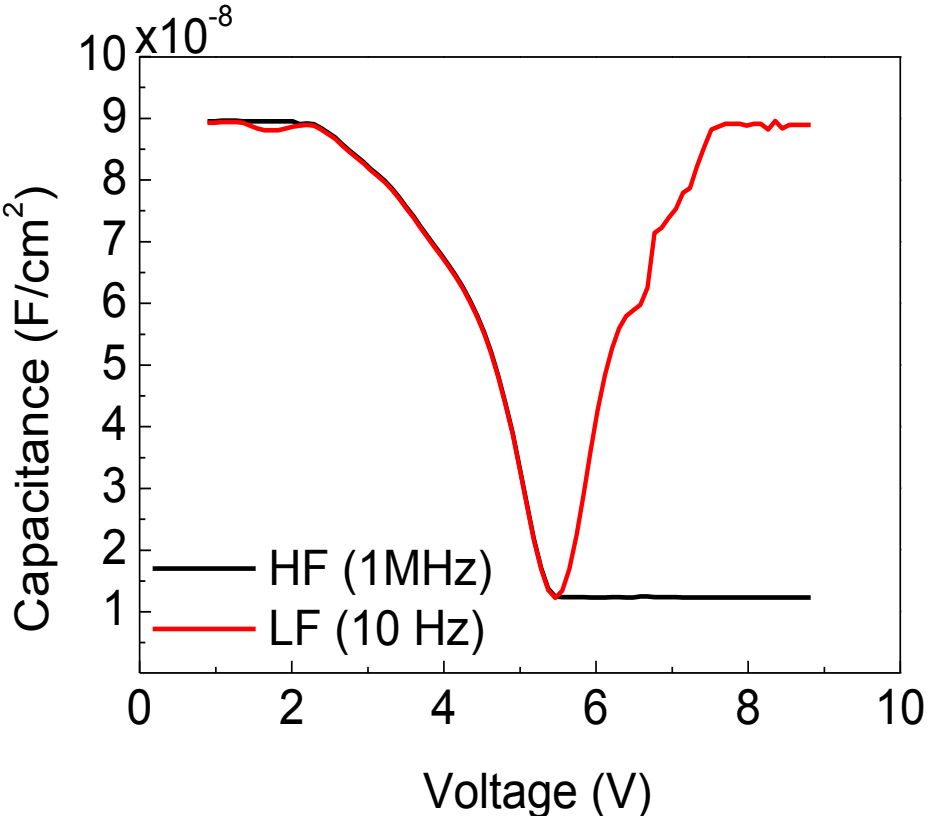

Figure 4.35: HF and LF C-V curves measured on *ad-hoc* MOS structures fabricated at ENEA by using F37d ZnO film.

From the elaboration of these curves, by adopting the procedure reported in Chapter 3, the average value of the D_{it} distribution was evaluated. For the MOS structure fabricated by using F42 film this was equal to $6.6 \cdot 10^{11}$ $cm^{-2}eV^{-1}$, while for MOS device on F37d film it was about $5 \cdot 10^{11}$ $cm^{-2}eV^{-1}$. These values confirm the influence of the growth mechanisms of TCO layer on the interface density of states [41,42]. All extracted values are comparable with those of commercial TCO [43] confirming the effectiveness of the use of Sol-Gel method for TCO deposition.

The other parameter qualifying the interface is R_{it}. In literature there are no straightforward methods for the extraction of the interface resistance. In Chapter 3 a simple method is proposed and explained. The procedure allows us to evaluate the R_{it} and the recombination lifetime (τ_r) near the interface region. This last indirectly qualifies the electrical interface with TCO layer. High τ_r is desirable for PV applications.

The extraction of R_{it} and τ_r requires the measurement of conductance-frequency (G-f) curve, as explained in the previous chapter. For the MOS structure on F37d ZnO film, the G-f curve is reported in Figure 4.36.

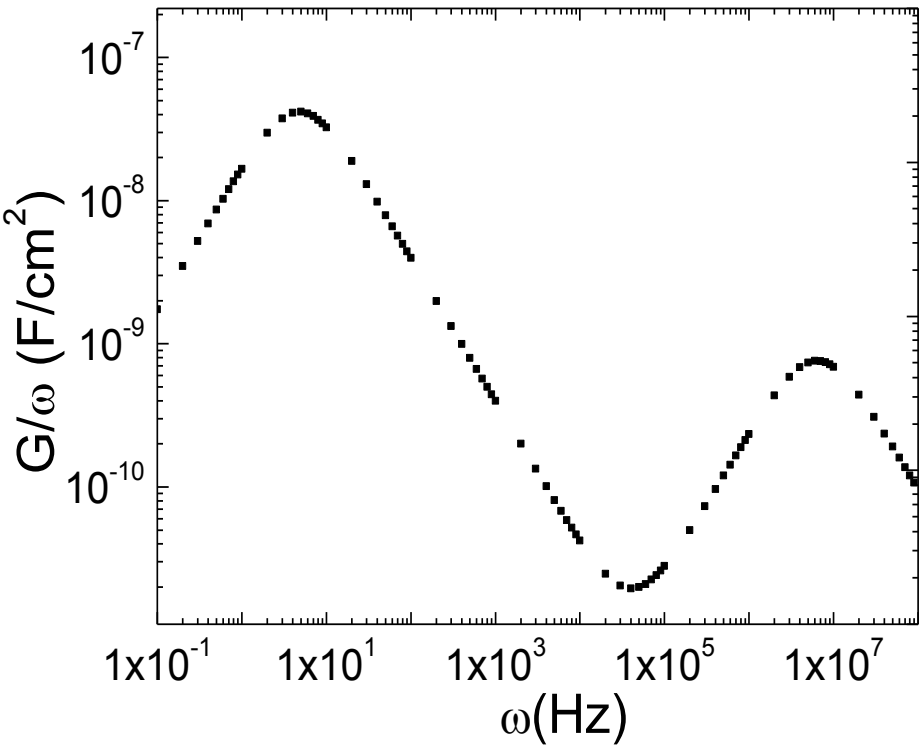

Figure 4.36: G-f curve of the MOS structure deposited on F37d ZnO film.

By applying the proposed procedure, R_{it}=90 $\Omega \cdot cm^2$ and τ_r= 3.4 μs was found while for the other MOS structure R_{it}=97 $\Omega \cdot cm^2$ and τ_r= 2.1 μs was found. These results agree well with the D_{it} values confirming that the F37d film (deposited from the solution with the highest pH value) is better than F42. Moreover, these values are in the same order of the values carried out on MOS devices fabricated on commercial TCO (SnO_2 - Asahi U-type). In fact, in literature there are no available data and commercial TCO are characterised by adopting this procedure on MOS fabricated *ad-hoc* at ENEA labs. The extracted values are: R_{it} =85 $\Omega \cdot cm^2$ and τ_r= 4.1 μs.

3.2 Thin Film Solar Cells Characterisation

Single junction a-Si:H solar cells were deposited [40] on films presented in Table 4.4. Figure 4.37 shows a photo of TFSCs fabricated at ENEA labs.

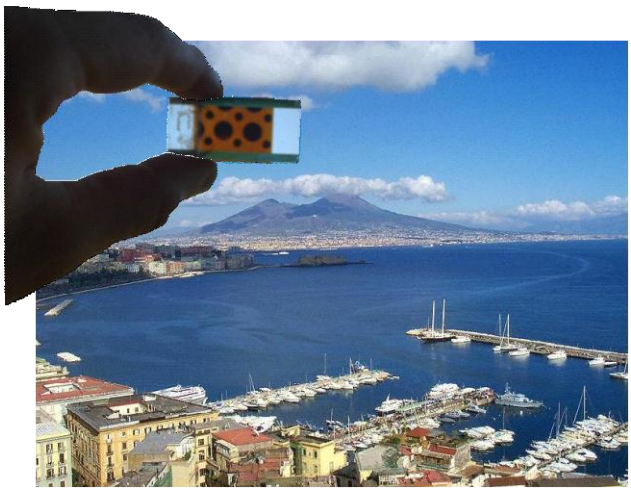

Figure 4.37: Thin Film Solar Cells fabricated at ENEA Portici labs.

These cells were characterised by measuring the Current-Voltage (I-V) curves in both dark and light conditions. Light measurements were performed by exposing cells to AM1.5G illumination by means of a class A solar simulator while applying a Nitrogen flux so as to avoid heating effects. I-V characteristics were monitored and recorded by using two 2430 Keithley SMUs and the external quantum efficiency (EQY) was collected for both cells. EQY is the ratio of the number of charge carriers collected by the solar cell to the number of photons of a given wavelength "shining on the solar cell from outside"(incident photons). It indicates the amount of current that the cell will produce when irradiated by photons at a particular wavelength. If the cell's quantum efficiency is integrated over the whole solar electromagnetic spectrum, the photogenerated current is evaluated. EQY curves of both cells (TFSC1 - pH=7.66) and TFSC2 - pH=8.76) are reported in Figure 4.38. In this graph the EQY of a TFSC deposited on commercial TCO (SnO_2 - Asahi U-type) is also shown.

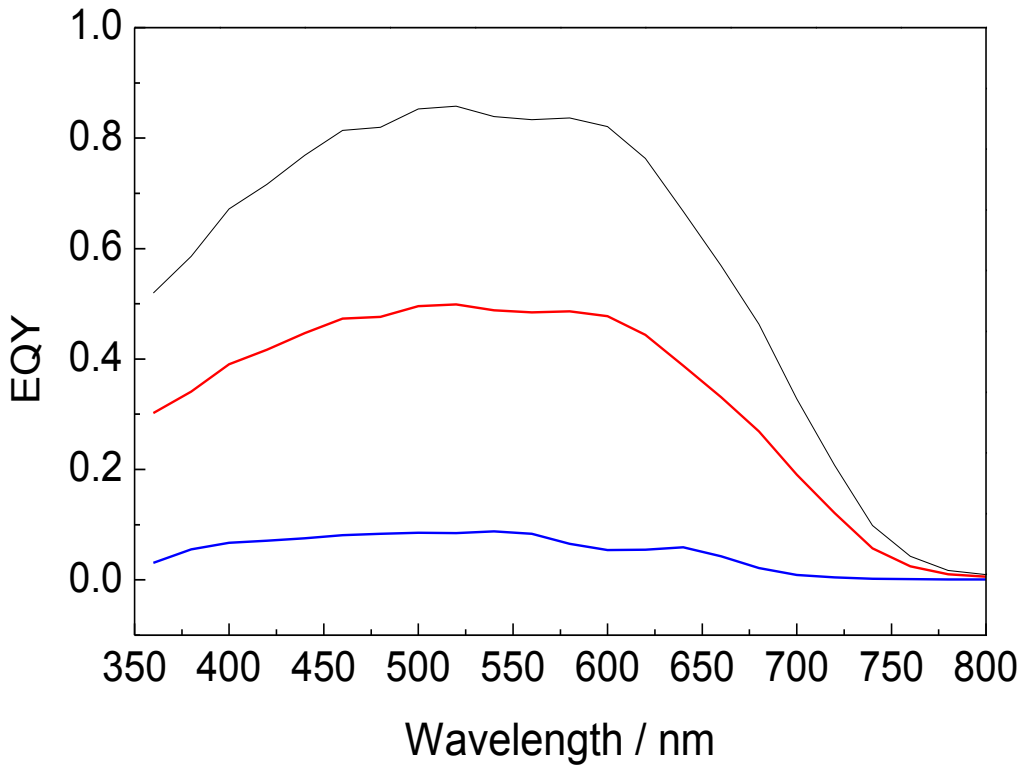

Figure 4.39: External Quantum Yield of TFSCs deposited on gel derived doped ZnO films: TSFC1- pH= 7.66 (blue line), TSFC2 – pH=8.76 (red line) and reference TFSC (black line).

By elaborating the I-V curves and the EQY curves, the global parameters qualifying the solar cells [44] were extrapolated and they are reported in Table 4.5.

Table 4.5: Global parameters of thin film solar cells.

Parameter	TFSC1 (7.66 pH)	TFSC2 (8.76 pH)
Open Circuit Voltage (V_{oc})	0.47 *V*	0.51 *V*
Short Circuit Current Density (J_{SC})	1.5 mA/cm^2	8.86 mA/cm^2
Fill Factor (%)	26.4	30
Conversion Efficiency (%)	0.19	1.35

From the data reported in this Table, it is clear that by reducing the electrical resistivity of TCO layer the solar cell performances improve. As a matter of fact, in the case of TFSC2 the efficiency was 1.35% instead of 0.19% of the TFSC1. These values are lower than the typical efficiencies of this kind of technology [40] whose normal range is 7-10%. This difference is due to the high series resistance [44] affecting I-V curves. It is to be found 1.1 $k\Omega$ for TFSC1 and 0.5 $k\Omega$ for TFSC2 (they are extrapolated from dark I-V curves). Typical series resistances for thin film technology are lower than 5 Ω. A reduction of at least one order of magnitude in term of electrical resistivity is required for TCO use in PV applications.

In any case, these preliminary results confirmed the fact that the gel-derived ZnO layers are compatible with the deposition processes of TFSC and stimulate us to deeply investigate how to further reduce the TCO electrical resistivity.

References

[1] J. Tauc, R. Grigorovici and A. Vancu, Physica Status Solidi, 15, pp. 627-637, (1966).

[2] E.A. Davis and N.F. Moh, Philosophical Magazine, 22, pp. 903-922, (1970).

[3] S. Rani, P. Suri, P.K. Shishodi and R.M. Mehra, Sol. Energ. Mat. Sol. Cells, 92, pp. 1639-1645, (2008).

[4] S. O'Brien, L.H.K. Koh and G. M. Crean, Thin Solid Films, 516, pp. 1391-1395, (2008).

[5] J.-H. Lee, K.-H. Ko and B.-O. Park, J. Cryst. Growth, 247, pp. 119-125 (2003).

[6] C.-Y. Tsay, K.-S. Fan, S.-H. Chen and C.-H. Tsai, J. Alloys Compd., 495, pp. 126-130 (2010).

[7] G. T. Delgado, C. I. Z. Romero, S. A. M. Hernández, R. C. Pérez and O. Z. Angel, Sol. Energy Mater. Sol. Cells, 93, pp. 55-59 (2009).

[8] S. Bandyopadhyay, G.K. Paul and S.K. Sen, Sol. Energy Mater. Sol. Cells, 71, pp. 103-113 (2002).

[9] C.-Y. Tsay , K.-S. Fan, Y.-W. Wang, C.-J. Chang, Y.-K. Tseng and C.-K. Lin, Ceram. Int., 36, pp. 1791-1795 (2010).

[10] A. Gulino, F. Lupo and M. E. Fragalà, J. Phys. Chem. C, 112, pp. 13869-13872 (2008).

[11] L.D. Landau and B.G. Levich, Acta Physiochimica URSS, 17, pp. 42-46 (1942).

[12] M. Çopuroğlu, L.H.K. Koh, S. O'Brien and G.M. Crean, Journal of Sol–Gel Science and Technology, 52, pp. 432-438, (2009).

[13] S. O'Brien, M.G. Nolan, M. Çopuroğlu, J.A. Hamilton, I. Povey, L. Pereira, R. Martins, E. Fortunato and M. Pemble, Thin Solid Films, 518, pp. 4515-4519 (2010).

[14] M. Dutta, S. Mridha and D. Basak, Applied Surface Science, 254, pp. 2743-2747 (2008).

[15] M.H. Aslan, A.Y. Oral, E. Mensur, A. Gul and E. Basaran, Solar Energy Materials & Solar Cells, 82, pp. 543-552 (2004).

[16] T-Y Shie and C-F. Lin, In: Eighth IEEE conference on nanothecnology 2008, Arlington, Texas, USA; 18–21, pp. 756–759 (August 2008).

[17] A.V. Shah, H. Schade, M. Vanecek, J. Meier, E. Vallat-Sauvain, N. Wyrsch, et al., Progress in Photovoltaics: Research and Applications, 12, pp. 113-142 (2004).

[18] D.K. Schroder, Semiconductor material and device characterisation, 3rd ed, Wiley-Interscience, New York, 2005.

[19] M.H. Sukkarand H.L. Tuller, Advanced Ceramics, 7, pp. 71-90 (1984).

[20] V. Musat, B. Teixeira, E. Fortunato and R.C.C., Thin Solid Films, 502, pp. 219-222 (2006).

[21] S. Fujihara, C. Sasaki and T. Kimura, Applied Surface Science, 180, pp. 341-350 (2001).

[22] L. Znaidi, Materials Science and Engineering B, 174, pp. 18-30 (2010).

[23] D. C. Look, J. W. Hemsky and J. R. Sizelove, Physical Review Letters, 82, pp. 2552-2555 (1999).

[24] M V. Musat, B. Teixeira, E. Fortunato and R.C.C. Monteiro, Thin Solid Films, 502, pp. 219-222 (2006).

[25] C. G. Van de Walle, Phisical Review Letters, 85, pp. 1012-1015 (2000).

[26] S.F.J. Cox, E.A. Davis, S.P. Cottrell, P.J.C. King, J.S. Lord, J.M. Gil, H.V. Alberto, R.C. Vilao, J. Piroto Duarte, N. Ayres de Campos, A. Weidinger, R.L. Lichti and S.J.C. Irvine, Phys. Rev. Lett., 86, pp. 2601-2604 (2001).

[27] D.M. Hofmann, A. Hofstaetter, F. Leiter, H. Zhou, F. Henecker, B.K. Meyer, S.B. Orlinskii, J. Schmidt and P.G. Baranov, Phys. Rev. Lett., 88, pp. 045504-045507 (2002).

[28] A. Janotti and C.G. Van de Walle, Nat. Mater., 6, pp. 44-47 (2007).

[29] E.V. Lavrov, F. Herklotz and J. Weber, Phys. Rev. B, 79, pp. 165210-165222 (2009).

[30] V. Kumar, R.G. Singh, L.P. Purohit and R.M. Mehra, J. Mater. Sci. Technol., 27 (6), pp. 481-488 (2011).

[31] Y. Yamamoto, K. Saito, K. Takahashi and M. Konagai, Sol. Energy Mater. Sol. Cells, 65, pp. 125-132 (2001).

[32] S. Ilican, F. Yakuphanoglu, M. Caglar and Y. Caglar, J. Alloys Compd., 509, pp. 5290-5294 (2011).

[33] G. Kim, J. Bang, Y. Kim, S. K. Rout and S. Ihl Woo, Appl. Phys. A, 97, pp. 821-828 (2009).

[34] R.B.H. Tahar and N.B.H. Tahar, J. Mater. Sci., 40, pp. 5285-5289 (2005).

[35] M.L. Addonizio and C. Diletto, Solar Energy Mater. Solar Cells, 92, pp. 1488-1494 (2008).

[36] K. Sivakumar, V.S. Kumar, N. Muthukumarasamy, M. Thambidurai and T. S. Senthil, Bull. Mater. Sci., 35, pp. 327-331 (2012).

[37] R. Wahab, S. G. Ansari, Y. S. Kim, M. Song and H. S. Shin, Appl. Surf. Sci., 255, pp. 4891-4896, (2009).

[38] M.H. Aslan, A. Y. Oral, E. Mensur, A. Gul and E. Basaran, Sol. Energy Mat. Sol. Cells, 82, pp. 543-552 (2004).

[39] B. Houng, C.L. Huang and S.Y. Tsai, Journal of Crystal Growth, 307, pp. 328-333 (2007).

[40] L.V. Mercaldo, M.L. Addonizio, M. Della Noce, P. Delli Veneri, A. Scognamiglio and C. Privato, Applied Energy, 86 (10), pp. 1836-1844 (2009).

[41] R. Romero, M.C. López, D. Leinen, F. Mart´ın, J.R. Ramos-Barrado, Mat. Sci. Eng. B, 110, pp. 87-93 (2004).

[42] G. Cannella, F. Principato, M. Foti, C. Garozzo, S. Lomabrdo, Energy Procedia, 3, pp. 51-57 (2011).

[43] T. Minami, Semicond. Sci. Technol. 20, pp. S35-S44 (2005).

[44] S. Daliento and L. Lancelloti, Solar Energy, 84 (01), pp. 44-50 (2010).

CONCLUSIONS

In this PhD research activity the Sol-Gel synthesis of transparent and conductive ZnO thin films, suitable for photovoltaic (PV) applications was deeply studied.

In particular, the main problems of the Sol–Gel synthesis of ZnO thin films were analysed. The control of the Zn^{2+} reactivity in a hydro-alcoholic environment is the key aspect of the preparation procedure. The use of triethanolamine (TEA) allowed to prepare stable Zinc Acetate Dehydrate (ZAD) solutions with $[Zn^{2+}] \geq 0.5$ M without to resort to high hydrolysis temperatures thanks to its high chelating efficiency to Zn^{2+}. Both this result and the optimisation of the substrate wettability allowed establishing a valuable Sol–Gel route performed at room temperature. Thanks to this process ZnO thin films could be prepared by dip-coating. Single layer films with a thickness of about 125 *nm* exhibiting a high adhesion force to substrate (about 145 $kg \cdot cm^{-2}$) were obtained.

The research explains the influence of the annealing time and/or temperature on the nucleation and on the crystals growth rates of ZnO nanocrystals. Polycrystalline films containing randomly oriented ZnO nanocrystals (about 20 *nm*) with an average transmittance level in the visible region higher than 90% were obtained. The electrical resistivity of these films was found to be strongly influenced by the environment of post-annealing treatments. The effect of this environment on ZnO films was investigated. The research proved that the electrical resistivity decreased by increasing the treatment temperature. The minimum value was obtained by post-annealing the films in Forming Gas (FG) at a temperature of 450°C for 0.5 *h* and it is about 0.12 $\Omega \cdot cm$.

By doping the films with Boron (0.8% in atoms) an electrical resistivity of about 0.085 $\Omega \cdot cm$ was obtained. This value is acceptable for some applications. However, for thin film solar cells a further reduction was required. At this end multi layer ZnO films were deposited on glass supports. The electrical resistivity was found to reduce by increasing the thickness. Finally, the effect of pH solution on film properties was studied. In fact, in a more alkaline environment (at higher pH values) the ZnO crystal growth is enhanced. The high film crystallinity and the higher grain size contributed to the formation of ZnO films with high diffuse transmittance

(> 35% in the visible region) and a low electrical resistivity (10^{-2} $\Omega \cdot cm$). These values were carried out on films deposited by using a precursor solution with ZAD concentration of 1.0 M and a pH value of 8.76.

Moreover, an innovative characterisation technique monitoring the electrical interface between TCO layers and a-Si:H was developed. The adopted method was applied to test structures fabricated at ENEA Portici labs, by depositing a-Si:H (p-type) on gel derived ZnO films. This allowed the evaluation of the density of states at the interface (D_{it}). The values obtained (lower than 10^{12} $cm^{-2}eV^{-1}$) confirmed the effectiveness of Sol-Gel method in order to create TCO layers for PV applications.

So far the best gel derived ZnO films are characterised as following:

- Total transmittance in the visible region higher than 81% (average value);
- Diffuse transmittance in the visible region higher than 35% (average value);
- Surface roughness in the order of 30 *nm* (root main square – rms);
- Good film uniformity and homogeneity;
- Adhesion to the glass substrates in the order of 140 kg/cm^2;
- D_{it} lower than 10^{12} $cm^{-2} \cdot eV^{-1}$;
- Electrical resistivity of about 10^{-2} $\Omega \cdot cm$.

From an optical, a morphological and a structural point of view the deposited ZnO film are at the state of art for their use in PV applications. However, its electrical resistivity is still high. Moreover, it requires at least a reduction of about one order of magnitude. To this end Boron and Aluminium co-doping is still under investigation.

In any case in order to check the effectiveness of gel derived ZnO films in TFSC deposition process, single junction amorphous silicon thin film solar cells (a-Si TFSC) were deposited on these layers at ENEA Portici labs.

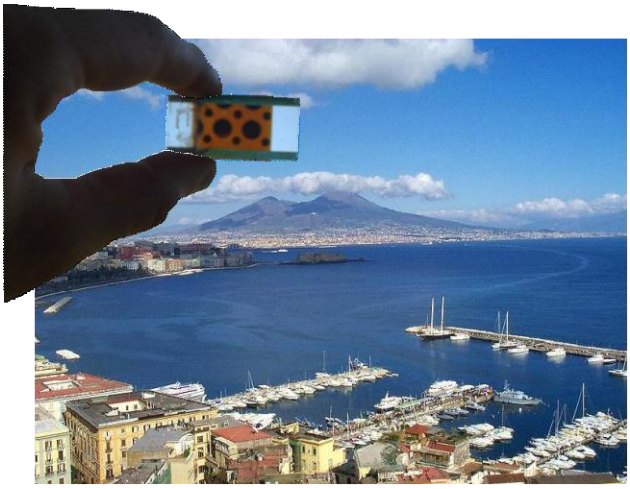

A short circuit current density of 8.85 mA/cm^2 and an open circuit voltage of 0.55 V were achieved confirming the good properties of the ZnO films. However, the Fill Factor (FF) and the efficiency were very low. This was probably due to interconnection troubles and high series resistance.